Manipulating optical properties of rubidium through microwave interactions

by

Andrei Tretiakov

A thesis submitted in partial fulfillment of the requirements for the degree of

Doctor of Philosophy

Department of Physics
University of Alberta

© Andrei Tretiakov, 2021

Abstract

Information transfer between a microwave field and light, also known as microwave-to-optical transduction, is a key area of research in quantum communication technology aimed at developing an interface between the superconducting processing devices operating at microwave frequencies and optical photons used for transferring quantum information over distance. Atomic vapors offer a good platform for such interfaces since they naturally support transitions at microwave and optical frequencies. In this work, we explored microwave-to-optical transduction in rubidium ensembles. We proposed a transduction method based on microwave-optical double resonance, where we can control the ensemble optical properties via non-linear interactions with a microwave magnetic field. With this method, we demonstrate the transduction of an audio signal from frequency-modulated and amplitude-modulated microwave fields to optical intensity modulation. We also present a protocol for engineering atomic spin polarization with microwave-assisted optical pumping and consider its applications for polarization-selective frequency conversion and microwave-controlled optical rotation.

Preface

The work presented in this manuscript would not be possible without the contribution of many members of the LeBlanc and the Davis labs.

The warm-atom apparatus used in Chapters 3, 4, and 6 was designed by Lindsay LeBlanc and Clinton Potts and was assembled by Clinton Potts, Timothy Lee, and Lindsay LeBlanc. The microwave cavity was designed and manufactured by Clinton Potts. Most of the data presented in Chapter 3 were collected together with Timothy. To obtain these results, we used the laser system from the quantum memory experiment, which was upgraded by Taras Hrushevskyi and Anindya Rastogi to accommodate our needs.

Chapter 3 is based on the publication Tretiakov, A., Potts, C. A., Lee, T. S., Thiessen, M. J., Davis, J. P., and LeBlanc, L. J., "Atomic microwave-to-optical signal transduction via magnetic-field coupling in a resonant microwave cavity", Applied Physics Letters, 116(16), 164101 (2020). The presented data were collected together with Timothy Lee. Lindsay LeBlanc and John Davis helped me with the experiment design and preparing the publication.

Chapter 5 is based on the publication Tretiakov, A., and LeBlanc, L. J., "Microwave Rabi resonances beyond the small-signal regime", Physical Review A, 99(4), 043402 (2019). The experiment was performed on the ultracold-gases apparatus with assistance from Taras Hrushevskyi. Lindsay LeBlanc helped me with the experiment design and preparing the publication and provided guidance with the simulation results.

The results presented in Chapter 6 were collected together with Brittany Lu using

the laser system for the newer cold-atom/cryogenic apparatus. The optical system was upgraded for our purposes by Taras Hrushevskyi.

Acknowledgements

Foremost, I am incredibly grateful to my supervisor Lindsay LeBlanc for her support and guidance in the lab, her help with preparing publications and conference talks, and her openness to my research ideas. Also, I want to thank my advisory committee members John Davis and Mark Freeman, with whom I had the pleasure of discussing my progress. Interacting with three people and observing their unique styles of research, management, and communication helped me shape my own vision of scientific research and academic life.

I would like to thank many of my peers I was lucky to interact with: my collaborators Clinton Potts, Timothy Lee, and Brittany Lu, who also helped with proofreading this thesis; people who occasionally helped with the equipment, including Hugh Ramp, Callum Doolin, and Anindya Rastogi; and all members of the LeBlanc group who created and maintained a friendly and supportive atmosphere in the lab.

Many thanks go to Edmonton's diverse Russian-speaking community, which helped me avoid home-sickness during my almost seven years in Canada. Especially to my close friends Anna, Georgui, Henna, Katia, Konshtie and Maggie, Maya and Vova, Tim, and Yuri, who are now scattered all over the world.

I would like to express my endless gratitude and appreciation to my dear friend Taras Hrushevskyi, with whom we spent many long hours in the lab and even longer hours outside. Together we have experienced many adventures in the majestic Canadian Rockies, including successful ascents of such alpine icons as Mt. Athabasca (3491 m), Mt. Temple (3544 m), Mt. Middle Sister (2769 m), and Mt. Big Sister (2982 m); memorable attempts of Mt. Robson and Mt. Little Sister; and

many other trips. These memories make leaving Alberta a truly hard decision.

Finally, I must thank my parents and family for their moral support and open-mindedness towards my life choices.

All of you and many other unmentioned people made my Ph.D. journey such a wonderful and enjoyable experience.

Table of Contents

List of Tables

List of Figures

List of Symbols

F	total internal angular momentum quantum number
Q	quality factor
Γ_1	total longitudinal relaxation rate
Γ_2	total transverse relaxation rate
Ω_{R}	Rabi frequency
$\hat{H}$	Hamiltonian operator
$\hat{\rho}$	density matrix operator
λ	wavelength
$\mathbf{B}$	static magnetic field vector
$\mathbf{b}$	microwave magnetic field vector
$\mathbf{k}$	wave-vector
ω_{m}	modulation frequency
ρ_{22}	population of state $\|2\rangle$
^{87}Rb	rubidium-87 isotope
m_F	total internal angular momentum projection quantum number

Constants

$\hbar$	reduced Planck's constant (J·s)	$1.054\ 571\ 817 \times 10^{-34}$

μ_{B}	Bohr magneton (J/T)	$9.274\ 009\ 994 \times 10^{-24}$
c	speed of light in vacuum (m/s)	299 792 458
e	elementary charge (C)	$1.602\ 176\ 634 \times 10^{-19}$
k_B	Boltzmann constant (J/K)	$1.380\ 649 \times 10^{-23}$
R_∞	Rydberg constant (m^{-1})	10 973 731.568 160

Abbreviations

AC alternating-current.

AM amplitude-modulated.

BB beam blocker.

BS beam splitter.

DC direct-current.

EIT electromagnetically-induced transparency.

FM frequency-modulated.

MW microwave.

PBS polarizing beam splitter.

PD photodetector.

WP wave plate.

Chapter 1

Introduction

The physics of interactions between electromagnetic fields and atoms and molecules, known as atomic and molecular optics, greatly impacted modern technology and fundamental science. In the first half of the 20th century, attempts to explain the rich structure of the emission spectrum of hydrogen lead to the creation of whole new areas of science, such as quantum mechanics and quantum electrodynamics. Later, research on microwave transitions in molecules resulted in the creation of the maser - the first source of coherent radiation and a precursor of the laser, the technology that shaped the world as we know it. These new technologies provided us with high-precision spectroscopy tools allowing even better measurements of atomic and molecular structures, fundamental constants, and properties of elementary particles.

These new tools were then adapted to control atomic properties. The effect of electromagnetic radiation on atomic motion was used to create the coldest matter in the universe and to study its unique macroscopic quantum properties. The effect of electromagnetic fields on the atomic quantum state provided us with several generations of the most accurate clocks, and precise and portable electromagnetic field sensors. Nowadays, due to the ever-increasing precision and accuracy with which atomic motion and quantum states can be manipulated, the field of atomic optics is gaining influence in quantum information and communication by providing promising platforms for quantum processing, quantum simulation, and storage and transduction

of quantum information.

During my doctoral research, I investigated microwave-to-optical transduction in rubidium vapor and its applications for magnetometry and quantum communications. In the context of this work, we refer to transduction as a modulation transfer between two electromagnetic fields. In our case, we implement transduction via nonlinear interactions between the electric-field component of laser light and the magnetic-field component of a microwave field in a rubidium vapor. The transduction idea builds upon the fact that the vapor's optical properties, such as absorption and dispersion, depend on the quantum states of the atoms interacting with light, while the atomic quantum states depend on the microwave field applied to the vapor. The main focus of my work was to develop tools for controlling the optical properties of a rubidium vapor via microwave interactions for microwave-to-optical transduction with several potential applications discussed below.

1.1 Applications

Microwave-to-optical transduction in atomic vapors plays a significant role in modern technology, including precise magnetometry, microwave frequency and power standards, conversion of radio signals to optical intensity signals, and shows great promise in quantum information science. Below we review state of the art in these techniques and discuss their relevance to our research.

1.1.1 Quantum computing

Unlike classical information, which consists of discrete zeros and ones, quantum information relies on a quantum system's ability to simultaneously be in several orthogonal quantum states, allowing encoding of information in a superposition of zeros and ones. As a result, a computer based on quantum-information principles can perform certain computational tasks at unprecedented speeds compared to classical computers [1, 2]. In addition, quantum information gives access to novel cryptography tools, improving

the security of communication [3].

Currently, some of the most promising candidates for a processing unit in a quantum computer operate in the microwave range [4], including superconducting circuits [5, 6], solid-state spins [7, 8], and trapped atoms [9–12] and ions [13]. At the same time, the long-distance transfer of quantum information mostly relies on optical photons [14–16]. To bridge the gap between the two, one needs a system that can coherently transfer quantum information between the two frequency ranges [17]. Several different systems can potentially implement such wavelength conversion, e.g., optomechanical systems [18–20], spin ensembles in solid-state devices [21–24], electro-optical modulators [25, 26], magnons [27], and atomic ensembles [28–32].

Rubidium vapors naturally support transitions at microwave and optical frequencies, making them a good platform for microwave-to-optical wavelength conversion. Besides, rubidium ensembles can be cooled below 1 μK, which offers a good coherence time for storing quantum information [33, 34]. By studying microwave-to-optical transduction in rubidium vapors, we hope to get one step closer to realizing quantum information transfer between these frequency domains.

1.1.2 Frequency standards

Transduction of microwave frequency modulation to the optical intensity in alkali vapor cells is used in compact frequency standards [35–38], i.e., devices providing stable signal serving as a frequency reference for calibration and frequency-locking. The transduction is based on the microwave-optical double resonance [39], where the two fields are close to resonance with the corresponding atomic transitions. Due to non-linear interactions between the microwave and optical fields, the optical absorption experiences a resonance when the microwave frequency matches a frequency of one of several hyperfine transitions. Because the transition frequency depends only on the fundamental constants, it can serve as a frequency reference providing the frequency standard. The transduction based on the double resonance can operate in

a continuous-wave regime, simplifying the experimental setup and making the frequency standards based on this technique relatively compact, portable, and versatile.

We will cover the physics of atomic transitions and the microwave-optical double resonance in Chapter 2 and Chapter 3.

1.1.3 AC magnetometry and power standards

The double-resonance setup discussed above also allows the transduction of microwave phase modulation to the optical intensity. In the case of harmonic modulation, the optical intensity varies periodically, with its spectrum depending on the relation between the microwave power and the modulation frequency. The optical signal response to varying the modulation frequency depends only on the microwave power and fundamental constants [see Chapter 5], providing a precise measure of the microwave power. Originally this technique was proposed to provide a microwave power standard [40–42], but nowadays, it is widely used for measuring the amplitude of the microwave magnetic field [43–49].

1.1.4 Radio-over-fiber communication

Another common application of microwave-to-optical transduction in atomic vapors is radio-over-fiber communications [50–61]. Here, an analog or a digital signal encoded as a frequency, amplitude, or phase modulation of a microwave field is transferred to an optical carrier. The atomic vapor cell here serves as both the receiving and the demodulating device, which is lightweight and electrically isolated [51].

1.2 Novelty of this work

This work aims to bring together various types and applications of the microwave-to-optical transduction discussed above under a single theoretical framework with an emphasis on the quantum nature of the process. During the research, we made the following contributions to the field:

- We adapted the double-resonance technique for radio-over-fiber applications, where this effect was used in room-temperature rubidium inside a microwave cavity to transduce an audio signal encoded as frequency and amplitude modulation of the microwave field to the intensity modulation of laser light. In a proof-of-principle experiment, we demonstrated the transduction for a microwave carrier transmitted via cable and free space. The experimental setup in our method is simpler and more suitable for real-life applications than the one used in the conventional technique based on electromagnetically-induced transparency. The quantum nature of our technique makes it potentially applicable to quantum information. These results were published in [62] and are discussed in detail in Chapter 4.

- Through numerical simulation and experiment, we studied the quantum-dynamics of a two-level system driven by a phase-modulated field with a large modulation index. Our findings could potentially improve the precision of microwave magnetometry in systems with limited interrogation time, making it feasible for the ultracold atoms, as demonstrated in our proof-of-principle experiments. These results were published in [63]. Chapter 5 provides the relevant theory and details of the experiment and simulation.

- We showed that microwave-optical double resonance can be used for frequency conversion based on optical switching. Within this approach, we also introduced a microwave-assisted optical pumping technique that allows controlling the population of specific Zeeman sublevels in the ground state. In Chapter 6, we describe the technique and show that it can be used for polarization-selective frequency conversion and microwave control of optical rotation.

Chapter 2

Background

In our experiments, we study how rubidium vapor interacts with electromagnetic fields at microwave and optical frequencies simultaneously. In particular, we are interested how one interaction can affect the other one. By examining what effect the variation in microwave parameters has on optical properties such as absorption and dispersion, we develop tools for microwave-to-optical signal transduction. In our setup, we use optical and microwave fields with frequencies close to resonance with electric-dipole and magnetic-dipole transitions in the rubidium-87 (^{87}Rb) isotope, respectively.

In this chapter, we discuss a brief overview of the relevant concepts in atomic optical physics to provide essential background and context for my research. To begin with, we introduce the energy-level structure of ^{87}Rb (and hydrogen-like atoms in general) and provide a description of the main physical effects contributing to it. Next, we move on to level splitting due to magnetic-dipole interaction with a weak external static magnetic field (the linear Zeeman effect), which gives rise to a family of microwave transitions observed and employed in later chapters. Finally, we introduce the theory of atomic transitions due to interactions with external oscillating electric and magnetic fields and conclude by discussing ensemble effects on quantum evolution.

2.1 Energy levels

Atomic optical physics studies interactions between an electromagnetic field and a single atom or ion, several atoms or ions, or a macroscopic ensemble of neutral[1] atoms weakly-interacting with each other. In our experiments, we work with ensembles of neutral atoms in the form of dilute vapor either at room temperature or laser-cooled. In contrast to condensed-matter systems, weak interactions between atoms within such ensembles do not significantly alter each atom's energy-level structure. Thus, all atoms within the ensemble have approximately the same energy-level structure and interact with external fields independently. This fact allows us to model an ensemble interacting with an external electromagnetic field as a single atom and to treat the ensemble effects phenomenologically (see Section 2.4).

When we describe the energy of an atom in atomic optical physics, we mostly focus on the energy of its electrons. As an alkali metal element, ^{87}Rb has an odd number of electrons, with a single unpaired electron above a closed core of filled electron shells (see Figure 2.1). Compared to the outer electron, the core is very robust under the influence of external fields. Below, we refer to this outer electron when we discuss the energy structure of alkali atoms. Because the closed core effectively neutralizes the positive nuclear charge of all but one proton, the energy level structure is similar to that of a hydrogen atom. In a nutshell, the energy levels can be represented as a gross structure due to Coulomb interaction with the nuclear electric charge, which splits into the fine structure due to spin-orbit interaction, and is further split into the hyperfine structure due to magnetic interaction with the nucleus.

[1] This is an intended tautology frequently used in the field to highlight the difference from charged ions, which employ a completely distinct set of experimental tools. In this manuscript, unless explicitly specified, all atoms are presumed to possess a neutral total electric charge.

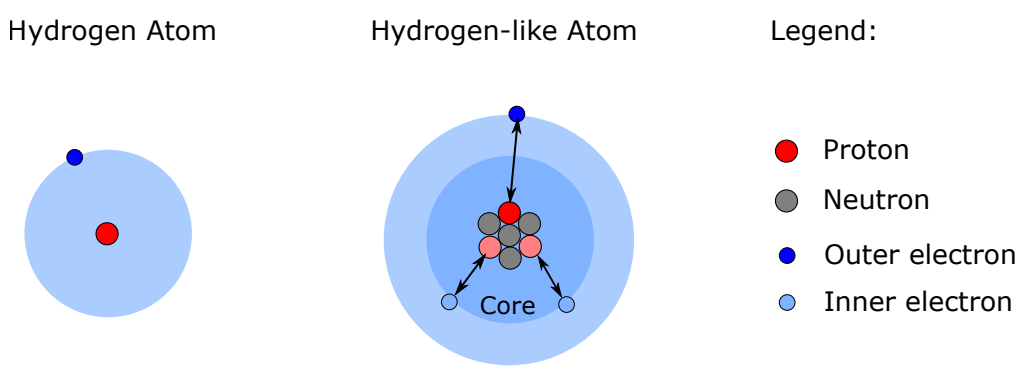

Figure 2.1: Illustration of a hydrogen atom and an alkali atom, using ^{7}Li as an example. In the case of ^{7}Li, two inner electrons form a closed core that neutralizes the positive electric charge of two protons.

2.1.1 Gross structure

As was discussed above, the closed electronic core reduces the effective nuclear charge interacting with the outer electron. As a result, the gross structure energy levels due to Coulomb interaction are similar to those of a hydrogen atom and are given by [64]

$$E(n,l) = -2\pi\hbar c \frac{R_\infty}{(n-\delta_l)^2}, \tag{2.1}$$

where n is the principal quantum number, l is the orbital quantum number, $\hbar$ is the reduced Planck constant, c is the speed of light in vacuum, and R_∞ is the Rydberg constant. The quantum defect δ_l takes into account the fact that the outer electron can penetrate into the core, which reduces the screening effect. The penetration depth depends on the shape of the wavefunction, determined by l, with the highest contribution for the s-state where $l = 0$. In ^{87}Rb , the lowest energy level is characterized by $n = 5$ and $l = 0$ with quantum defect $\delta_s = 3.19$ [64].

2.1.2 Good quantum numbers

Before moving on to the next-order corrections to the electron's energy, I would like to introduce a concept of "good" quantum numbers. This is terminology which is usually used in atomic physics to describe fine and hyperfine structures of atoms. An

eigenvalue a of a quantum operator $\hat{A}$ is considered a good quantum number if $\hat{A}$ (approximately) commutes with the atomic Hamiltonian. In this case, because the expectation value of $\hat{A}$, which coincides with a, does not evolve in time, it provides a good way to describe a quantum state at any given moment. Good quantum numbers are analogous to constants of motion in classical mechanics [64].

2.1.3 Fine structure

Taking into account the electron's magnetic moment associated with its spin splits the gross levels into a manifold know as the fine structure. When the electron moves through the nuclear electric field, it experiences an effective magnetic field proportional to the electron's speed.

This effect can be qualitatively understood in terms of the Bohr model of a hydrogen atom if we move to the electron's reference frame, as is shown in Figure 2.2. In this frame, the nucleus orbits around the electron with an orbital angular momentum $-\mathbf{l}$, where $\mathbf{l}$ is the electron's orbital momentum vector in the nuclear frame. Since the nucleus is charged, its motion creates a magnetic field aligned with its orbital momentum. Because the electron's orbital angular momentum determines the direction and magnitude of this field, its effect on the atom's energy due to magnetic-dipole interaction with the electron's spin $\mathbf{s}$ is called spin-orbit coupling. It can be expressed as an additional term in the Hamiltonian [65]:

$$\hat{H}_{\text{so}} = A_{\text{fs}} \hat{\mathbf{l}} \cdot \hat{\mathbf{s}} = A_{\text{fs}} \left(\hat{l}_x \hat{s}_x + \hat{l}_y \hat{s}_y + \hat{l}_z \hat{s}_z \right), \tag{2.2}$$

where A_{fs} is the constant describing the strength of the coupling. Note that, even though the above model provides us with the correct qualitative dependence of the energy on $\mathbf{l} \cdot \mathbf{s}$, in order to calculate the coupling strength, we would need a fully relativistic treatment [66].

The spin-orbit coupling term $\hat{H}_{\text{so}}$ commutes with $\hat{l}^2$ and $\hat{s}^2$, but not $\hat{l}_z$ and $\hat{s}_z$, meaning that l and s are good quantum numbers, but m_z and m_s are not[2]. On the

[2]See Appendix A for more details on angular momentum operators and their eigenvalues.

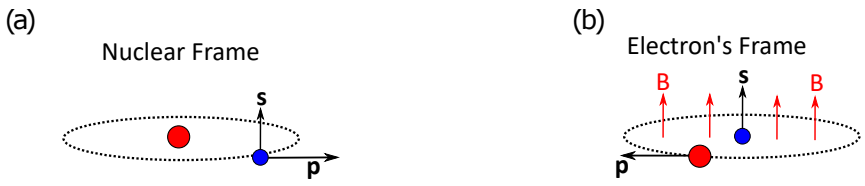

Figure 2.2: Toy model for the spin-orbit coupling in the Hydrogen atom. (a) In the nuclear reference frame, the electron circles around the nucleus with momentum $\mathbf{p}$. (b) In the electron's reference frame, the nucleus circles around the electron with momentum $-\mathbf{p}$. This motion produces magnetic field $\mathbf{B}$ with the magnetic dipole associated with the electron's spin $\mathbf{s}$.

other hand, if we define the electron's total angular momentum as $\hat{\mathbf{j}} = \hat{\mathbf{l}} + \hat{\mathbf{s}}$, then $\hat{j}^2$ and $\hat{j}_z$ commute with $\hat{H}_{\text{so}}$, and both j and m_j are good quantum numbers.

Therefore, the spin-orbit interaction splits the energy levels according to the value of j. In the ground state of an alkali atom, the total angular momentum includes the electron's spin only, so the ground-state level does not split due to spin-orbit coupling. On the other hand, the first excited state with $l = 1$ splits into a doublet with $j_1 = 1/2$ and $j_2 = 3/2$. Following the standard spectroscopic notation, we refer to the transition lines between these doublet states and the ground state as the D1 and D2 lines, respectively. In ^{87}Rb the wavelength of the D1 line is approximately 794.978 nm [67], and the wavelength of the D2 line is approximately 780.241 nm [67].

In the fully relativistic treatment, there are other terms that contribute to the Hamiltonian on the same order as the spin-orbit coupling, namely the second-order relativistic correction to the kinetic energy and zitterbewegung [66]. Another energy shift of the same order comes from the quantum electrodynamics and is known as the Lamb shift [68]. All these effects do not provide any additional insight for understanding the fine structure of alkalies and are not discussed here.

2.1.4 Hyperfine structure

Because protons and neutrons have magnetic moments associated with their spins, the nucleus possesses a magnetic dipole moment proportional to the total nuclear

spin **I**. This nuclear magnetic moment interacts with the magnetic field produced by the electron's motion and magnetic dipole moment. The additional energy due to this interaction is given by [69]

$$\hat{H}_{\text{hfs}} = A_{\text{hfs}} \hat{\mathbf{I}} \cdot \hat{\mathbf{j}} = A_{\text{hfs}} \left(\hat{I}_x \hat{j}_x + \hat{I}_y \hat{j}_y + \hat{I}_z \hat{j}_z \right), \tag{2.3}$$

where A_{hfs} is the isotope- and transition-specific constant determining the interaction strength. This interaction causes the fine-structure levels to split according to the value F of the total atomic angular momentum[3] $\hat{\mathbf{F}} = \hat{\mathbf{j}} + \hat{\mathbf{I}}$, with the new levels forming the hyperfine structure. The hyperfine levels are characterized by new good quantum numbers F and m_F, while m_j is no longer a good quantum number. For us, of a special interest is the hyperfine structure of the ground state in alkali elements. In the absence of external fields, it consists of two energy levels corresponding to $F_1 = |I - 1/2|$ and $F_2 = |I + 1/2|$. The nuclear spin of ^{87}Rb is 3/2, which gives the ground-state levels with $F_1 = 1$ and $F_2 = 2$, respectively, that are separated by a transition at a microwave frequency of 6.83468261090429(9) GHz [67]. The hyperfine structure of the D1 and D2 lines is shown in Figure 2.3.

For heavy elements like Rb, taking into account the finite size of the nucleus leads to noticeable corrections to the hyperfine structure, such as the isotope volume shift [69] and electric-quadrupole interaction between the electron and the nucleus [67]. These effects do not play an important role in our experiments; therefore, we will omit their details.

2.2 Linear Zeeman effect

In a static magnetic field **B**, a system with magnetic dipole moment $\boldsymbol{\mu}$ acquires energy $H_{\text{Z}} = -\boldsymbol{\mu} \cdot \mathbf{B}$. For a quantum system, it is usually convenient to choose the z-axis along the direction of the magnetic field vector and consider the quantum-state

[3] Here we use lower case letters for parameters describing a single particle, i.e., an electron, while the capital letters correspond to systems of many particles, such as a nucleus or an atom.

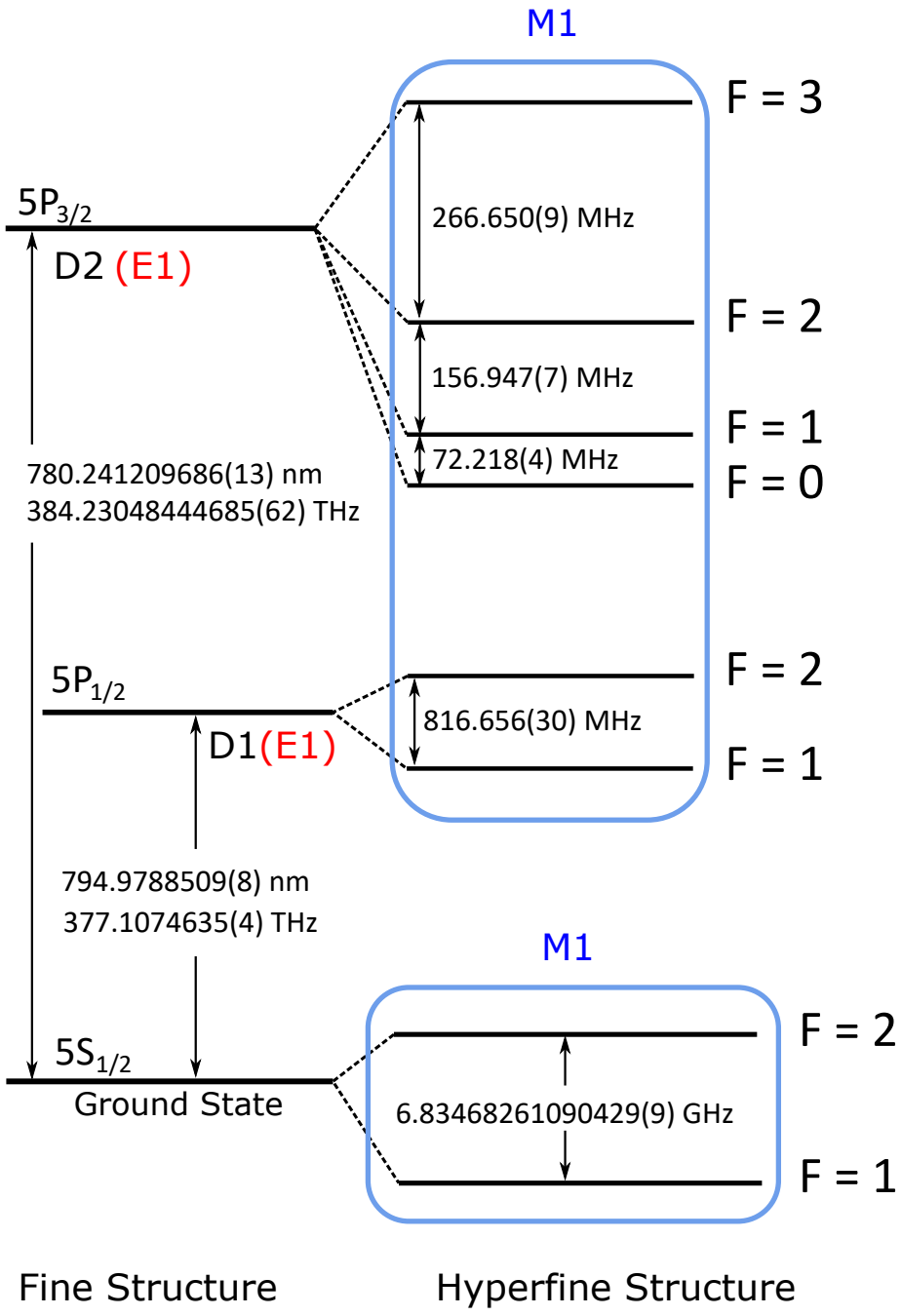

Figure 2.3: The hyperfine structure of the D1 and D2 lines in^{87}Rb . Arrows indicate the energy splitting between levels in units of frequency and wavelength. Electric-dipole and magnetic-dipole transitions are labeled as E1 and M1, respectively. Adapted from [67].

evolution in the basis of eigenstates of $\hat{\mu}_z$. We are interested in the low-field limit, where the interaction energy is much smaller than the hyperfine coupling, and we can treat it as a perturbation. In this case, the magnetic dipole moment is coupled to the atom's total angular momentum, and the magnetic energy can be expressed in terms of the good quantum numbers F and m_F as

$$E_z = g_F m_F \mu_{\mathrm{B}} B, \tag{2.4}$$

where μ_{B} is the Bohr's magneton, and

$$g_F = \left[1 + \frac{j(j+1) + s(s+1) - l(l+1)}{2j(j+1)}\right]\left[\frac{F(F+1) + j(j+1) - I(I+1)}{2F(F+1)}\right] \tag{2.5}$$

is the Landé g-factor.

As a result, a hyperfine level $|F\rangle$ splits into $2F+1$ sublevels $|F, m_F\rangle$, with $m_F = \{-F, -F+1, \ldots, F\}$, and the energy difference between two neighboring sublevels is given by $g_F \mu_{\mathrm{B}} B$. This phenomenon is known as the linear Zeeman effect and we refer to the new states as Zeeman sublevels. As the magnetic energy $\mu_{\mathrm{B}} B$ becomes comparable with the hyperfine coupling strength A_{hfs}, higher-order terms of B have to be taken into account, and m_F is no longer a good quantum number.

In the ground state of alkalis, Eq. 2.5 reduces to $g_F = \pm 1/(s+I)$, with the negative value corresponding to the lower energy level. In ^{87}Rb, the ground state g-factors are $\pm 1/2$, leading to Zeeman splitting between two neighboring sublevels by $\Delta E_Z = \pm 2\pi\hbar B \times (0.70\ \mathrm{MHz/G})$ [67], where $\hbar$ is the reduced Planck constant measured in the SI units, and B is measured in Gauss. Despite its small value compared to the linewidth of the optical transitions in Rb, the linear Zeeman splitting can be resolved through the microwave-optical double-resonance spectroscopy and plays an important role in our experiments, as will be discussed in Chapter 3.

2.3 Transitions due to oscillating fields

An electron within an atom can change its energy and quantum state due to interactions with an oscillating electric or magnetic field. Most experiments in atomic

optical physics employ transitions due to electric-dipole and magnetic-dipole interactions with an external field. This chapter will focus on these transitions in the case of a monochromatic field, which allows solving the quantum dynamics analytically.

2.3.1 Selection rules

An electromagnetic field can drive a transition between two atomic states only if the following conditions are satisfied.

1. The driving frequency is sufficiently close to the energy difference (in frequency units) between the two states. This condition is analogous to the resonance condition in a driven classical harmonic oscillator.

2. The result of the action of the coupling operator $\hat{V}$ on the initial state $|i\rangle$ has a nonzero projection on the final state $|f\rangle$, i.e., $\langle f|\,\hat{V}\,|i\rangle \neq 0$. In atomic optical physics, this condition is usually formulated as a set of the so-called "selection rules".

Below we present the selection rules for electric-dipole and magnetic-dipole transitions.

Electric-dipole (E1) transitions

When the wavelength of the electromagnetic field is much larger than the atomic dimensions, the leading term in the interaction between the atom and electromagnetic field is the interaction between the electric component of the field, $\mathbf{E}(t)$, and the induced electric dipole of the atom. Such transitions are known as electric-dipole or E1 transitions.

For our purposes, it sufficient to consider the interaction in a semi-classical picture, where we describe atomic parameters using quantum operators but treat the field as a classical vector. In this picture the interaction term is given by

$$\hat{V}_{\mathrm{d}} = -e\hat{\mathbf{r}} \cdot \mathbf{E}(t), \tag{2.6}$$

Allowed	
$\Delta l = \pm 1$	$\Delta F = 0,\ \pm 1$
$\Delta j = 0,\ \pm 1$	$\Delta m_{\mathrm{F}} = 0,\ \pm 1$

Exceptions
$\Delta m_F = 0$, if $F' = F$ and $m_{\mathrm{F}} = 0$

Table 2.1: Selection rules for E1 transitions in a hydrogen-like atom [70]. Only transitions that satisfy all criteria in the left-hand table, except those indicated in the right-hand table, are allowed. Transitions with $\Delta m_{\mathrm{F}} = 0$ and $\Delta m_{\mathrm{F}} = \pm 1$ are allowed only in the case of π-polarized and $\sigma^{\pm}$-polarized fields, respectively.

where e is the absolute value of the elementary charge, and $\hat{\mathbf{r}}$ is the position of the interacting electron with respect to the nucleus.

The selection rules for E1 transitions are given in Table 2.1[4]. Their unique feature is that the electron orbital number must change by ± 1, which a consequence of the parity of the electric-dipole interaction. The rest of the rules can be understood as conservation laws for a single-photon absorption or emission. Transitions that do not satisfy the selection rules are usually referred to as "forbidden."

Magnetic-dipole (M1) transitions

In a similar way, an oscillating magnetic field $\mathbf{B}(t)$ interacting with the atomic magnetic moment $\boldsymbol{\mu}$ can lead to magnetic-dipole (M1) transitions. In this case, the semi-classical interaction term is $\hat{V}_{\mathrm{m}} = -\hat{\boldsymbol{\mu}} \cdot \mathbf{B}$, with the selection rules provided in Table 2.2. Unlike E1 transitions, M1 transitions require that neither the principle

Allowed	
$\Delta n = 0,\ \Delta l = 0$	$\Delta F = 0,\ \pm 1$
$\Delta j = 0,\ \pm 1$	$\Delta m_{\mathrm{F}} = 0,\ \pm 1$

Exceptions
$\Delta m_F = 0$, if $F' = F$ and $m_{\mathrm{F}} = 0$

Table 2.2: Selection rules for M1 transitions in hydrogen-like atoms [70]. Only transitions that satisfy all criteria in the left-hand table, except those indicated in the right-hand table, are allowed. Transitions with $\Delta m_{\mathrm{F}} = 0$ and $\Delta m_{\mathrm{F}} = \pm 1$ are allowed only in the case of π-polarized and $\sigma^{\pm}$-polarized fields, respectively.

nor the orbital quantum numbers of the electronic wave function change. Classically,

[4]Polarization types are discussed in Appendix B

it can be explained by the fact that the magnetic-dipole interaction cannot change either the electron's kinetic or Coulomb energies. Besides, the opposite parities of the electric-dipole and the magnetic-dipole operators guarantee that the corresponding transitions are mutually exclusive. As a result, only one or neither of them can be allowed between two given states. In our experiments, E1 transitions correspond to optical frequency range and connect states from different fine-structure levels. Meanwhile, M1 transitions due to microwave fields are used to couple the two hyperfine levels of the ground state.

2.3.2 Quantum evolution

To show how the atomic state evolves during a transition, we will consider only two atomic levels and assume that the frequency of the electromagnetic field driving this transition is close to the transition frequency. This is known as the two-level system approximation, and it is sufficient to understand most of the effects in atomic optical physics.

Experimentally, it is impossible to have a fully isolated atomic system since there will always be some interactions with the environment and the vacuum electromagnetic field. These interactions lead to spontaneous transitions between quantum states and quantum decoherence of the wavefunction. We will call these processes relaxation and consider their effect on the two-level system evolution phenomenologically. Qualitatively, depending on how the coupling strength Ω_{R} between the driving field and the two-level system compares to the relaxation rate Γ, we can separate two limiting cases:

1. $\Omega_{\mathrm{R}} \gg \Gamma$. In this case, the system undergoes coherent Rabi oscillations between the two states [71]. In our experimental setup, it can be observed in M1 transitions.

2. $\Omega_{\mathrm{R}} < \Gamma$. In this case, after a couple of oscillations, the system reaches a steady-

state, a statistical mixture of the two levels that provide a balance between excitation and relaxation. Experimentally, this regime is observed in E1 transitions as resonance fluorescence [72].

We will treat these two cases separately, starting with the more straightforward case of the Rabi oscillations, and then extending to the resonance fluorescence case.

Rabi oscillations

Here we consider a quantum system of two orthogonal non-degenerate levels $|1\rangle$ and $|2\rangle$ separated by $\hbar\omega$, that are coupled by the interaction term $\hat{V}\cos\left[(\omega+\delta)t\right]$, such that the diagonal terms are zero, i.e., $V_{11}=V_{22}=0$, and the off-diagonal terms are equal, i.e., $V_{12}=V_{21}$. For now, we assume that $|1\rangle$ and $|2\rangle$ form a complete basis, and there is no relaxation between these levels. The Hamiltonian of this system in a matrix form is given by

$$\hat{H}=\frac{\hbar\omega}{2}\begin{pmatrix}1 & 0\\ 0 & -1\end{pmatrix}+\frac{\hbar\Omega_{\mathrm{R}}}{2}\begin{pmatrix}0 & 1\\ 1 & 0\end{pmatrix}\cos\left[(\omega+\delta)t\right]=\frac{\hbar\omega}{2}\hat{\sigma}_z+\hbar\Omega_{\mathrm{R}}\hat{\sigma}_x\cos\left[(\omega+\delta)t\right], \tag{2.7}$$

where $\hat{\sigma}_x$ and $\hat{\sigma}_z$ are the Pauli matrices in the basis of $|1\rangle$ and $|2\rangle$, and $\Omega_{\mathrm{R}}=V_{12}/\hbar$ is the coupling strength, also know as the Rabi frequency.

In general, the system's quantum state is defined as a time-dependent vector $|\psi(t)\rangle$ in the basis of $|1\rangle$ and $|2\rangle$. We will describe the two-level system in terms of the pseudo-spin $\boldsymbol{\nu}$, also known as the Bloch vector, defined as

$$\boldsymbol{\nu}(t)=\langle\hat{\boldsymbol{\sigma}}\rangle(t)=\langle\psi(t)|\,\hat{\boldsymbol{\sigma}}\,|\psi(t)\rangle\,, \tag{2.8}$$

where $\hat{\boldsymbol{\sigma}}$ is a three-dimensional vector whose components are the Pauli matrices. In this definition, the x and y components of the pseudo-spin are proportional to the real and imaginary parts of the coherence between the two levels, respectively. The z component equals the population inversion $|\langle 2|\,\psi(t)\rangle|^2-|\langle 1|\,\psi(t)\rangle|^2$. Note that the pseudo-spin coefficients are real numbers, and they uniquely define the quantum

state $|\psi(t)\rangle$. A set of all possible pseudo-spin vectors forms a sphere of unit radius, known as the Bloch sphere.

Next, we will rewrite[5] the two-level Hamiltonian as a linear combination of the Pauli matrices and the unit-matrix $\hat{1}$ i.e,

$$\hat{H} = \frac{\hbar}{2}\left(\Omega_0\hat{1} + \Omega_x\hat{\sigma}_x + \Omega_y\hat{\sigma}_y + \Omega_z\hat{\sigma}_z\right) = \frac{\hbar}{2}\left(\Omega_0\hat{1} + \boldsymbol{\Omega}\cdot\hat{\boldsymbol{\sigma}}\right), \tag{2.9}$$

where $\boldsymbol{\Omega}$ is a real vector that we will call the pseudo-field. It can be shown that the evolution of a two-level system in terms of the pseudo-spin and pseudo-field satisfies [73]

$$\dot{\boldsymbol{\nu}}(t) = \boldsymbol{\Omega}(t) \times \boldsymbol{\nu}(t), \tag{2.10}$$

which is analogous to the classical equation describing a gyromagnetic system interacting with a time-dependent magnetic field. In the case of a time-independent Hamiltonian, the pseudo-spin precesses around the axis of $\boldsymbol{\Omega}$ [see Figure 2.4(a)] at a frequency $\Omega = |\boldsymbol{\Omega}|$.

Let us consider the Hamiltonian in Eq. 2.7 when $\Omega_{\mathrm{R}} = 0$, so there are no time-dependent terms. In this case $\boldsymbol{\nu}$ precesses around the z-axis at a frequency ω. We can simplify the problem by going to a frame of reference rotating around the z-axis at frequency $\omega + \delta$ in the direction of precession. Mathematically, such transformation is given by a unitary operator

$$\hat{U}(t) = \exp\left[-i(\omega+\delta)t\frac{\hat{\sigma}_z}{2}\right] = \hat{1}\cos\frac{\omega+\delta}{2}t - i\hat{\sigma}_z\sin\frac{\omega+\delta}{2}t. \tag{2.11}$$

In the rotating frame, the original Hamiltonian from Eq. 2.7 is replaced with

$$\hat{H}' = \hat{U}^{-1}\hat{H}\hat{U} + i\hbar\frac{d}{dt}\left(\hat{U}^{-1}\right)\hat{U} = \frac{\hbar}{2}\left(\Omega_{\mathrm{R}}\hat{\sigma}_x - \delta\hat{\sigma}_z + \hat{W}(t)\right), \tag{2.12}$$

where $\hat{W}(t) = \hat{\sigma}_x\cos\left[2(\omega+\delta)t\right] + \hat{\sigma}_y\sin\left[2(\omega+\delta)t\right]$ corresponds to a pseudo-field rotating in the new frame around the z-axis at a frequency $2(\omega+\delta)$. Provided that

[5] This can be done for any Hermitian operator from the 2D matrix space.

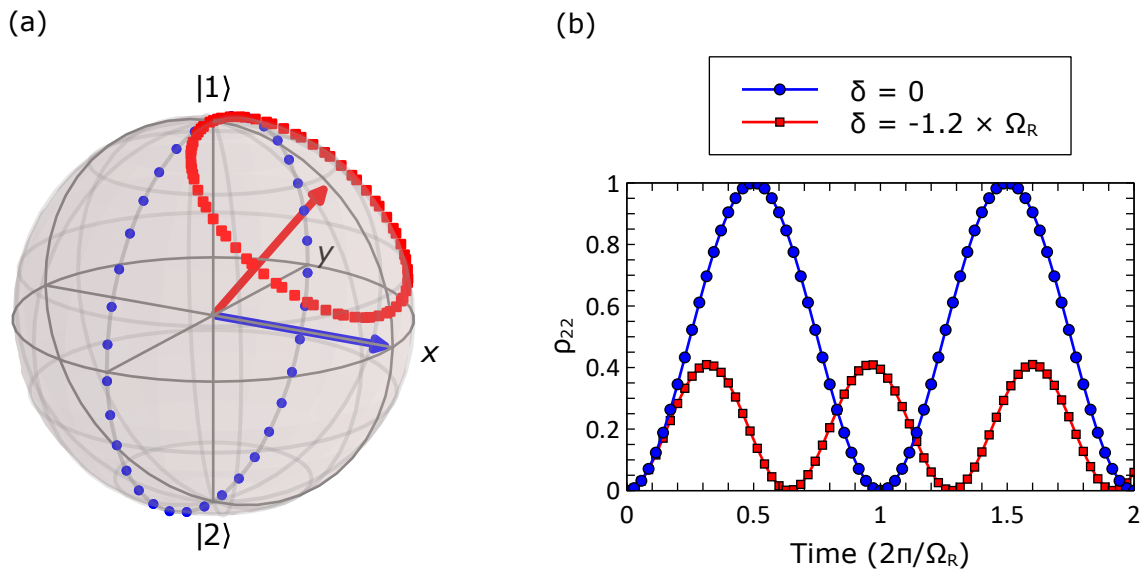

Figure 2.4: Evolution of a two-level system in the rotating frame due to the rotating-wave Hamiltonian in Eq. 2.13 for two values of detuning $\delta = 0$ (blue circles) and $\delta = -1.2 \times \Omega_{\mathrm{R}}$ (red squares). The simulation is done in QuTiP [74, 75]. For the simulation, the system is initially in state $|1\rangle$, and we use units such that $\hbar\Omega_{\mathrm{R}} = 1$. (a) Pseudo-spin precession on the Bloch sphere around the pseudo-field vector. The pseudo-field direction is indicated with an arrow. (b) Rabi oscillations of the excited state population.

$\sqrt{\Omega_{\mathrm{R}}^2 + \delta^2} \ll \omega$, the effect of the counter-rotating term $\hat{W}$ can be neglected, resulting in the Hamiltonian

$$\hat{H}' = \frac{\hbar}{2}\left(\Omega_{\mathrm{R}}\hat{\sigma}_x - \delta\hat{\sigma}_z\right). \tag{2.13}$$

In the laboratory frame, this is equivalent to replacing the linearly-polarized field with a rotating field, so this approximation is known as the rotating-wave approximation.

In the rotating-wave approximation, the evolution of a two-level system in the rotating frame is a precession of the pseudo-spin around the pseudo-field vector $\mathbf{\Omega}' = (\Omega_{\mathrm{R}}, 0, -\delta)$. If at $t = 0$ the system is in state $|1\rangle$, the probability of the system being measured in state $|2\rangle$ oscillates in time as

$$P_2(t) = |\langle 2|\,\psi(t)\rangle|^2 = \frac{\nu_z(t) + 1}{2} = \frac{\Omega_{\mathrm{R}}^2}{\Omega_{\mathrm{R}}^2 + \delta^2}\sin^2\frac{\sqrt{\Omega_{\mathrm{R}}^2 + \delta^2}}{2}t. \tag{2.14}$$

These oscillations are known as the Rabi oscillations and are depicted in Figure 2.4(b). On resonance, the system's population harmonically oscillates between the two states at the Rabi frequency Ω_{R}. Note that this probability does not depend on the reference frame, and is the same if we measure the system in the laboratory frame.

Damped Rabi oscillations

Whenever there is relaxation or decoherence in a quantum system, we can no longer use a single wavefunction to describe the system's state. Instead, the system is characterized by a statistical mixture of wavefunctions, known as a mixed state. Mathematically, a mixed quantum state can be described in terms of the density matrix $\hat{\rho} = \sum_k p_k \left|\psi_k\right\rangle \left\langle\psi_k\right|$, where p_k is the probability of the system being in a state $\left|\psi_k\right\rangle$.

The density matrix evolution in an open system is given by the Lindblad master equation [76]

$$\frac{d}{dt}\hat{\rho} = -\frac{i}{\hbar}\left[\hat{H}, \hat{\rho}\right] + \sum_n \frac{1}{2}\left(2\hat{L}_n\hat{\rho}\hat{L}_n^\dagger - \hat{\rho}\hat{L}_n^\dagger\hat{L}_n - \hat{L}_n^\dagger\hat{L}_n\hat{\rho}\right), \tag{2.15}$$

where $\hat{L}_n$ are referred to as collapse operators, and the summation goes over all relaxation processes. The decay of the population from state $\left|2\right\rangle$ to state $\left|1\right\rangle$ at rate γ_1 is described by collapse operator $\hat{L}_1 = \sqrt{\gamma_1}\left|1\right\rangle\left\langle 2\right|$. In terms of the pseudo-spin vector, which is redefined below, this type of relaxation affects the z-component and is therefore known as longitudinal relaxation. According to Eq. 2.15, longitudinal relaxation at rate γ_1 is accompanied by the damping of the off-diagonal density matrix elements, known as transverse relaxation, at rate $\gamma_1/2$. In some situations, quantum systems can have transverse relaxation between two levels that does not affect their populations. In this case, the collapse operator is given by $\hat{L}_2 = \sqrt{\frac{\gamma_2}{2}}\hat{\sigma}_z$, where γ_2 is the transverse relaxation rate.

For a mixed state, the pseudo-spin definition from Eq. 2.8 should be generalised as

$$\boldsymbol{\nu}(t) = \langle\hat{\boldsymbol{\sigma}}\rangle(t) = \mathrm{Tr}\left[\hat{\rho}(t)\cdot\hat{\boldsymbol{\sigma}}\right], \tag{2.16}$$

where the pseudo-spin components have the same physical meaning as before. The two-level system master equation in terms of the pseudo-spin has the following form:

$$\dot{\boldsymbol{\nu}}(t) = \boldsymbol{\Omega}(t) \times \boldsymbol{\nu}(t) - \begin{pmatrix} \Gamma_2 \nu_x \\ \Gamma_2 \nu_y \\ \Gamma_1 \nu_z \end{pmatrix} - \begin{pmatrix} 0 \\ 0 \\ \Gamma_1 \end{pmatrix}, \tag{2.17}$$

where Γ_1 and Γ_2 are the total longitudinal and transverse relaxation rates, respectively. If the pseudo-field $\boldsymbol{\Omega}$ does not depend on time, Eq. 2.17 has the stationary solution $\boldsymbol{\nu}(t) = \boldsymbol{\nu}_\mathrm{s}$, such that $\dot{\boldsymbol{\nu}}_\mathrm{s}(t) = \mathbf{0}$, known as the steady-state. In the case of $\Gamma_1 \neq 0$, the steady-state does not depend on the initial conditions and is uniquely defined by the pseudo-field and the relaxation rates. For the Hamiltonian in Eq. 2.13, the steady-state pseudo-spin is given by

$$\boldsymbol{\nu}_\mathrm{s} = \frac{-1}{\Gamma_2^2 + \delta^2 + \Omega_\mathrm{R}^2 \frac{\Gamma_2}{\Gamma_1}} \begin{pmatrix} \Omega_\mathrm{R} \delta \\ \Omega_\mathrm{R} \Gamma_2 \\ \Gamma_2^2 + \delta^2 \end{pmatrix}. \tag{2.18}$$

The pseudo-spin evolution is a spiraling motion from the original state towards $\boldsymbol{\nu}_\mathrm{s}$, as is shown in Figure 2.5(a). The analytical solution for population inversion for atoms starting in state $|1\rangle$ is given by [77]

$$\nu_z(t) = \nu_{\mathrm{s},z} - (1 + \nu_{\mathrm{s},z}) e^{-\Gamma_2 t} \left(\cos \Omega' t + \frac{\Gamma_2}{\Omega'} \sin \Omega' t \right), \tag{2.19}$$

where $\Omega' = \sqrt{\Omega_\mathrm{R}^2 + \delta^2}$ [see Figure 2.5(b)]. The excited state population in this case undergoes damped oscillations until it reaches its steady-state value

$$\rho_{22,\mathrm{s}} = \frac{1}{2} \frac{\Omega_\mathrm{R}^2 \frac{\Gamma_2}{\Gamma_1}}{\Gamma_2^2 + \delta^2 + \Omega_\mathrm{R}^2 \left(\frac{\Gamma_2}{\Gamma_1} \right)}. \tag{2.20}$$

According to 2.19, cycles of the damped Rabi oscillations can be observed only when $\Omega' > \Gamma_2$. In our experiments, this condition is satisfied for microwave magnetic-dipole transitions between the two hyperfine ground levels, which allows observing the damped Rabi oscillations as a change in transmission for a resonant light, as will be described in Chapter 3.

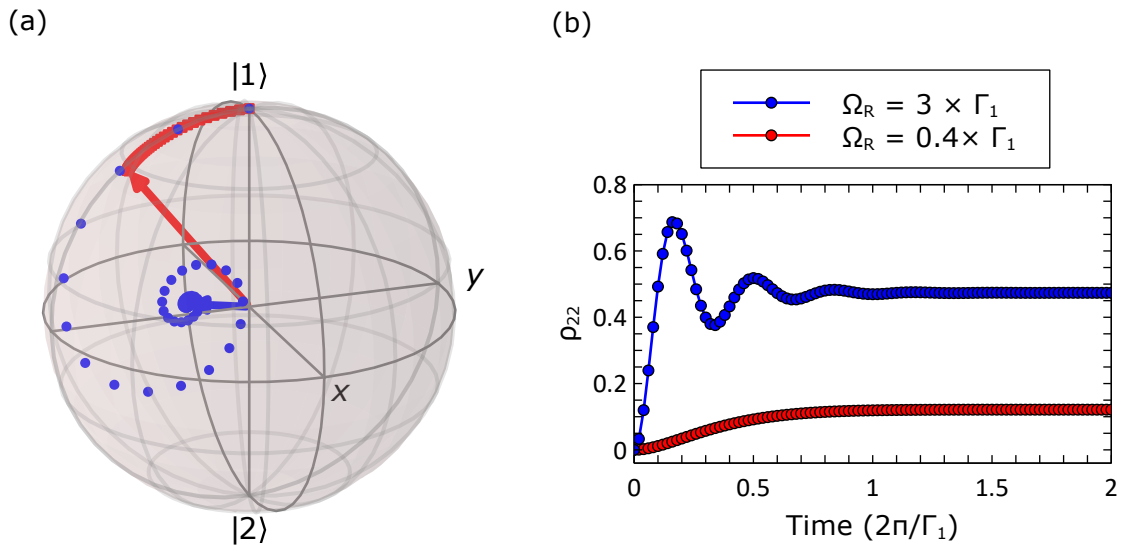

Figure 2.5: Evolution of a two-level system with longitudinal relaxation in the rotating frame due to the rotating-wave Hamiltonian in Eq. 2.13 for two values of the Rabi frequency $\Omega_R = 3 \times \Gamma_1$ (blue circles) and $\Omega_R = 0.4 \times \Gamma_1$ (red squares). The simulation is done in QuTiP [74, 75]. For the simulation, the system is initially in state $|1\rangle$, and we use units such that $\hbar\Gamma_1 = 1$ and $\Gamma_1 = 2\Gamma_2 = \delta$. The pseudo-field direction is along x-axis. (a) Damped pseudo-spin precession on the Bloch sphere around the pseudo-field direction towards the steady-state vector (the steady states are indicated with arrows) (b) Damped Rabi oscillations of the excited state population.

Resonance fluorescence

In the case of optical E1 transitions, there is always transverse and longitudinal relaxation due to spontaneous emission. For the D1 and D2 lines in Rb, the spontaneous emission rate Γ_{sp} is on the order of $2\pi\times$ MHz, which makes observing the Rabi oscillations a non-trivial experimental task that requires relatively large optical intensities and fast detection [78]. In our experiments, we work in a regime where the optical Rabi frequency is much less than the spontaneous emission rate. In this case, the quantum system reaches the steady state directly, as is shown in Figure 2.5. In this state, the system continuously absorbs and emits light at a rate $\Gamma_{sp}\rho_{22,s}$, which results in a fluorescence signal that has a Lorentzian shape in terms of the detuning with a peak at $\delta = 0$. The same shape has the absorption coefficient, which is proportional

to ν_y.

Usually, there is more than one level the excited state can decay to, in which case the two-level approximation is no longer valid. Nevertheless, the results obtained above can provide a good starting point for describing the three-level dynamics.

2.3.3 Optical pumping

Optical pumping is a multilevel effect that can act as a tool for creating a population imbalance between quantum states of an atomic ensemble via interaction with a "pump" light. Here we present the most common optical pumping schemes that rely on transferring the population to states that do not interact with the pump light.

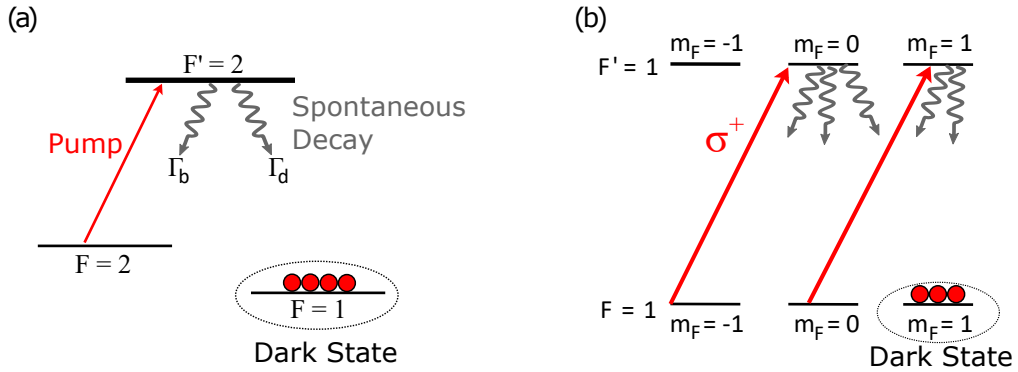

Figure 2.6: Optical pumping schematics. (a) Optical pumping in a Λ-type three-level system. Light resonant with $|F = 2\rangle \rightarrow |F' = 2\rangle$ transition optically pumps atoms to an off-resonant dark state $|F = 1\rangle$. (b) Optical pumping in a system with degenerate Zeeman sublevels. σ^+-polarized pump transfers atoms to a Zeeman state with the highest m_F, which does not interact with the pump due to selection rules.

Figure 2.6(a) illustrates the optical pumping principle in the case of a Λ-type three-level system excited by a monochromatic optical field. The key component for creating the population imbalance is the existence of a "dark" state - a ground state that does not interact with the driving field. The other ground state that is coupled to the field, is known as the "bright" state. If there is a significant energy splitting between the two ground states, the dark state occurs naturally, provided that the pump field frequency is on resonance with a transition between one of the ground

states and the excited state. According to Eq. 2.20, the large detuning between the driving field and the second transition leads to negligible excitation of the second ground state, making it dark. In the example depicted in Figure 2.6(a), the pump light resonant with $|F = 2\rangle \rightarrow |F' = 2\rangle$ transfers atoms from $|F = 2\rangle$ to the excited state, where they can spontaneously decay to either ground state. Atoms that decay into $|F = 2\rangle$ state continue to absorb light until the whole population is accumulated by the off-resonant dark state $|F = 1\rangle$. The optical pumping rate can be estimated as a product of the probability of being in the excited state and the decay rate to the dark state. Provided that the Rabi frequency is much smaller than the spontaneous emission rate in Eq. 2.20, the optical pumping rate for resonant excitation is given by

$$\Gamma_{\mathrm{p}} = \frac{\Omega_{\mathrm{R}}^2}{\Gamma_{\mathrm{b}}^2}\Gamma_{\mathrm{d}}, \tag{2.21}$$

where Γ_{b} and Γ_{d} and are the rates of emission to the bright and dark states, respectively. Here we used the fact that for spontaneous emission $\Gamma_1 = 2\Gamma_2$.

The optical pumping can also be achieved in a degenerate ground-state level if the pump light is polarized. In this case, one of the sublevels becomes dark if it does not interact with the driving field due to the selection rules. For example, a circularly polarized light optically pumps the atomic population to a single Zeeman sublevel, as is shown in Figure 2.6(b). Here, the absorption of a photon changes the atomic magnetic number m_F by one. After several cycles of excitation followed by spontaneous emission, the atomic population accumulates in the dark state that corresponds to either the highest or the lowest m_F depending on the circularity of the pump field.

2.4 Ensemble effects

So far, we have considered a quantum system as if it was a single particle. This approximation may be valid for an ensemble of identical particles, provided all particles interact with the driving field and the environment in the same way. In this

case, these interactions have the same effect on the ensemble's quantum state as on the quantum state of each individual particle. One example of such effects is the homogeneous broadening of the fluorescence and absorption resonances due to spontaneous emission. For E1-transitions, spontaneous emission leads to relaxation that broadens the resonance line according to Eq. 2.20. For atoms of the same isotope, this relaxation happens at the same rate. As a result, during the interaction with the external field, all atoms are in a state with the same density matrix. The ensemble resonance line, representing the steady-state fraction of atoms in the excited state, is the same as $\rho_{22,\mathrm{s}}$ of an individual atom.

If different parts of the ensemble interact with an external field differently, for example, due to atomic motion or the field inhomogeneity, they will end up in different states with different resonance lines. In terms of the ensemble, these effects can be taken into account as an additional relaxation or a shift and broadening of the resonance line. Below we will discuss some examples of these effects relevant to our experiments.

2.4.1 Doppler broadening

Due to the Doppler effect, atoms that move relative to each other interact with a traveling electromagnetic wave differently. In thermal atomic ensembles, it leads to a significant inhomogeneous broadening of optical transitions, known as the Doppler broadening.

To illustrate this effect, let us consider a single atom moving in the laboratory frame with velocity $\mathbf{v}$ that interacts with a traveling wave with a wave-vector $\mathbf{k}$, as is shown in Figure 2.7(a). In a non-relativistic case, the frequency of the field in the atomic rest frame is shifted by $-\mathbf{k}\cdot\mathbf{v}$. As a result, the resonance line of a moving atom is frequency-shifted with respect to the stationary atom's line. The value and sign of the this shift is proportional to the atom's velocity component along the wave-vector [see Figure 2.7(b)]. Atoms, whose velocities differ only by an infinitesimal value, have the

same resonance lines. We will call this group of atoms a velocity class. The fact that different velocity classes have different resonance frequencies in the laboratory frame leads to a broadening of the ensemble resonance, known as the Doppler broadening.

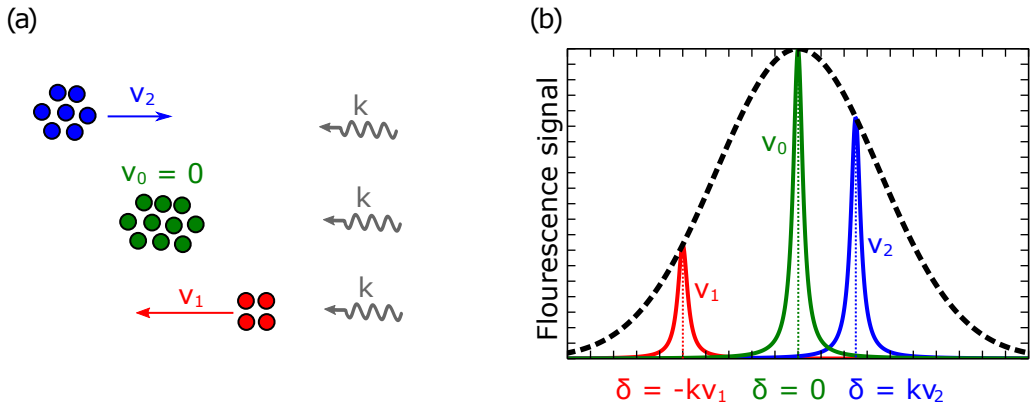

Figure 2.7: (a) Illustration of three different atomic velocity classes defined with respect to the wave-vector $\boldsymbol{k}$ of a driving optical field. The ensemble temperature determines the fraction of atoms in a particular velocity class. (b) Resonance lines for three different velocity classes (solid curves) weighted by the corresponding fractions of atoms in those velocity classes, as is determined by the Maxwell-Boltzmann distribution (black dashed curve). The central line corresponds to the zero-velocity class.

In a thermal ensemble, atoms occupy velocity classes according to the Maxwell-Boltzmann distribution

$$g_{\mathrm{MB}}(v) = \sqrt{\frac{m}{2\pi k_{\mathrm{B}} T}} \exp\left(-\frac{mv^2}{2k_{\mathrm{B}}T}\right), \tag{2.22}$$

where $g_{\mathrm{MB}}(v)$ is the fraction of atoms in a velocity class v, m is the atom's mass, T is the ensemble temperature, and k_B is the Boltzmann constant. Assuming that the only source of relaxation is the spontaneous decay, for each velocity class the resonance line is a Lorentzian centered around $\delta_0 = -\mathbf{kv}$:

$$L(\delta, v) = \frac{\Omega_{\mathrm{R}}^2 \Gamma_{\mathrm{sp}}}{\Gamma_{\mathrm{sp}}^2 + 4(\delta - \mathbf{kv})^2 + 2\Omega_{\mathrm{R}}^2}, \tag{2.23}$$

where δ is the detuning from the resonance of the zero-velocity class. The ensemble resonance line will be a sum of contributions from all velocity classes, weighted by the

fraction of atoms occupying that velocity class. Mathematically, it can be expressed as a convolution

$$g_{\mathrm{V}}(\delta) = \int_{-\infty}^{+\infty} L(\delta, v) g_{\mathrm{MB}}(v) dv, \tag{2.24}$$

known as the Voight profile. Physically, $g_{\mathrm{V}}(\delta)$ corresponds to the steady-state fraction of the excited atoms in the ensemble driven by a field detuned from the zero-velocity class resonance by δ. In the case when $k_{\mathrm{B}}T \gg \hbar\Gamma_{\mathrm{sp}}$, $g_{\mathrm{V}}(\delta)$ can be approximated by a Gaussian with characteristic width proportional to $\sqrt{T}$.

In a room-temperature ^{87}Rb vapor, the Doppler broadening, defined as the full width at half maximum of the Voigt profile, for D1 and D2 lines is on the order of $2\pi \times 100$ MHz, which is much larger than the hyperfine splitting in the excited state. As a result, a single laser field cannot resolve transitions to different hyperfine states for states originating from the same ground level. On the other hand, the Doppler shift for microwave fields is negligible because of a small k. Thus, combining optical and microwave transitions in the double-resonance imaging, as will be discussed in Chapter 3, allows us to resolve hyperfine transitions whose linewidth is of many orders of magnitude smaller than the Doppler width of the optical line.

2.4.2 Transverse relaxation due to inhomogeneous static field

In this section, we want to describe how an external field's inhomogeneity leads to transverse relaxation in an ensemble. As an example, we will consider an ensemble of two-level systems in an inhomogeneous magnetic field. We assume that at least one of the levels is susceptible to the linear Zeeman effect, and there are no other interactions or relaxations in the ensemble. According to Eq. 2.10, the two-level system evolution is a precession of the pseudo-spin around the pseudo-field. In our case, the pseudo-field vector is proportional to the magnetic field.

Next, we assume that the magnetic field vector points in one direction everywhere, but its magnitude varies across the spatial extent of the ensemble. In this situation, all

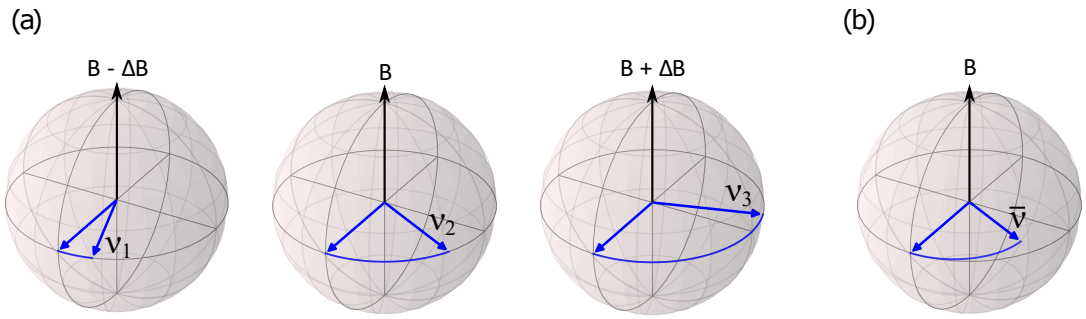

Figure 2.8: Illustration of a spatially-inhomogeneous magnetic field (a) Pseudo-spins at different locations experience different magnetic field, which affects their precession frequencies. (b) Misalignment of the individual pseudo-spins due to the difference in angular frequencies leads to a decrease in the transverse component of the average pseudo-spin $\bar{\nu}$.

pseudo-spins precess around the same axis, but their precession frequency varies across the ensemble, as is shown in Figure 2.8(a). As a result, after some time, the transverse pseudo-spin components of different parts in the ensemble diverge, causing a reduction in the average transverse component, as is illustrated in Figure 2.8(b). Effectively, this is equivalent to transverse relaxation of the ensemble pseudo-spin, even though there is no relaxation for each individual two-level system. The same effect occurs for any pseudo-field $\mathbf{\Omega}$, that is spatially inhomogeneous across an ensemble of two-level systems.

2.4.3 Relaxation due to thermal motion

Another type of inhomogeneous relaxation occurs if the external field is spatially limited and occupies a smaller volume, which we will call the interrogation region, than the size of the ensemble. In this case, only a part of the ensemble interacts with the field at a given time. When describing the quantum state of the ensemble, we can focus our attention only on this interacting part and treat the rest of the ensemble as the environment. In this case, in terms of the interrogated ensemble, the exchange of particles between the interrogation region and the environment acts as a relaxation.

Figure 2.9 illustrates this idea using a hypothetical pump and probe experiment broken into stages. Here the interrogation region is defined as the space occupied by the laser beam. Let us assume, that before the experiment all atoms in the cell are in state $|1\rangle$. During the first stage [see Figure 2.9(a)], a laser pulse optically pumps all atoms within the interrogation region into state $|2\rangle$, in which case the quantum state of the ensemble within the interrogation region is $\hat{\rho}_1 = |2\rangle\langle 2|$.

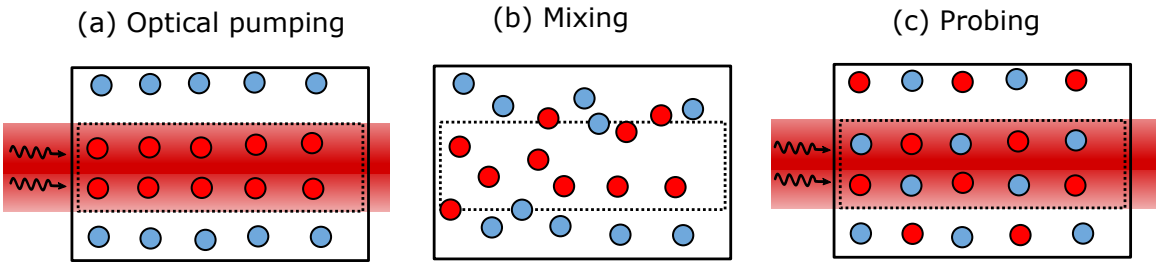

Figure 2.9: Illustration of the concept of relaxation due to thermal motion. (a) A laser pulse pumps atoms into state $|2\rangle$, represented by red circles. (b) Atoms in states $|1\rangle$ (blue circles) and $|2\rangle$ mix via thermal motion. (c) When probed with the same laser beam, the ensemble population of state $|2\rangle$ after mixing is less than right after the optical pumping, meaning that thermal motion act as a relaxation. In all figures the interrogation region is enclosed by the dashed rectangle.

Next, we let atoms fully mix via to thermal motion [see Figure 2.9(b)] and probe the ensemble with the same beam [see Figure 2.9(c)]. If we assume that atomic state is preserved and that the atoms are uniformly distributed across the cell, the fraction of atoms found in the state $|2\rangle$ is given by the ratio of the interrogation region volume to the total volume of the cell. In terms of the interrogation, the thermal motion results in the relaxation of the ensemble to the state

$$\hat{\rho}_2 = \left(1 - \frac{V_i}{V_c}\right)|1\rangle\langle 1| + \frac{V_i}{V_c}|2\rangle\langle 2|\,, \tag{2.25}$$

where V_i and V_c are the volumes of the interrogation region and the cell, respectively. If the atomic state is affected by the collisions with other atoms and with the cell wall, the relaxation is directed toward the density matrix of thermal equilibrium, e.g., $\hat{\rho} = |1\rangle\langle 1|$.

Chapter 3

Microwave-optical double resonance

In this chapter we present the microwave-optical double resonance - a phenomenon at the core of our transduction experiments. The double resonance method originates in spectroscopy [39], where it allows detection of hard-to-observe microwave and radio-frequency transitions via their effect on the absorption of light in the sample medium. In the context of our experiment, double resonance manifests itself as a change in the absorption of a resonant optical field in a rubidium vapor as a result of a non-linear coupling to a magnetic component of a microwave field resonant with a hyperfine transition. This effect is the strongest when both fields are on resonance with their corresponding transitions, giving the technique its name.

We begin by introducing the physical principle and theoretical model of the double resonance method. Next, we describe the apparatus and experimental procedures. Finally, we present a set of measurements performed to characterize our experimental system and develop a better understanding of the technique. These results provided us with essential insights leading to the development of our method of microwave-to-optical transduction, and they lay the foundation of the work presented in the remaining chapters.

3.1 Principle

To illustrate the double resonance principle, let us consider a lambda-type three-level system with two ground-state levels $|1\rangle$ and $|2\rangle$, and an excited state $|e\rangle$. The ground levels are connected by an M1 microwave transition, and each of them can couple to the excited state via an E1 optical transition. As was discussed in Section 2.3.3, an oscillating electric field resonant with the $|2\rangle \rightarrow |e\rangle$ transition will optically pump the atomic population to the dark state $|1\rangle$, and the medium becomes transparent for this field [Figure 3.1(a)]. We will call this field the "probe". If a microwave field is simultaneously driving the $|1\rangle \rightarrow |2\rangle$ transition, then for the total field, $|2\rangle$ is no longer a dark state, and the atomic population is redistributed between $|1\rangle$ and $|2\rangle$ to achieve a balance between the microwave drive and the optical pumping. As a result, the medium is not fully transparent for the probe, with the transmission coefficient T depending on the microwave parameters [Figure 3.1(b)].

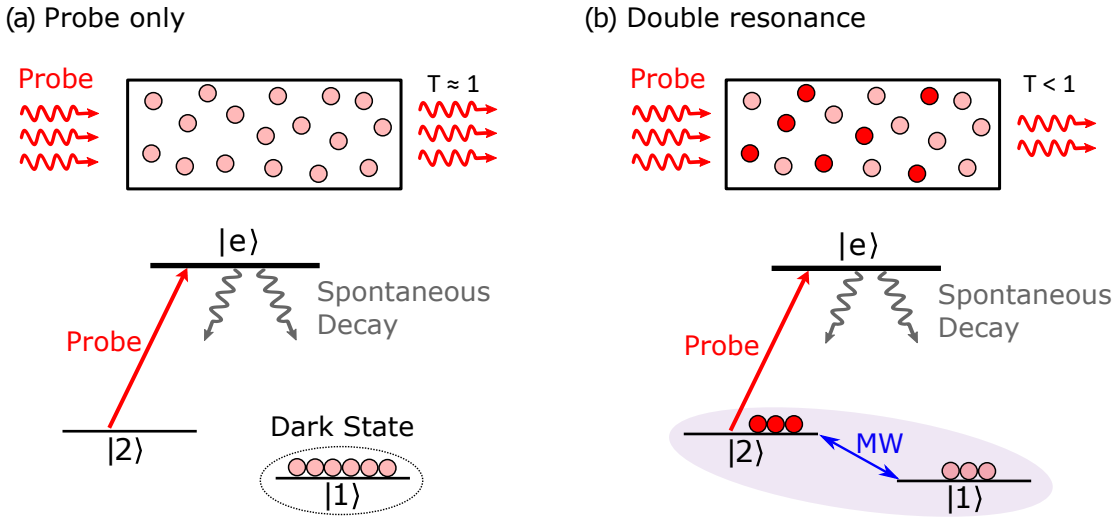

Figure 3.1: Schematics of the double resonance in a three-level Λ system. (a) The probe field resonant with $|2\rangle \rightarrow |e\rangle$ transition optically pumps the atomic population to the dark state $|1\rangle$, which results in an increased steady-state transmission T. (b) A microwave field driving $|1\rangle \rightarrow |2\rangle$ creates coherence and redistributes the atomic population between the ground-state levels. In this case the probe transmission depends on the microwave parameters.

In the case of a dilute vapor, the probe transmission linearly depends on the atomic population in state $|2\rangle$, corresponding to the density-matrix element ρ_{22}. It can be seen from the Beer-Lambert law, where the transmission is given by

$$T = e^{-n\rho_{22}l\sigma} \approx 1 - n\rho_{22}l\sigma, \tag{3.1}$$

where n is the vapor density, l is the optical path length, and σ is the absorption cross-section.

If the optical pumping rate Γ_p (see Eq. 2.21) is much larger than the microwave Rabi frequency, we can exclude the excited state $|e\rangle$ from the description of the system's dynamics by treating the optical pumping as a longitudinal relaxation from $|2\rangle$ to $|1\rangle$ at the rate Γ_p. In this two-level approximation, the steady-state population in level $|2\rangle$ is described by Eq. 2.20, which is a Lorentzian centered at the resonance frequency of the $|1\rangle \rightarrow |2\rangle$ transition. By combining Eq. 2.20 and Eq. 3.1, we can see that the steady-state probe transmission depends on the microwave detuning as a negative Lorentzian, with a dip when the microwave field is on resonance with the corresponding transition. This allows detection of microwave transitions with an optical signal, which can be used to measure a static magnetic field (see Section 3.6.2) or to provide a microwave frequency standard [35–38]. The fact that the probe transmission is linear in ρ_{22} provides the basis for the microwave-to-optical transduction.

3.2 Experimental setup

Figure 3.2 illustrates the experimental setup for the double-resonance imaging and microwave-to-optical transduction in warm atomic vapors in our experiments (the setup for the cold-atom experiment will be described in Chapter 5). Below I describe the key components of the setup.

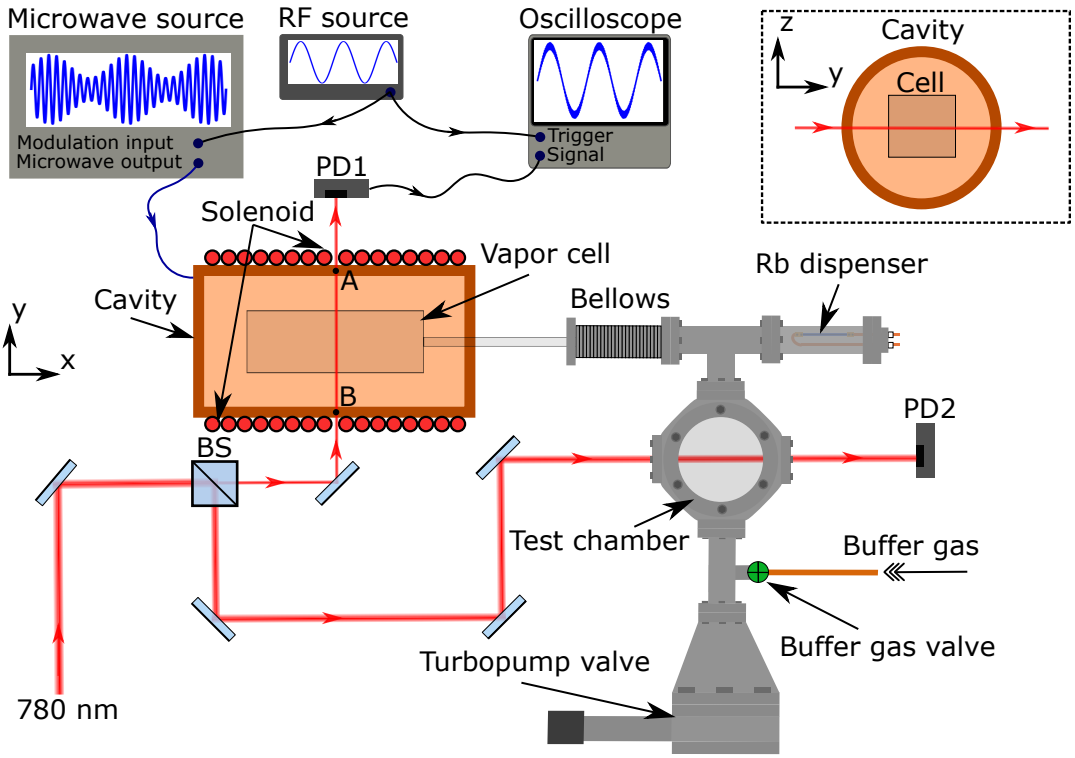

Figure 3.2: Schematics of the experimental setup for microwave to optical transduction experiments in warm rubidium vapor. Helmoltz coils for bias fields are not shown. Relative dimensions of the components are not preserved. The signal from radio-frequency (RF) source provides modulation input for the microwave source and triggers the oscilloscope. Points A and B indicate holes drilled for optical access. The inset shows the cavity cross-section in the yz plane.

3.2.1 Vacuum system

The rubidium vapor is prepared in a stainless-steel vacuum system connected to a vapor cell located inside a microwave cavity The system was initially assembled by Clinton Potts and Timothy Lee and later modified by Timothy and myself. ConFlat technology provides the sealing for the connections between components. The system is evacuated with a turbopump connected via an angle- or a gate-valve.

3.2.2 Vapor cell

The transduction is realized in a quartz cell, centered inside a high-Q copper microwave cavity. The cell's location and dimensions are chosen to enclose the region

where the microwave field is most strongly localized. The cell's dimension along x, y, and z axes are 30, 12.5, and 12.5 mm, respectively. A hollow "stem" is attached to one end of the cell and connected to the rest of the vacuum system via a bellows, with the connections sealed with Viton o-rings. The cavity has a pair of holes drilled across its body (at points A and B in Figure 3.2) to provide optical access to the cell.

3.2.3 Microwave cavity

We use the cavity, designed and manufactured by Clinton Potts, to amplify the magnetic-field component of the microwave field. The cavity has a cylindrical shape and supports the TE_{011} mode [79] at around 6.8 GHz, with the magnetic field oscillating along the x-axis. The cavity length with both caps is around 57 mm, and we can tune the exact resonance frequency by adjusting the position of one of the caps. The inner and outer diameters are 58 and 68 mm, respectively. The copper's high quality and surface treatment provide the cavity with a quality factor of $Q \approx 27000$ at room temperature. As a result, the microwave field can be transmitted to the cavity via SMA cable or over free space via antennas directly from the microwave source without an intermediate amplification. A pair of holes were drilled across the cavity body to provide optical access to the cell.

3.2.4 Rubidium source

We introduce the atoms to the system by running an electric current through a dispenser: a metallic strip containing the rubidium salt of chromic acid (Rb_2CrO_4). The heat produced by the electric current breaks down the salt, and the released Rb vapor fills the whole system. By changing the electric current, we can control Rb's steady-state concentration in the system.

3.2.5 Optical probe

For the optical probe, we use light from an external-cavity diode laser at around 780.24 nm derived from the optical system used in ultracold atom experiments carried out in our lab [80–83]. In Section 3.5 we discuss the particular optical transitions used for the probe. The laser operates in a continuous-wave regime at constant frequency and power, with the setup for optical frequency and power control described in [81]. We used optical power in range from 10 to 300 μW, with a typical beam waist around 2 mm. A fast amplified photodetector (PD1 in Figure 3.2) converts the probe power transmitted through the cell to a voltage signal, which is then displayed and recorded on a digital oscillograph. For a typical probe power of $10-20$ μW we set the detector's amplification to 60 dB.

3.2.6 Electronics

Depending on the availability, we borrowed from the Davis lab the following microwave sources from Berkeley Nucleonics': either model 845 or model 865. For microwave modulation we used an external signal from radio-frequency source Agilent 33220A. We use the same signal also as the oscilloscope trigger for the optical signal detection and averaging.

To control the static magnetic field in the vapor cell, we use a solenoid wrapped around the cavity and two pairs of Helmholtz coils whose axes are orthogonal to each other and the cavity axis. The typical currents are on the order of 10 mA, and are adjusted by observing the double-resonance signal of Zeeman level described in Section 3.6.2. The typical magnetic field magnitude is on the order of 0.1 G.

3.2.7 Buffer gas compatibility

Vapor-cell atomic microwave frequency standards are usually filled with a buffer gas [84], consisting of atomic or molecular species or a mixture of species weakly interacting with the atoms of interest. A buffer gas effectively "freezes" the thermal

motion of the atoms, increasing the microwave interrogation time, reducing Doppler broadening, and suppressing the relaxation due to spin-flipping collision with the cell walls. On the other hand, collisions with the buffer gas lead to a pressure-dependent shift of the transition frequency and broadening of the resonance.

Our warm-atoms system supports a buffer gas injection, but several trials with dry nitrogen as a buffer gas did not show any benefits for our experimental purposes. While it needs additional investigation, we were satisfied with our system's performance and did not use any buffer gas in our experiments.

3.3 System preparation

Before assembling the vacuum system, the inner walls of its stainless steel components need to be properly cleaned and dried. The cleaning procedure that we follow in our lab is described in [80]. We evacuate the air from the system with a turbopump. To desorb water residues and other contaminants from the inner walls, we "bake" the system by wrapping metallic parts with heater tape and aluminum foil and gradually raising the temperature to 100^0C. During the bake, we also run about 3 A of current through the dispenser to desorb contaminants. Typically, we bake the system for a day or over the weekend after each time the dispenser is replaced. Before we stop baking, we activate the dispenser by gradually increasing the current to 5 A. At this point, laser absorption and fluorescence can be observed in the test chamber. We finish baking by gradually lowering the temperature, closing the pump valve, and switching off the pump.

During the first experimental trial, we could not detect any absorption of the light coming through the cavity and vapor cell, which was an indicator of low Rb concentration there. We speculated that the most probable causes of this problem could be the absorption of atoms by the cell walls or a high differential pressure due to a narrow connection between the vapor cell and the system. Since the latter problem would require a redesign of the system, we decided to focus on the other issue.

Fortunately for us, a similar problem was encountered in the experimental set up for Rb-based atomic clock described in [85], where the proposed solution was curing the cell with rubidium. We decided to give it a try and performed curing by running the dispenser at 6.4 A overnight while keeping the system at 50 ^{0}C. After that, we were able to observe the absorption in the vapor cell. Since then, the dispenser had performed as intended producing rubidium as the current is applied.

3.4 System troubleshooting

In this section, we discuss some issues we encountered in the experimental setup described above and the actions we took to analyze and resolve those issues.

3.4.1 Test chamber

During our first experimental trials, we had issues with detecting any absorption signal in the vapor cell, so we introduced a small test chamber connected via a Tee to the dispenser and the bellows. Because of good optical access and a higher optical density compared to the cell, the chamber gives a better absorption signal to characterize the dispenser performance. To produce this signal, we divide the probe into two beams with a beamsplitter ["BS" in Figure 3.2] before the cavity and send one of the beams through the test chamber towards photodetector PD2. In addition, the test chamber's top window allows observing resonance fluorescence with a near-infrared viewer [see Figure 3.3(a)], which gives a quick check of the laser frequency stability or suggests that there is no rubidium in the system.

3.4.2 Rb dispenser issues

We noticed that in our system, the dispenser performance degrades over time, as we needed to increase the electric current to maintain the absorption signal. Additionally, the time interval between applying the current and observing an increase in the probe absorption increased. At some point, the dispenser stopped releasing rubidium

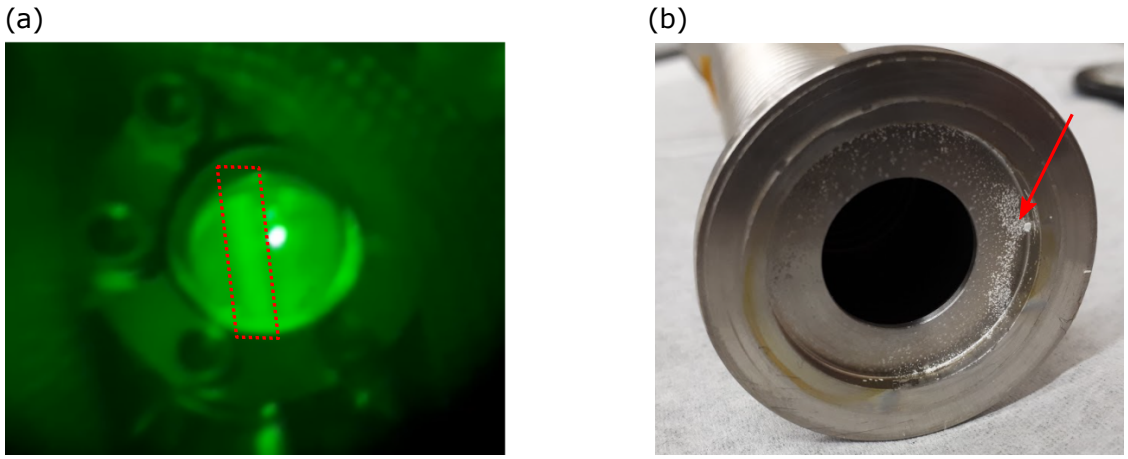

Figure 3.3: (a)Fluorescence from a laser beam in the characterization chamber observed with a near-infrared viewer. The beam is highlighted with a red dashed curve. The picture is taken on a smartphone camera. (b) A white residue can be seen at the end of the bellows connecting the vapor cell to the vacuum system. The red arrow indicates a large residue conglomerate.

and had to be replaced. We were able to prolong the dispenser's lifetime to one month by pumping out the system overnight with the dispenser current set to 3 A. Yet, this lifespan is inferior compared to the ultrahigh-vacuum systems for cold-atom experiments [80] where a single dispenser can operate for years.

The most probable potential reason for the dispenser degradation is the high presence of reactive gaseous contaminants, such as oxygen, that would chemically interact with an activated dispenser. To test for the leaks in the system, we ran a couple of helium leak-checks. In this procedure, we connected our system to a pump with a built-in helium detector and sprayed helium gas around the connections between the system's parts. Because the helium has the smallest atomic size among the elements, it would infiltrate the system through the location of the leak and reach the detector. In our case, no leak was detected, and we were not able to identify the exact cause of the problem. Another possible explanation is that our system did not operate under ultra-high vacuum conditions, which would require more advanced pumping and sealing technology. Practically, it means that even though there is no apparent leak in the system, smaller atoms or molecules can penetrate one by one, causing

degradation in the long term.

While we continued with our measurements replacing the dispensers as needed, we decided to replace our cell with a custom-made sealed cell filled with enriched ^{87}Rb for the next generation of experiments. As we installed the new cell in December 2020, we discovered a white residue at the ends of the bellows [see Figure 3.3(b)]. The residue is likely to be rubidium hydroxide that forms when rubidium interacts with water, and whose description matches the observed appearance of the residue.

3.5 Atomic transitions for the double resonance measurements

In our experiments, we use a double-resonance configuration with the microwave field coupling the two hyperfine levels $|F = 1\rangle$ and $|F = 2\rangle$ of the ^{87}Rb ground state, and an optical probe that couples the $|F = 2\rangle$ state with one of the hyperfine states of $5P_{3/2}$ level. Because our probe was provided by the laser used in the cold-atom quantum memory experiment, in order to run both experiments simultaneously, we used a frequency in between the $|F = 2\rangle \rightarrow |F' = 2\rangle$ and $|F = 2\rangle \rightarrow |F' = 3\rangle$ transitions. Even though this frequency does not seem to be a perfect choice for optical pumping necessary to observe the double resonance, to our surprise and our labmates' envy, it produced more than a satisfactory double-resonance feature.

To explain why the seemingly off-resonant probe works, we need to consider Doppler broadening. As was discussed in Section 2.4.1, atoms are distributed over many velocity classes in thermal vapor. The Doppler shift compensates for the optical detuning from a particular transition for several velocity classes. In our case, there are three velocity classes for which the probe is on resonance with the corresponding transition, as is shown in Figure 3.4(a). Here, the probe optically pumps velocity classes v_1 and v_2 into $|F = 1\rangle$ state [see Figure 3.4(b)] in a process known as "velocity-selective optical pumping" [86–88], and atoms from these velocity classes contribute to the double-resonance signal. Because of the selection rules that forbid spontaneous emis-

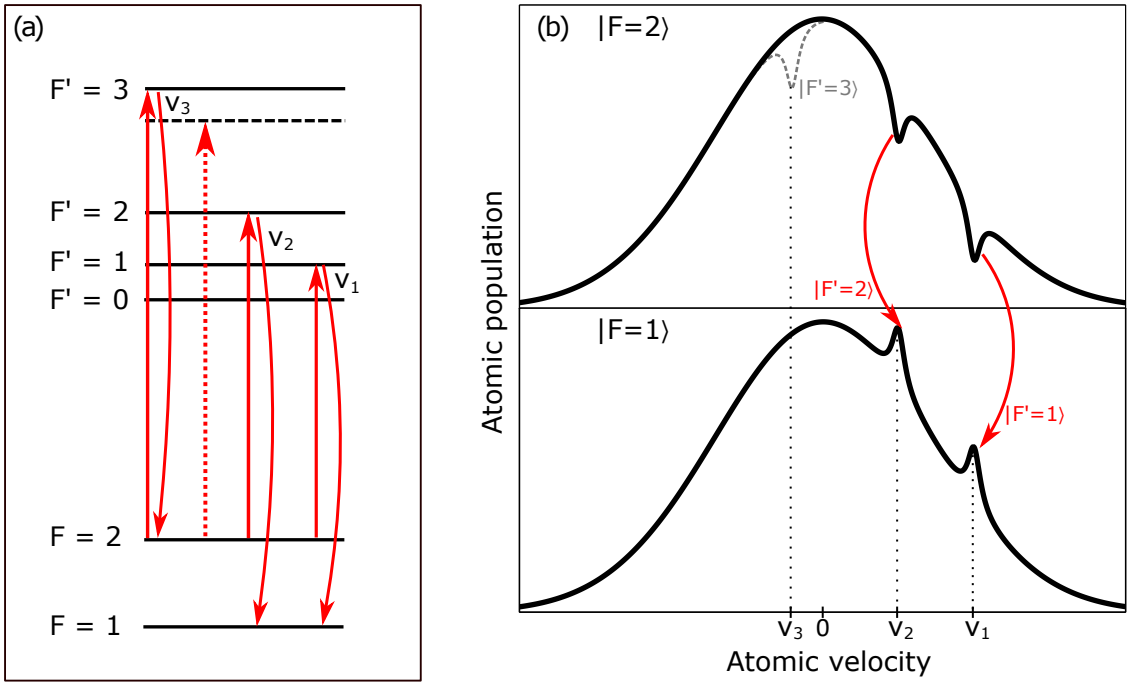

Figure 3.4: Illustration of velocity-selective optical pumping and velocity classes contributing to the double-resonance signal. (a) Schematics of the relevant levels. Dotted arrow indicates the probe frequency in the laboratory frame. Solid arrows show transitions resonant with the probe in three velocity classes. (b) Black solid curves show atomic population in states $|F = 2\rangle$ (top) and $|F = 1\rangle$ (bottom) as a function of the atomic velocity along the probe's wavevector (the horizontal axis is not to scale). The probe is on resonance with transitions $|F = 2\rangle \rightarrow |F' = 1\rangle$, $|F = 2\rangle \rightarrow |F' = 2\rangle$, and $|F = 2\rangle \rightarrow |F' = 3\rangle$ in velocity classes v_1, v_2, and v_3, respectively. Due to selection rules, only velocity classes v_1 and v_2 are optically pumped to $|F = 1\rangle$. Velocity class v_3 contributes to the absorption, but not to the double-resonance signal.

sion from $|F' = 3\rangle$ to $|F = 1\rangle$ (see Section 2.3.1), atoms in velocity class v_3 do not undergo optical pumping and continuously scatter the probe.

Because the Doppler shift at microwave frequencies is negligible, the microwave field interacts with all velocity-classes simultaneously. Combined with the velocity-selective optical pumping, this effectively makes the double-resonance imaging a Doppler-free technique.

3.6 Experimental characterization

This section presents our experimental investigation of various aspects of the microwave-optical double resonance that we carried out to learn more about this phenomenon and characterize the atom-cavity coupling. In all of these experiments, the probe laser operates in the continuous-wave regime. The transmission signal is obtained by digitally averaging several samples triggered by the signal that was used to modulate the microwave field.

3.6.1 Optical pumping and Rabi oscillations

As was discussed in Section 3.1, double-resonance imaging can be considered as a combination of optical pumping and coherent dynamics due to magnetic-dipole coupling by the microwave field. We can observe both effects by continuously monitoring the probe transmission as we switch the microwave interaction on and off. The latter is achieved by modulating the microwave frequency with a square-wave voltage signal. We set the modulation parameters so that the field is on resonance with the clock transition when the voltage is high and is far off-resonance when the voltage is low. In the second case, we effectively switch the interaction off.

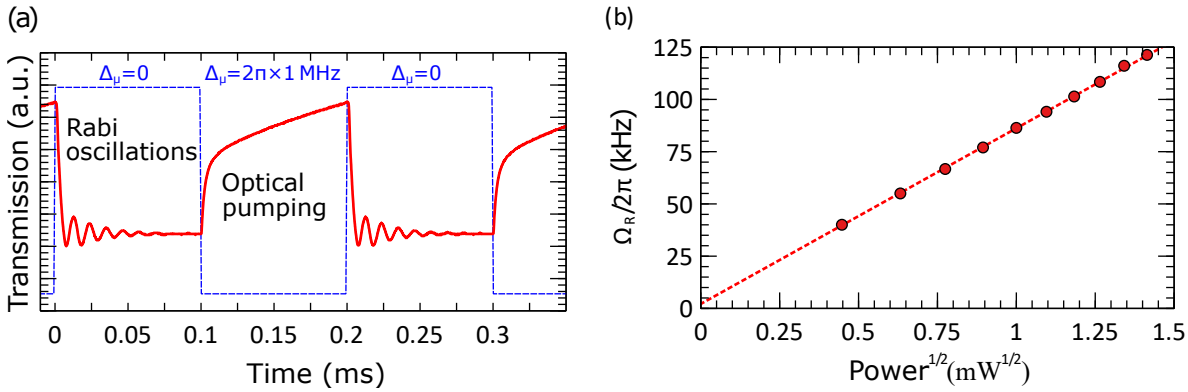

Figure 3.5: (a) Probe transmission (red solid) due to periodic square modulation (blue dashed) of the microwave field in the continuous-wave regime. (b) The Rabi frequency as a function of the microwave power. Red dashed line shows the linear fit. The Rabi frequency was determined via the fast Fourier transform.

The resulting optical signal is shown in Figure 3.5(a). When the microwave field is on resonance, a series of oscillations in the probe transmission are observed. Figure 3.5(b) shows a linear relationship between the oscillation frequency and the square-root value of the input microwave power, and thus the magnitude of the oscillating magnetic field, suggesting these are the Rabi oscillations. Due to relaxation in the vapor, the oscillations damp out to a steady-state level, where the optical pumping is balanced by the microwave driving. As the microwave interaction is switched off, the optical pumping transfers the atomic population to the dark state, increasing the probe transmission.

3.6.2 Double-resonance imaging for Zeeman spectroscopy and scalar magnetometry

The double resonance enables the detection of the microwave transitions between Zeeman sublevels of the hyperfine ground levels, and estimation of their transition frequencies. Below we demonstrate how the structure of the observed signal allows us to estimate the magnitude of the external static magnetic field. We use this information to adjust the microwave parameters and bias magnetic fields for optimal signal transduction.

Zeeman levels

Figure 3.6(a) shows the Zeeman structure of the ^{87}Rb ground state with all possible microwave M1 transitions. Each F-level has $2F + 1$ Zeeman sublevels, resulting in nine transitions that satisfy the M1 selection rules [see Section 2.3.1]. We detect these transitions with a conventional double-resonance technique [89] by performing a symmetrical linear sweep of the microwave frequency through the hyperfine splitting value of 6.834 682 612 910 GHz. The linear sweep is achieved with a saw-tooth modulation. Figure 3.6(b) shows the results for two cases: a typical ambient magnetic field and a bias-canceled field. We assume that for a sufficiently slow frequency sweep, the atomic population quasi-statically follows the frequency-dependent steady

state. Each microwave transition results in a Lorentzian-shaped dip in the probe transmission centered at the transition frequency. The validity of this assumption will be discussed in Section 3.6.4.

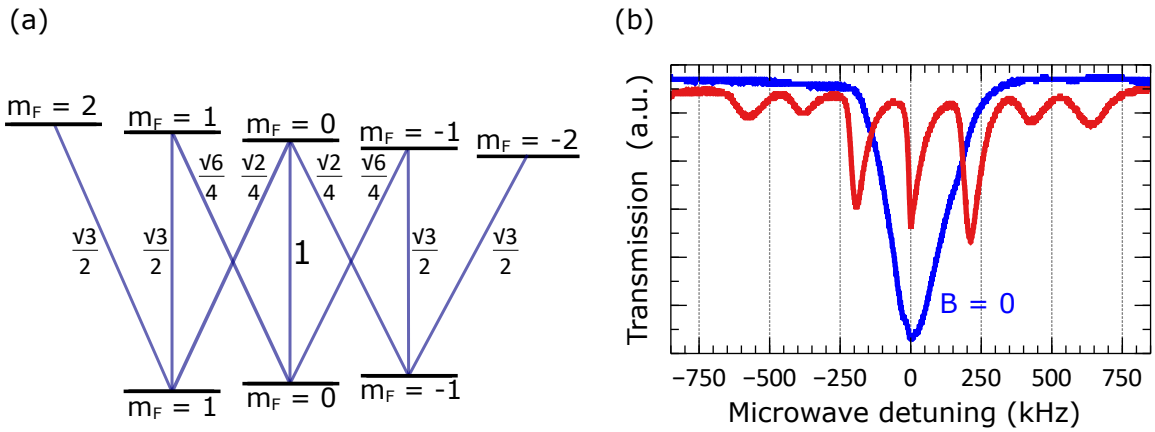

Figure 3.6: (a) Zeeman level structure of ^{87}Rb hyperfine ground state (see Figure 2.3). Purple lines indicate possible microwave M1 transitions. Transitions indicated by crossing lines have the same frequency and contribute to the same double-resonance dip. Numerical value next to a line shows the transition strength relative to the clock transition $|F = 1, m_F = 0\rangle \rightarrow |F' = 2, m'_F = 0\rangle$. (b) Contentious-wave optical transmission during a linear microwave frequency sweep. The x-axis shows the detuning from the frequency of 6.834 682 610 904 GHz. When the ambient magnetic field is canceled, all transitions are degenerate and contribute to a single peak.

A constant magnetic field splits Zeeman sublevels [see Section 2.2], introducing a difference in the transitions' frequencies, which results in several observed transmission resonances, seen as "dips". The central resonance corresponds to the $|F = 1, m_F = 0\rangle \rightarrow |F' = 2, m'_F = 0\rangle$ transition. This transition is insensitive to the linear Zeeman shift and has the largest matrix element [see Section 3.6.3], making it the transition of choice for the microwave atomic clocks, and it is therefore referred to as the "clock transition." Each pair of crossing lines from Figure 3.6(a) corresponds to transitions experiencing the same frequency shifts with respect to the clock transition, which contribute to the same resonances. This reduces the number of observed resonances from nine to seven.

Scalar magnetometry

The distance between double-resonance dips during the microwave frequency scan depends on the magnitude of the applied static magnetic field, making this technique suitable for scalar magnetometry - a procedure for finding the magnitude of the magnetic field. In a weak static magnetic field $\mathbf{B}$, the double-resonance dips are separated by the Larmor frequency

$$\omega_{\mathrm{L}} = \frac{\mu_{\mathrm{B}} B}{2\hbar}, \tag{3.2}$$

which allows us to find the magnetic field magnitude B from the frequency separation and fundamental constants. If there is no external magnetic field, both hyperfine ground states are degenerate, and a single transmission resonance dip is observed. This technique can be employed to assist in canceling out stray magnetic fields or singling out a particular microwave transition in magnetic-field sensitive experiments [90] where, due to physical constraints, the magnetic field can not be measured directly with a magnetometer.

3.6.3 Relative depth of double-resonance dips

As can be seen in Figure 3.6(b), the depth of the double-resonance transmission signal varies from transition to transition. This implies that different transitions couple to the microwave field with different strengths. Below we discuss the three main factors contributing to these differences: the transition matrix element, cavity resonance and bandwidth, and the orientation of the external field with respect to the cavity axis.

Matrix element

As was discussed in Section 2.3.2, the coupling between two atomic levels due to the interaction with an external electromagnetic field is proportional to the matrix element of the quantum operator describing this interaction, calculated between the two coupled quantum states. The magnetic-dipole interaction term for a microwave

field with vector $\mathbf{b}$ is characterized by the operator

$$\hat{V}_{\mathrm{m}} = -\hat{\boldsymbol{\mu}} \cdot \mathbf{b} = \left(|g_s| \frac{\hat{\mathbf{s}}}{\hbar} + |g_l| \frac{\hat{\mathbf{l}}}{\hbar} - g_{\mathrm{I}} \frac{m_{\mathrm{e}}}{m_{\mathrm{p}}} \frac{\hat{\mathbf{I}}}{\hbar} \right) \mu_{\mathrm{B}} \mathbf{b}, \tag{3.3}$$

where m_{p} is mass of a proton, $g_s \approx -2$ and $g_l \approx -1$ are electron's spin and orbital g-factors respectively, g_{I} is the nuclear g-factor, and the angular momentum operators are given in units of $\hbar$. We use absolute values of the electron's g-factor to avoid confusion between different conventions, keeping in mind that the electron's magnetic moments are always antiparallel to the corresponding angular momenta. Because $m_{\mathrm{e}}/m_{\mathrm{p}} \ll 1$, we ignore the last term in (3.3).

If we consider the case of ground states of alkali metals only, in which case $l = 0$, the coupling operator becomes

$$\hat{V}_{\mathrm{m}} = \frac{2\mu_{\mathrm{B}}}{\hbar} \hat{\mathbf{s}} \cdot \mathbf{b} = \frac{2\mu_{\mathrm{B}}}{\hbar} \left(b_\tau \hat{s}_{\mathrm{z}} + b_\perp \hat{s}_{\mathrm{x}} \right), \tag{3.4}$$

where $\mathbf{b}_\tau$ is the vector component tangential to the quantization axis (usually set by a static magnetic field causing splitting of Zeeman levels), and $\mathbf{b}_\perp$ is the component perpendicular to the quantization axis. The tangential component $\mathbf{b}_\tau$ drives π-transitions, contributing to three of the seven resonance dips in Figure 3.6(b), while the transverse component $\mathbf{b}_\perp$ drives $\sigma^{\pm}$-transitions contributing to the remaining four resonance dips.

The matrix element for the π-transitions between the two alkali ground-state levels is given by [91]

$$M_\pi = \left| \left\langle F+1, m_{\mathrm{F}} \left| \frac{\hat{s}_{\mathrm{z}}}{\hbar} \right| F, m_{\mathrm{F}} \right\rangle \right| = (I+1/2) \sqrt{(I+1/2)^2 - m_{\mathrm{F}}^2} = \sqrt{1 - g_{\mathrm{F}}^2 m_{\mathrm{F}}^2}, \tag{3.5}$$

where g_{F} is the Landé g-factor defined in Eq. 2.5. For the clock transition $m_F = 0$, and the matrix element does not depend on the nuclear spin I, and is the same for all alkali atoms.

For the $\sigma^{\pm}$-transitions between the two alkali ground states, the matrix element is

given by [91]

$$M_\sigma = \left| \left\langle F+1, m_\mathrm{F} \left| \frac{\hat{s}_\mathrm{x}}{\hbar} \right| F, m_\mathrm{F} \pm 1 \right\rangle \right| = \frac{1}{2I+1}\sqrt{(I \mp m_\mathrm{F})^2 - \frac{1}{4}}. \tag{3.6}$$

The matrix elements for each microwave transition in our case are indicated in Figure 3.6(a). From equations 3.5 and 3.6 it can be shown that the clock transition has the largest matrix element. Thus, all other parameters being equal, it gives the largest double-resonance absorption.

Magnetic field orientation

As was discussed above, we have three types of transitions driven by different microwave field polarization components, defined with respect to the quantization axis [see Appendix B for more details on polarization]. In the lab frame, the microwave field is linearly polarized along the cavity axis, so its polarization with respect to the static magnetic field $\mathbf{B}$ depends on the angle θ between $\mathbf{B}$ and the cavity axis [See Figure 3.7(a)]. As a result, the Rabi frequency for the π transitions is given by

$$\Omega_\pi = \frac{1}{2} M_\pi(m_\mathrm{F}) \mu_\mathrm{B} b_\tau = \frac{1}{2} M_\pi(m_\mathrm{F}) \mu_\mathrm{B} b |\cos\theta|, \tag{3.7}$$

while for the $\sigma^\pm$-transitions, the Rabi frequency is

$$\Omega_\sigma = \frac{1}{2} M_\sigma(m_\mathrm{F}, m_{\mathrm{F}'}) \mu_\mathrm{B} b_\perp = \frac{1}{2} M_\sigma(m_\mathrm{F}, m_{\mathrm{F}'}) \mu_\mathrm{B} b |\sin\theta|, \tag{3.8}$$

where M_π and M_σ are the matrix elements from Eq. 3.5 and Eq.3.6, respectively, and the prefactors come from the rotating-wave approximation.

Figure 3.7(b) shows the double-resonance scan in two limiting cases of the magnetic field orientation. Here, we first tune the bias magnetic field to cancel out the ambient field and then apply excessive field in a direction either parallel or perpendicular to the cavity axis. In the parallel case, $\theta = 0$, the microwave field has only a tangential component: $b = b_\tau$. In this case, we observe only three peaks corresponding to the π-transitions and separated by $2\omega_\mathrm{L}$. In the perpendicular case, the microwave field has only a transverse component: $b = b_\perp$. In this case, we expect to observe

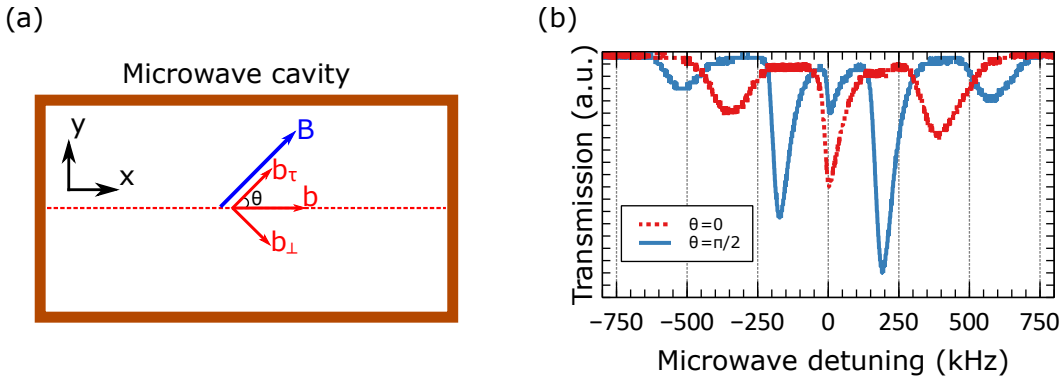

Figure 3.7: (a) Orientation of the microwave field vector **b** and a static magnetic field **B**. The microwave field oscillates along the cavity axis indicated by the dashed line. With respect to the quantization axis, vector **b** can be decomposed into tangential $b_\tau = b\cos\theta$ and transverse $b_\perp = b\sin\theta$ components driving the π- and $\sigma^\pm$-transitions, respectively. (b) Double-resonance spectrum for two orientations of the bias magnetic field, plotted as a function of the microwave detuning from the clock transition. Blue solid curve corresponds to the case when the bias field is perpendicular to the cavity axis. Red dashed represents parallel orientation.

only four peaks corresponding to $\sigma^\pm$-transitions, while in fact, we can see the central peak corresponding to the clock transition. A possible explanation is the bias field's inhomogeneity that does not completely cancel the ambient magnetic field along the cavity axis. Because the clock transition has the largest matrix element, and its frequency is the closest to the cavity resonance, it results in a signal that is sufficiently strong to be noticeable.

Cavity resonance and linewidth

We use a high-Q cavity to amplify the microwave field and increase the coupling strength. A downside of this approach is the small cavity linewidth, which is an inevitable consequence of the high Q-factor. As a result, only microwave fields at frequencies close to the cavity resonance are enhanced, while the fields at other frequencies are suppressed. In terms of the double-resonance spectrum, it means that the depth of a transmission dip depends on how close the corresponding transition is

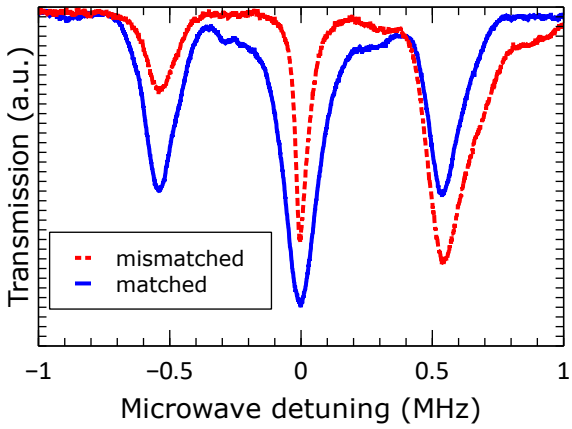

Figure 3.8: Double-resonance spectrum as a function of the microwave detuning from the clock transition for two values of the cavity resonance frequency. When the cavity resonance frequency matches the frequency of the clock transition (blue solid curve), the observed spectrum is symmetric. In the case when the cavity resonance frequency is higher than the clock transition frequency (red dashed curve), the spectrum is tilted towards higher-frequency transitions.

to the cavity resonance.

In our cavity, we can mechanically adjust the resonance frequency by moving one of the endcaps. This might be useful if we want to selectively enhance a particular transition, which is usually the clock transition. Figure 3.8 shows that the mismatch between the cavity resonance and the clock transition frequency results in an asymmetric shape of the double-resonance scan (red). This measurement provides a quick way to detect a shift of the cavity resonance from the clock transition.

3.6.4 Signal shape and frequency-sweeping rate

When we were discussing the shape of the double-resonance signal above, we assumed the atomic population stays in the steady-state as the microwave frequency is varied. In this case, each microwave transition provides a Lorentzian dip in transmission, which is symmetric with respect to the transition frequency. When we first obtained the double-resonance spectrum, the observed dips did not have the expected symmetry, which was a puzzle at that time. A closer investigation showed that the

asymmetry does not depend on the actual microwave frequency or the direction of the frequency sweep [see Figure 3.9(a)], which was a hint that the issue was an artifact of our measuring approach.

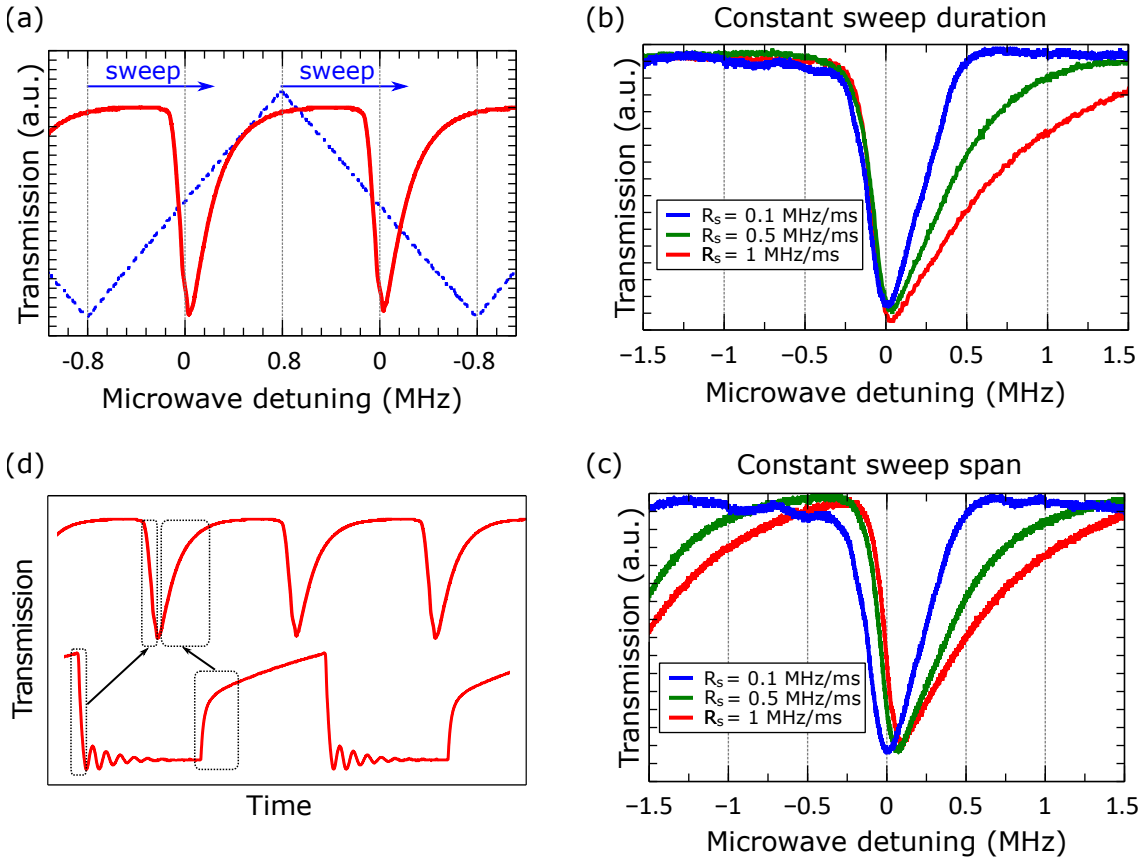

Figure 3.9: (a) Double-resonance signal during the back-and-forth frequency sweep. The dashed blue line indicates the triangular modulating signal. The modulation repetition rate is 120 Hz. (b) Double-resonance signal for a constant frequency sweep duration of 20 ms for three different values of the frequency sweep rate R_s. The rate is varied by adjusting the frequency span. (c) Double-resonance signal for a constant frequency span of 2 MHz for three different values of the frequency sweep rate R_s. The rate is varied by adjusting the sweep duration. (d) Hypothetical correspondence between the signals shown in (a) and Figure 3.5(a).

Below we demonstrate that the asymmetry arises at a higher microwave frequency sweeping rate, which suggests that in this case, the atomic population does not have sufficient time to keep up with the changing steady-state. In our setup, we control

the microwave frequency with an external sawtooth voltage with a constant repetition rate. This gives us two different ways to control the sweeping rate. For the measurements shown in Figure 3.9(b), we change the sweep duration by varying the control signal repetition rate, while keeping the frequency span constant. For the results shown in Figure 3.9(c), we vary the frequency span at a constant sweep duration. In both cases, a symmetric signal is observed at a lower sweeping rate.

In order to explain the asymmetric shape, we would like to highlight the resemblance between the two parts of the double-resonance dip in the high-rate case with the double-resonance signal at the falling and rising edges in the case of square-pulse modulation shown in Figure 3.9(d). This suggests that as the frequency is swept towards the resonance of the corresponding transition, the dynamics are dominated by the microwave drive, while after the frequency crossed the resonance, the main contribution is from the optical pumping. A slow sweeping rate allows the atomic population to quasi-statically follow the steady-state where these two processes are balanced.

To see how close the double-resonance signal is to an actual steady-state transmission during a linear sweep, we measure the latter directly. As it turns out, measuring the actual steady-state transmission in our setup is complicated. All our double-resonance measurements are done in AC coupling regime of the oscilloscope, where any constant offset of the voltage signal is filtered out. This is necessary because the double-resonance signal is only a very small correction to a constant transmission level (see Eq. 3.1), and our oscilloscope can not resolve the signal in DC coupling regime.

To overcome this issue and estimate the shape of the steady-state transmission in the AC regime, we use square-pulse frequency modulation [see Figure 3.10(a)]. As the reference point, we use the transmission signal on resonance. For the case of a positive microwave detuning, we set up the modulation parameters so that the low signal of the square-pulse train corresponds to the resonance frequency, while the high signal

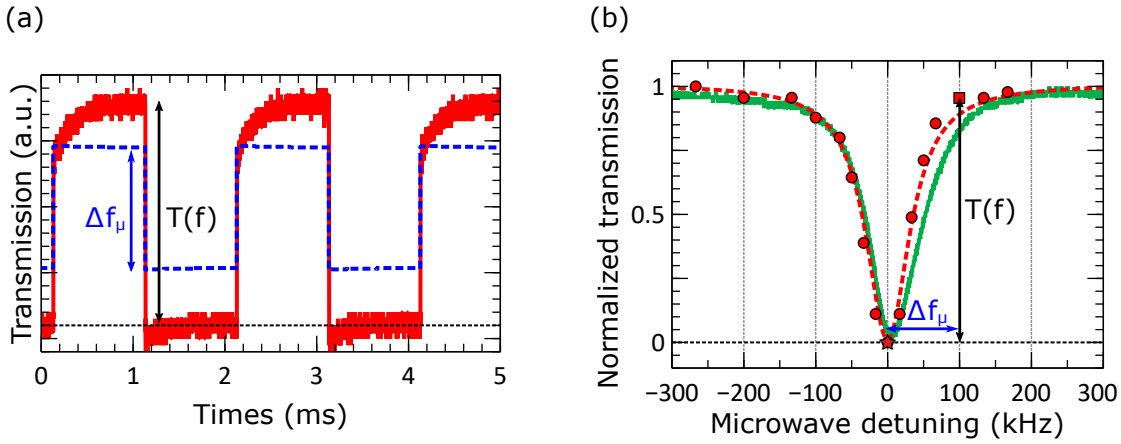

Figure 3.10: (a) Example measurement for the data-point corresponding to transmission (red solid) at the frequency detuning $\Delta f_\mu = 100$ kHz. The blue dashed curve shows the frequency-modulation signal with the low level corresponding to the resonance frequency. The modulation rate is chosen to allow the transmission to reach the steady state. The blue and black arrows correspond to data point coordinate in (b). (b) Comparison between the double-resonance transmission during a linear sweep (green solid) and the steady-state transmission measured "by hand" (red dots). Red dashed curve corresponds to Lorentzian fit through the steady-state values. Both signals are normalized so that zero and one correspond to the lowest and highest transmission values, respectively. The star and horizontal dotted line correspond to the reference transmission for the steady-state measurements.

shifts the frequency proportionally to its value. We adjust the pulse duration to allow the transmission signal to level off. We use the difference between the maximal and minimal values of the transmission signal as an estimate for the steady-state value at the corresponding microwave detuning with respect to the resonance value. We do the same procedure for the case of negative detuning by reversing the sign of the square pulses. Figure 3.11(b) shows the normalized steady-state transmission estimated in this way, which is in a good agreement with the corresponding continuous-wave signal. The square indicates the data point corresponding to the signal from (a).

3.6.5 AC magnetometry with a phase-modulated field

Even though we can directly estimate the strength of the microwave coupling by measuring the frequency of the Rabi oscillations, this method's precision depends on the

number of the observed Rabi cycles, which is limited by relaxation processes. Because of the straightforward relationship between the Rabi frequency and the magnitude of the oscillating magnetic field, the process of finding the Rabi frequency is commonly referred to as the AC magnetometry. Below we discuss how we can extend the precision of AC magnetometry by using a phase-modulated microwave field.

First, let us consider a phase-modulated magnetic field

$$b(t) = b\cos[\omega t + \theta(t)] = b\cos(\omega t + m\sin\omega_{\mathrm{m}} t) \tag{3.9}$$

where ω is the carrier frequency, ω_{m} is the modulation frequency, and m is the modulation depth. Here, the quadrature phase $\theta(t)$, is what we refer to as "the phase". The time-independent rotating-wave Hamiltonian $\hat{H}'$ in Eq. 2.13, now needs to be replaced with a time-dependent periodic Hamiltonian

$$\hat{\tilde{H}}(t) = \frac{\hbar}{2}\left(\Omega_{\mathrm{R}}\hat{\sigma}_x - [\delta + \dot{\theta}(t)]\hat{\sigma}_z\right) = \hat{H}' - \frac{\hbar}{2}\hat{\sigma}_z m\omega_{\mathrm{m}}\cos\omega_{\mathrm{m}} t. \tag{3.10}$$

It was mathematically proved [92] that an open quantum system driven by a periodic Hamiltonian with period T has a dynamic steady-state solution $\rho_{\mathrm{s}}(t)$, such that $\rho_{\mathrm{s}}(t+T) = \rho_{\mathrm{s}}(t)$, where the "dynamic steady state" refers to the time-dependent quantum state at times much larger than the relaxation time. Practically, for us it means that applying a phase-modulated microwave would result in a periodic steady state with an arbitrary large number of cycles instead of a few Rabi oscillations decaying to a constant level.

Figures 3.11(a) and 3.11(b) show the double-resonance optical transmission for the case of a phase-modulated microwave field. As is expected, it is periodic, and its spectrum consists of spectral components at multiples of ω_{m} [see Figure 3.11(c)]. The spectrum has two curious features. First, the relationship between the amplitudes of the odd and even harmonics depends on the carrier detuning δ. Surprisingly, when $\delta = 0$, the spectrum contains only even harmonics [see Figure 3.11(d)]. Second, the amplitudes of the spectral components show a resonant behavior when their

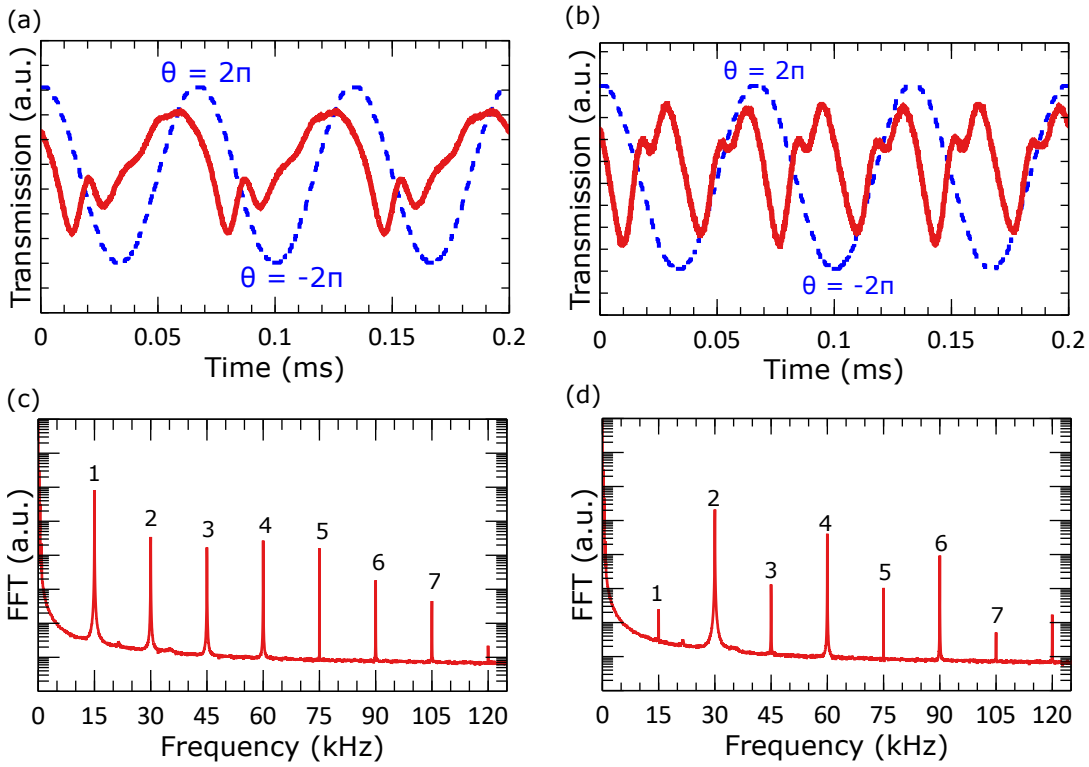

Figure 3.11: (a) Double-resonance signal (red solid curve) of the dynamic steady state for microwave phase modulation $\theta(t) = m \sin \omega_{\rm m} t$ (blue dashed curve), with $m = 2\pi$ and $\omega_{\rm m}/2\pi = 15$ kHz, and the carrier detuning $\delta = 10$ kHz. (b) Same as in (a), except $\delta = 0$. (c-d) Fast Fourier transform of the signal in (a-b). The integer numbers next to the peaks indicate harmonics of $\omega_{\rm m}$ the peaks correspond to. Plots are on a semi-logarithmic scale. For $\delta = 0$, the odd harmonics are suppressed.

frequencies are close to the Rabi frequency [93, 94]. For a two-level system, the analytical form of the Rabi resonance lines can be obtained in the small-signal approximation [41], where $m < \sqrt{2\Gamma_1/\omega_{\rm m}}$ and $\omega_{\rm m} \gg \Gamma_2$. Under these conditions, the dynamic steady-state population contains only two harmonics, with the excited state population given by [41]

$$\rho_{22,\rm s}(t) = P_1 \cos(\omega_{\rm m} t + \phi_1) + P_2 \sin(2\omega_{\rm m} t + \phi_2), \tag{3.11}$$

with amplitudes

$$P_1 = \frac{\frac{m}{2}\omega_{\mathrm{m}}\Omega_{\mathrm{R}}^2\delta}{\left[\Gamma_2^2 + \delta^2 + \frac{\Gamma_2}{\Gamma_1}\Omega_{\mathrm{R}}^2\right]\sqrt{\left(\omega_{\mathrm{m}}^2 - \Omega_{\mathrm{R}}^2\right)^2 + \Gamma_1^2\omega_{\mathrm{m}}^2}}, \tag{3.12}$$

$$P_2 = \frac{\left(\frac{m}{2}\right)^2\omega_{\mathrm{m}}\Omega_{\mathrm{R}}^2\Gamma_2}{\left[\Gamma_2^2 + \delta^2 + \frac{\Gamma_2}{\Gamma_1}\Omega_{\mathrm{R}}^2\right]\sqrt{\left(\omega_{\mathrm{m}}^2 - 4\Omega_{\mathrm{R}}^2\right)^2 + 4\Gamma_1^2\omega_{\mathrm{m}}^2}}, \tag{3.13}$$

and quadrature phases

$$\phi_1 = -\tan^{-1}\left[\frac{\Omega_{\mathrm{R}}^2 - \omega_m^2}{\Gamma_1\omega_m}\right], \quad \phi_2 = \tan^{-1}\left[\frac{\Omega_{\mathrm{R}}^2 - 4\omega_m^2}{2\Gamma_1\omega_m}\right]. \tag{3.14}$$

In agreement with Figure 3.11(d), Eq. 3.12 predicts the disappearance of the first harmonics when $\delta = 0$. In addition, according to Eq 3.12 and Eq 3.13, amplitudes P_1 and P_2 experience enhancement, known as the "Rabi resonances," when the frequency of the corresponding harmonic is resonant with the Rabi frequency, $\omega_{\mathrm{m}} = \Omega_{\mathrm{R}}$ and $2\omega_{\mathrm{m}} = \Omega_{\mathrm{R}}$, respectively. The Rabi resonances allow finding the Rabi frequency by scanning ω_{m}, which is widely used for microwave AC magnetometry inside cavities [46, 95], waveguides [42, 43, 96], and in free space [45, 46, 48, 49, 97].

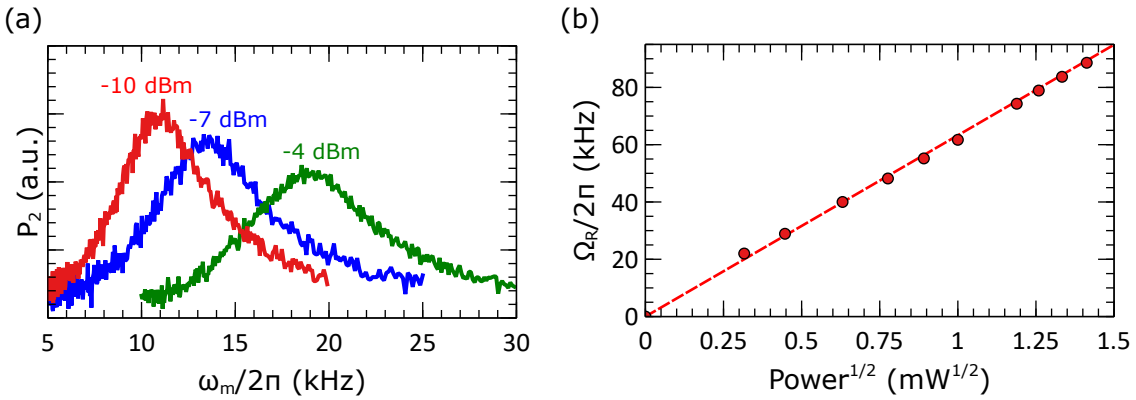

Figure 3.12: (a) Amplitude of the second harmonics as a function of the modulation frequency of phase modulation for three values of the microwave power. Measured on the clock transition with $m = \pi$. (b) Extracted Rabi frequency as a function of the square-root value of the microwave power. Linear fit (red dashed) gives a slope of 58.6 kHz/mW$^{1/2}$.

Figure 3.12(a) shows the second-harmonics Rabi resonance in our system obtained with a lock-in amplifier for several microwave power values. Here, the lock-in amplifier

serves as a source of the control signal for the phase modulation at ω_{m} and as a spectral analyzer of the double-resonance transmission. For the latter, the lock-in amplifier integrates the photodetector voltage with an internal sinusoidal reference at twice the modulation frequency and applies a DC filter to the result. The outcome is a DC voltage proportional to the amplitude of the analyzed signal's spectral component at the reference frequency $2\omega_{\mathrm{m}}$. In our case, the lock-in amplifier automatically adjusts the integration time during the analysis as it scans ω_{m}. Figure 3.12(b) shows the expected linear dependence between the square-root value of the microwave power and Ω_{R} extracted from the location of the Rabi resonance peak.

Meditations on the nature of the spectrum

For a long time, we could not find a comprehensive theory that would explain the spectra observed in Figure 3.11(a-b) neither in literature nor in discussions with our colleagues working on similar experiments. Especially curious is the fact that the dynamic steady-state contains only even harmonics when the carrier is on resonance. Even though Eq. 3.12 describes this behavior for the first harmonics, it is a rather mathematical result that does not provide an understanding of the essence of this phenomenon. Here we propose a qualitative explanation of the observed spectra, which is based on the insights we gained from the experiments on microwave-to-optical transduction.

We begin by noticing that according to Eq. 5.1, the phase modulation $\theta(t)$ effectively acts as a perturbation to the carrier detuning, which we take into account by introducing the effective detuning $\tilde{\delta}(t) = \delta + \dot{\theta}(t)$. Next, we assume that the modulation period is much larger than the response time of the two-level system, which allows the system's quantum state to quasistatically follows the instantaneous steady state, which we define as a stationary solution of Eq. 2.17 with the pseudo-field $\mathbf{\Omega}(t)$ treated as a time-varying parameter. The instantaneous steady-state population $P(\delta, t)$ of

the excited level is obtained by substituting δ with $\tilde{\delta}(t)$ in Eq. 2.20, yielding

$$P(\delta,t) = \rho_{22,\mathrm{s}}[\delta + \dot{\theta}(t)] = \frac{1}{2}\frac{\Omega_{\mathrm{R}}^2 \frac{\Gamma_2}{\Gamma_1}}{\Gamma_2^2 + [\delta + \dot{\theta}(t)]^2 + \Omega_{\mathrm{R}}^2 \frac{\Gamma_2}{\Gamma_1}}. \tag{3.15}$$

Expanding Eq. 3.15 in a series of $\dot{\theta}(t) = m\omega_{\mathrm{m}} \cos \omega_{\mathrm{m}} t$ results in

$$P(\delta,t) = P(\delta) + \sum_{n=1}^{+\infty} \frac{P^{(n)}(\delta)}{n!} (m\omega_{\mathrm{m}} \cos \omega_{\mathrm{m}} t)^n, \tag{3.16}$$

whose spectrum consists of integer harmonics of ω_{m}, explaining the experimental spectrum in Figure 3.11(c). For example, the component corresponding to $n = 4$ is given by

$$P_4(\delta,t) = \frac{P^{(4)}(\delta)}{4!} m^4 \omega_{\mathrm{m}}^4 \cos^4(\omega_{\mathrm{m}} t) = \frac{P^{(4)}(\delta)}{4!} m^4 \omega_{\mathrm{m}}^4 \left(\frac{3}{8} + \frac{1}{2}\cos 2\omega_{\mathrm{m}} t + \frac{1}{8}\cos 4\omega_{\mathrm{m}} t \right),$$

whose spectrum consists of the second and fourth harmonics. Since $P(\delta)$ is an even function, its odd-order derivatives $P^{(2k+1)}(\delta)$ are odd functions, and thus

$$P^{(2k+1)}(0) = 0. \tag{3.17}$$

As a result, when $\delta = 0$, the right-hand side of Eq. 3.16 has only even powers of $\cos \omega_{\mathrm{m}} t$, whose spectra include even harmonics only, explaining the absence of the odd harmonics in Figure 3.11(d).

We would like to stress out that our results obtained in the quasi-static approximation qualitatively agree with the experimental spectra but do not capture the resonance behavior of the spectral components, which can be considered as a result of the interplay between the dynamics of the instantaneous steady state and the two-level system response [94].

Chapter 4

Microwave-to-optical transduction of an audio signal

This chapter presents our results on the transduction of an audio signal from a microwave to an optical carrier, which was published in Ref. [62]. For the transduction, we developed a novel method based on the microwave-to-optical double resonance, with the audio signal encoded as either frequency or amplitude modulation. This approach makes the technique readily available for radio-over-fiber communications with a simpler and more robust experimental setup compared to previous atom-based audio transduction techniques.

This chapter's content follows that of the publication rather closely, with more details and discussions provided here. We begin by briefly introducing the field of radio-over-fiber communications in Section 4.1. Next, we describe the principle of our transduction technique in Section 4.2 and the experimental setup in Section 4.3. After that, we present the measurements used to characterize our method in Section 4.4 and the final results of the audio signal transduction in Section 4.5. Finally, we discuss our method's practical advantage and feasibility compared to other techniques in Section 4.6, and provide a brief overview and possible future directions in Section 4.7.

4.1 Introduction and motivation

This experiment was motivated by the field of radio-over-fiber (RoF) communications [98], and atomic radio [51] in particular. The primary motivation for the radio-over-fiber communication technologies is a growing demand in wireless communication operating in GHz frequency range with a trend toward microwaves (in some literature referred to as radio waves) with frequencies of $20-30$ GHz and higher [99, 100]. The challenge encountered by this trend is that electromagnetic waves at these frequencies do not penetrate efficiently through walls and experience significant attenuation when propagating in cables, which limits their suitability in home-area networks and urban areas. The RoF approach addresses this problem by mapping the radio signal to an optical carrier, which can access hard-to-reach areas via optical fiber. A device performing the conversion is known as a transducer or an optical antenna.

Room-temperature alkali vapors are promising candidates for microwave-to-optical transducers in RoF applications. In these systems, there have been recently demonstrated successful transduction of amplitude (AM) and frequency (FM) modulated analog signals [51, 53, 57], AM and FM digitized signals [54, 56, 58, 101, 102], and even music recording [61, 103]. All these experiments use microwave electric-dipole transitions between highly excited atomic states, known as the Rydberg states. Atoms in Rydberg states have large AC electric polarizability and couple strongly to the electric-field component of the microwave field. This coupling results in the Autler-Townes splitting of the coupled levels, which depends on the magnitude and frequency detuning of the microwave field. Modulating these microwave parameters leads to modulation of the splitting, which is mapped onto the intensity of a probe laser beam via electromagnetically-induced transparency created by a second higher-frequency laser addressing one of the involved Rydberg states. Below we propose an alternative signal transduction method based on magnetic-dipole coupling, which increases the repertoire of atom-based transducers for RoF applications.

4.2 Principle

In our approach, microwave-to-optical transduction is based on the double-resonance scheme discussed in Chapter 3, where a room-temperature rubidium vapor simultaneously interacts with resonant or near-resonant optical electric and microwave magnetic fields $\mathbf{E}(t)$ and $\mathbf{b}(t)$, respectively. To explain the transduction principle, we will use the same three-level model, as in Figure 3.1 . The microwave field couples $|g_1\rangle$ and $|g_2\rangle$ states from the hyperfine ground state of ^{87}Rb, which can be either the degenerate levels $|F = 1\rangle$ and $|F = 2\rangle$ or isolated Zeeman sublevels, e.g, $|F = 1, m_F = 0\rangle$ and $|F = 2, m_F = 0\rangle$. Qualitatively, the transduction performs equally well in both cases, but the degenerate case gives a better signal-to-noise ratio since all transitions contribute to a single double-resonance dip. The optical field couples $|g_2\rangle$ to an excited state $|e\rangle$ and serves both as the optical pump and the probe. The experimental details and parameters used in this chapter will be given in the following section.

As was discussed in Section 3.1, if the optical and microwave parameters are kept constant, the atomic population reaches a steady state that determines how much light is transmitted. In a dilute vapor, the transmitted optical intensity is proportional to the steady-state population and depends on the microwave parameters. As we have also seen in Chapter 3, time variation in the microwave parameters leads to dynamic change in the transmitted optical signal. Provided that the variation is sufficiently slow, the signal follows the analytical shape of the steady-state population. In addition, in the case of the variation $\delta X(t)$ of a microwave parameter X is sufficiently small, the optical transmission linearly follows the variation:

$$T[X + \delta X(t)] \approx T(X) + \frac{\partial T}{\partial X}\delta X(t). \tag{4.1}$$

This linear relationship allows us to transduce a baseband signal by encoding it in the microwave modulation $\delta X(t)$. The idea here is similar to the principle of frequency-modulation spectroscopy [104], except in our case, the derivative is obtained through an auxiliary field, rather than modulating the probe itself.

The double-resonance scheme allows signal encoding as either a frequency or an amplitude modulation. This fact is evident from the Hamiltonian

$$\hat{H} = \hat{H}_0 - \hat{\mathbf{d}} \cdot \mathbf{E}(t) - \hat{\boldsymbol{\mu}} \cdot \mathbf{b}(t), \tag{4.2}$$

where $\hat{H}_0$ is the atomic Hamiltonian, and $\hat{\mathbf{d}}$ and $\hat{\boldsymbol{\mu}}$ are the electric and magnetic dipole operators, respectively. For the harmonic fields $\mathbf{E}(t) = \mathbf{E}_0 \cos(\omega_{\text{opt}} t + \phi_{\text{opt}})$ and $\mathbf{b}(t) = \mathbf{b}_0 \cos(\omega_\mu t + \phi_\mu)$, the three-level rotating-wave Hamiltonian takes the following form:

$$\hat{H} = \frac{\hbar}{2} \begin{pmatrix} 2\Delta_{\text{opt}} & \Omega_{\text{opt}} e^{-i\phi_{\text{opt}}} & 0 \\ \Omega_{\text{opt}} e^{i\phi_{\text{opt}}} & 0 & \Omega_{\text{R}} e^{-i\phi_\mu} \\ 0 & \Omega_{\text{R}} e^{i\phi_\mu} & 2\Delta_\mu \end{pmatrix}, \tag{4.3}$$

where Δ_{opt} and Δ_μ are the optical and microwave detunings respectively, and Ω_{opt} and Ω_{R} are the optical and microwave Rabi frequencies, respectively. The Hamiltonian is given in a rotating basis obtained from $\{|e\rangle, |g_2\rangle, |g_1\rangle\}^{\text{T}}$ by applying the following transform:

$$\hat{U}(t) = \begin{pmatrix} e^{i\omega_{\text{opt}} t} & 0 & 0 \\ 0 & 1 & 0 \\ 0 & 0 & e^{i\omega_\mu t} \end{pmatrix}. \tag{4.4}$$

In the above Hamiltonian, modulation of the microwave amplitude and frequency affects Ω_{R} and Δ_μ, respectively. As was discussed in Section 3.6.5, the phase-modulation's effect on the optical transmission is proportional to the modulation signal's derivative, which makes this type of modulation too complicated for signal transduction.

Figure 4.1 illustrates the principle of the AM and FM transduction in terms of the double-resonance profile. In the AM case, the modulating signal $V(t)$ changes the microwave magnetic field amplitude, such that

$$b_{\text{AM}}(t) = b_0[1 + m_{\text{AM}} V(t)] \cos(\omega_\mu t + \phi_\mu), \tag{4.5}$$

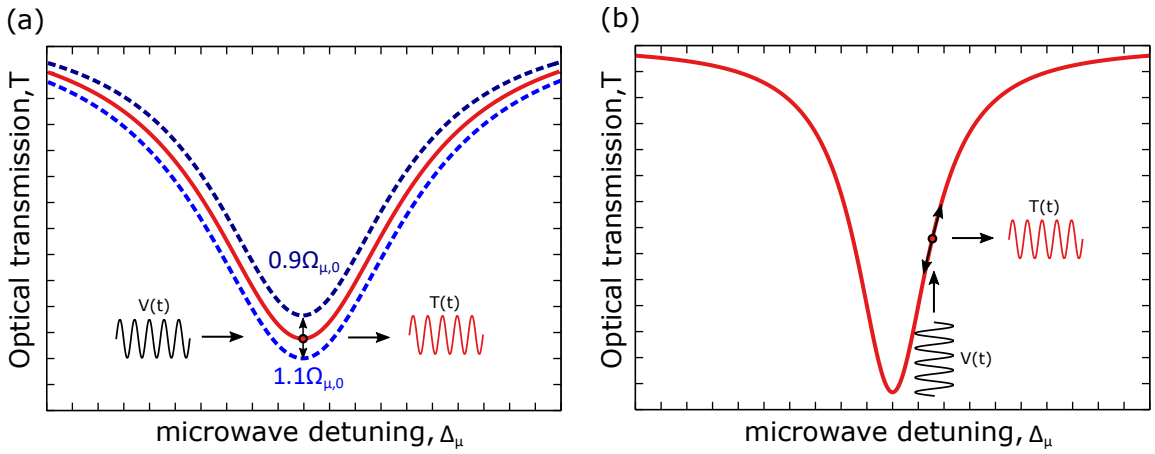

Figure 4.1: Illustration of the AM and FM transduction principles in terms of the double-resonance profile. (a) In the AM case, the modulating signal $V(t)$ modulates the depth of the resonance profile. Effectively, the transmission level (indicated by the dot) travels between profiles of different depths. (b) In the FM case, $V(t)$ modulates the microwave carrier detuning Δ_μ, so the transmission level glides along the resonance profile.

where m_{AM} is the relative amplitude-modulation sensitivity [see Appendix C for more details on modulation]. This results in the following modulation of the Rabi frequency:

$$\Omega_{\mathrm{R}}(t) = \Omega_{\mathrm{R},0}\left[1 + m_{\mathrm{AM}} \cdot V(t)\right], \tag{4.6}$$

where $\Omega_{\mathrm{R},0}$ is the value of unmodulated Rabi frequency. In terms of the resonance profile, the amplitude modulation at a constant carrier frequency is equivalent to modulating the resonance depth [see Figure 4.1(a)]. The resulting modulation of optical transmission is given by

$$T^{\mathrm{AM}}(t) \approx T_0 + m_{\mathrm{AM}} V(t) \Omega_{\mathrm{R},0} \left(\frac{\partial T}{\partial \Omega_{\mathrm{R}}}\right), \tag{4.7}$$

which is linearly proportional to the modulating signal $V(t)$.

In the FM case, the affected parameter is the microwave carrier frequency, so that

$$b_{\mathrm{FM}}(t) = b_0 \cos[\omega_\mu t + m_{\mathrm{FM}} V(t) \cdot t + \phi_\mu], \tag{4.8}$$

where m_{FM} is the frequency-modulation sensitivity. As a result, the microwave de-

tuning in the Hamiltonian is modulated as

$$\Delta_\mu(t) \rightarrow \Delta_{\mu,0} + m_{\mathrm{FM}} V(t), \tag{4.9}$$

The resulting transmission is given by

$$T^{\mathrm{FM}}(t) \approx T_0 + m_{\mathrm{FM}} V(t) \left(\frac{\partial T}{\partial \Delta_\mu} \right). \tag{4.10}$$

The frequency modulation at constant microwave amplitude is equivalent to gliding back-and-forth along the resonance line [see Figure 4.1(b)]. As a result, for efficient transduction the microwave carrier frequency must be off-resonance, where the derivative $\partial T/\partial \Delta_\mu$ is non-zero. The characterization of the optical response to microwave modulation, including the dependence of the transduction coefficients $k_{\mathrm{AM}} = \partial T/\partial \Omega_{\mathrm{R}}$ and $k_{\mathrm{FM}} = \partial T/\partial \Delta_\mu$ on the microwave parameters, will be discussed in Section 4.4.

4.3 Setup

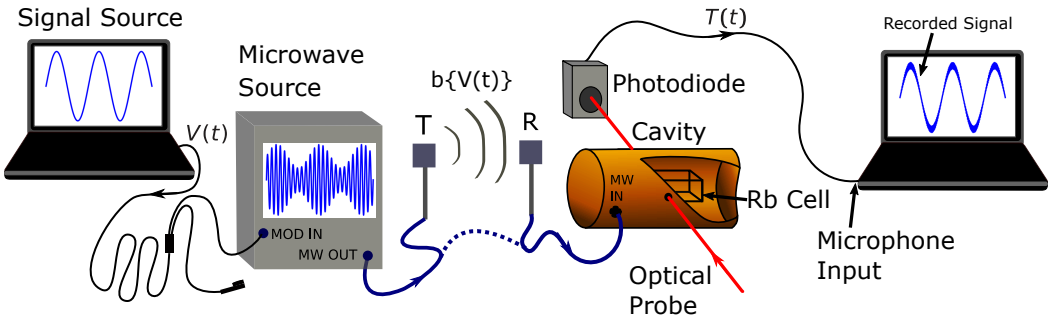

Figure 4.2: Experimental setup. An audio signal $V(t)$ is applied to the external modulation input of a microwave frequency source. The modulated microwave field is transmitted via cable (solid) or antenna (dashed) to a microwave cavity with a vapor cell inside. The atomic vapor transduces the modulation from the microwave carrier to the optical probe intensity, which is converted to voltage via a photodiode (Thorlabs PDA36A) and recorded via a microphone input of a laptop. Figure adapted from [62].

Figure 4.2 shows a schematic of the experimental setup. The main part of the setup is the same as in Chapter 3 with the audio transduction implemented in a room-temperature ^{87}Rb vapor cell inside a microwave cavity. The optical probe addresses

a transition within the D2-line at around 780 nm [see Section 3.5 for more details]. The microwave power and carrier frequency vary depending on the measurement with the exact values indicated in the caption of the corresponding figure. In all cases, the detuning Δ_μ is given with respect to $f_0 = 6.834\ 682\ 610$ GHz.

The microwave field is modulated by the microwave source itself in the "external modulation" regime, where the modulating signal $V(t)$ is applied to the corresponding modulation input of the microwave source. The way the modulation is applied is slightly different in the FM and AM cases. In the FM case, we set the microwave power and the carrier frequency directly, and by adjusting the frequency-modulation sensitivity m_{FM}, we set the deviation of the output microwave frequency from the carrier frequency, with typical values used ranging $10 - 200$ kHz/V. In the AM case, we still set the microwave power and the carrier frequency directly, but this time the amplitude-modulation sensitivity m_{AM} sets the **relative** deviation, as was shown in Eq. 4.5. Neither of our microwave sources provided sensible results as we varied m_{AM}, so we chose to work with Berkeley Nucleonics 845, which we calibrated by looking at the relative amplitude of the sideband frequency components on a spectral analyzer. From this calibration we extracted a value of $m_{\mathrm{AM}} = 15\%/\mathrm{V}$.

Depending on the measurement, we used different sources for the modulating signal $V(t)$. For the single-frequency response measurements in Section 4.4.1, the signal was derived from an RF source Agilent 33220A. For the measurements of transduction coefficients presented in Section 4.4.2 and signal bandwidth presented in Section 4.4.3, we used the Zurich Instruments HF2LI lock-in amplifier. For the audio transduction, we originally obtained the audio signal in the form of electric voltage from a laptop's headphone output. In order to apply the audio signal to the modulation input of the microwave source, we cut off one speaker from a headphones pair and soldered the corresponding contacts to a BNC jack. To record the transduced signal from the optical field, we applied the photodetector voltage to the microphone input of a laptop. To do that, we cut off the wire from another pair of headphones and soldered

its microphone contacts to another BNC jack. For the signal recording and editing we used the free software Audacity.

In the spirit of radio-over-fiber applications, we demonstrated successful transduction with the microwave field transmitted to the cavity via air. For this purpose, we used FXUWB10.01 3-10GHz Ultra Wideband Flex Antennas from Taoglas connected to the microwave source and the cavity, as the transmitter and the receiver, respectively.

4.4 Transduction characterization

4.4.1 Single-frequency response

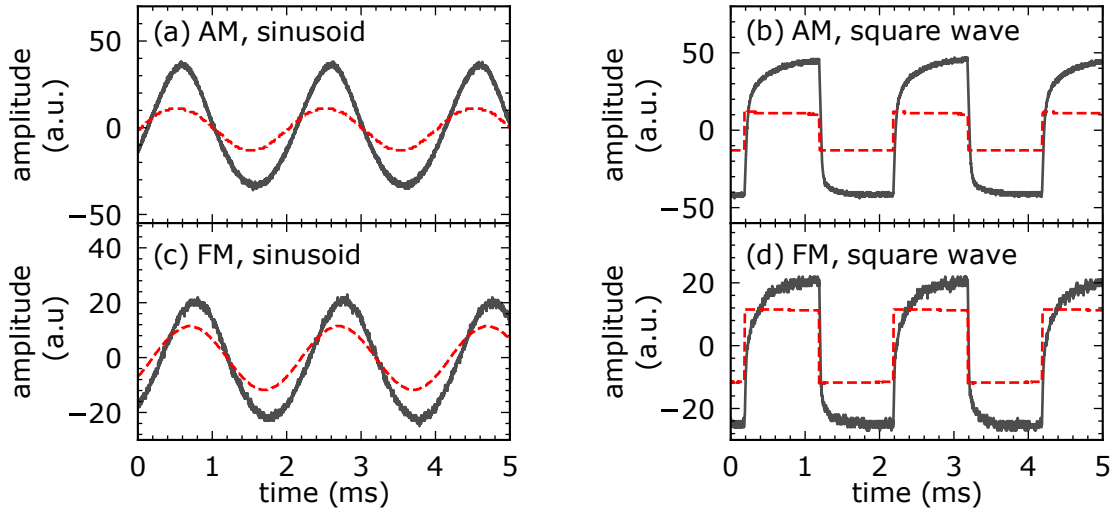

Figure 4.3: Single-frequency responses of optical transmission (grey) in the presence of microwave fields modulated at $\omega_{\mathrm{m}}/2\pi = 500$ Hz (red dashed) with input microwave power $P = 2$ dBm corresponding to $\Omega_{\mathrm{R}}/2\pi = 74$ kHz. (a) Sinusoidal and (b) square-wave amplitude modulation with modulation sensitivity $m_{\mathrm{AM}} = 15\%/\mathrm{V}$ measured at $\Delta_\mu/2\pi = -5$ kHz. (c) Sinusoidal and (d) square-wave frequency modulation with modulation sensitivity of $m_{\mathrm{FM}} = 40$ kHz/V, measured at $\Delta_\mu/2\pi = 95$ kHz. AM and FM depictions are not to scale. Figure reprinted from [62].

To analyze the performance potential and limitations of our method, we carried out a range of measurements, starting with the optical response to a periodic mod-

ulation, which is shown in Figure 4.3. All measurements here are done using the clock transition, which is separated from adjacent transition via the Zeeman effect from an applied static magnetic field. The microwave power was set to $P = 2$ dBm, corresponding to $\Omega_{\mathrm{R}}/2\pi = 74$ kHz. Here and below, we calculate the Rabi frequency from corresponding to the microwave power value using

$$\Omega_{\mathrm{R}} = 2\pi \times 10^{P[\mathrm{dBm}]/20} \times 58.6 \text{ kHz}, \tag{4.11}$$

obtained from the calibration Section 3.6.5.

As is expected from Eq. 4.1, in the case of a harmonic modulating signal $V(t) = V_0 \sin \omega_{\mathrm{m}} t$, both AM and FM responses [Figure 4.3(a, c)] are harmonic oscillations at ω_{m} and slightly out of phase with respect to $V(t)$. A response due to a square-pulse modulation $V(t) = V_0 \mathrm{sgn}[\sin(\omega_{\mathrm{m}} t)]$ [Figure 4.3(b, d)] shows that in both cases there is a finite response time for the optical signal. As a result, the amplitudes and relative phases of the optical signal in both AM and FM cases depend on ω_{m}, which limits the transduction bandwidth, as will be discussed in Section 4.4.3.

4.4.2 Double-resonance profile and transduction coefficients

To provide some context for the bandwidth characterization, we begin with measuring the profile of the microwave-optical double-resonance line, shown in Figure 4.4(a). We performed these measurements on the clock transition isolated with a bias magnetic field. The measurements are done for three values of the microwave power: -10, 0, and $+10$ dBm, corresponding to $\Omega_{\mathrm{R}}/2\pi$ of 18, 60, and 180 kHz, respectively. The optical signal is obtained in a continuous-wave regime while the microwave frequency is swept by an external saw-tooth signal at a 50 Hz repetition rate. In all cases, the FM-modulation sensitivity is set to $m_{\mathrm{FM}} = 1.33\ 501$ MHz/V. For a better resolution for each power value, we adjust the span of the frequency sweep by adjusting the peak-to-peak value of the saw-tooth voltage, which in turn affects the sweeping rate. These peak-to-peak values are ± 2, ± 1, and ± 0.5 V, with the larger values corresponding to

a higher microwave power. In each case, we make sure that the sweeping rate is low enough to provide a symmetric resonance profile [see Section 3.6.4 for the discussion of the relationship between the observed resonance profile and the frequency-sweep rate].

Next, we analyze the transduction coefficients $k_{\mathrm{FM}} = \partial T/\partial \Delta_\mu$ and $k_{\mathrm{AM}} = \partial T/\partial \Omega_{\mathrm{R}}$ obtained via lock-in detection. In both cases, the corresponding microwave parameter is modulated by a sinusoidal voltage

$$V(t) = V_{\mathrm{off}} + V_0 \sin \omega_{\mathrm{m}} t \tag{4.12}$$

provided by the lock-in amplifier. We keep the amplitude V_0 constant, and vary either the voltage offset V_{off} or the modulation frequency ω_{m} as a parameter. The modulation results in an oscillating optical signal, similar to the one shown in Figure 4.3(a,c). On the lock-in amplifier, this optical signal is mixed with $V(t)$, which allows us to extract the amplitude and phase of the signal's spectral component at ω_{m}. According to Eq. 4.7 and Eq. 4.10, the amplitude is proportional to the transduction coefficient, provided that V_0 is sufficiently small. For the k_{FM} and k_{AM} measurements discussed below, we program the lock-in amplifier to scan either parameter of $V(t)$, performing lock-in detection for each parameter value. The duration of $V(t)$ is automatically set by the amplifier, depending on the value of ω_{m}.

Figure 4.4(b) shows k_{FM} as a function of the microwave carrier detuning for the same three values of microwave power as in Figure 4.4(a). For each set of measurements, we vary the detuning by varying V_{off} from -0.5 V to 0.5 V, while keeping $m_{\mathrm{FM}} = 1.33\ 501$ MHz/V, $V_0 = 0.1$ V and $\omega_{\mathrm{m}}/2\pi = 1$ kHz constant. The microwave source is operating in the DC-coupling regime of FM modulation, sensitive to the DC offset of the modulating voltage. According to Eq. 4.9, the resulting microwave detuning is given by

$$\Delta_\mu(t) = \Delta_{\mu,0} + m_{\mathrm{FM}} \left[V_{\mathrm{off}} + V_0 \sin \omega_{\mathrm{m}} t\right] = \tilde{\Delta}_{\mu,0} + m_{\mathrm{FM}} V_0 \sin \omega_{\mathrm{m}} t, \tag{4.13}$$

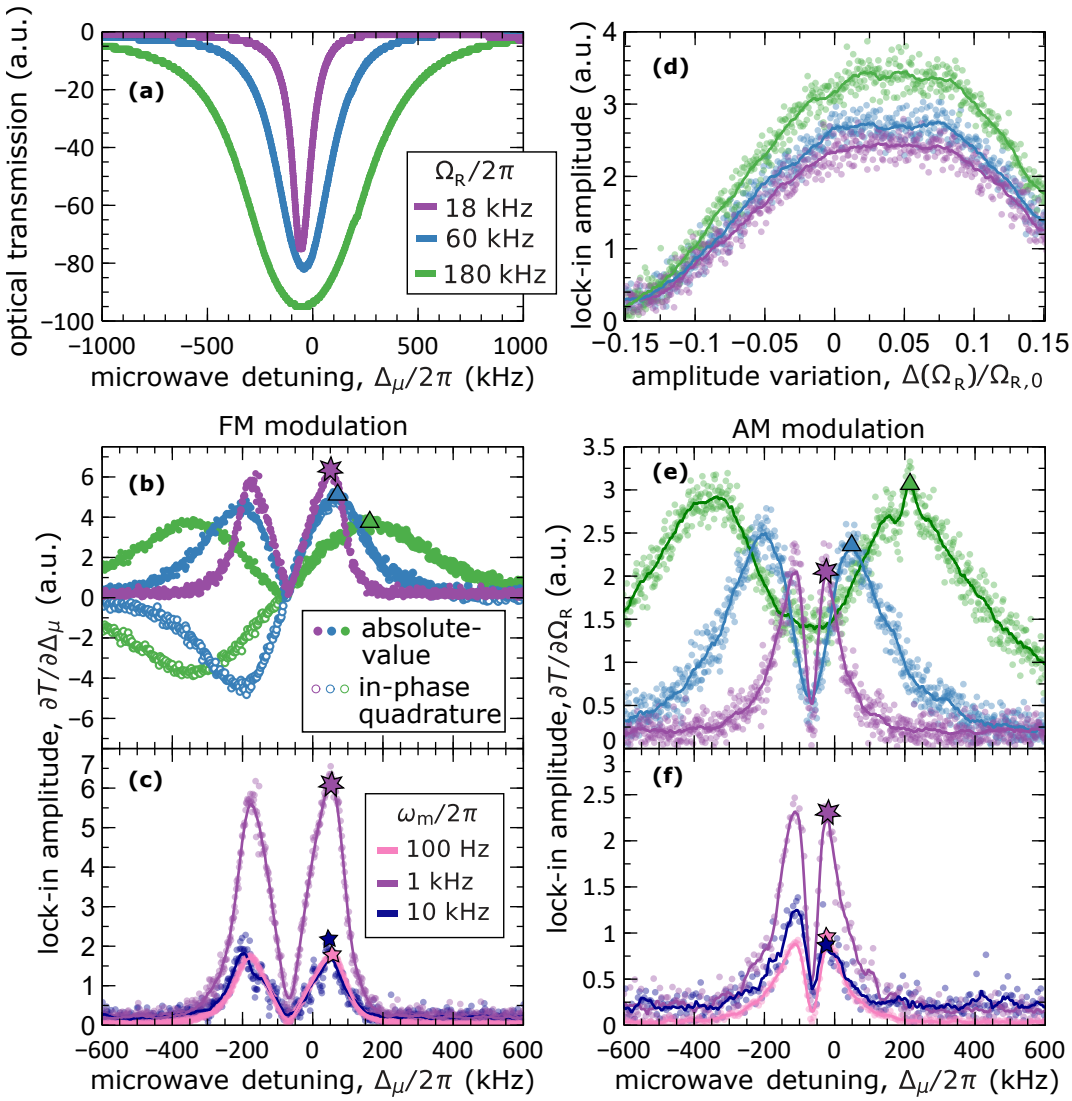

Figure 4.4: Microwave-to-optical transduction calibrations, varying microwave power [Rabi frequencies $\Omega_R/2\pi = 18$ kHz (green), 60 kHz (blue), and 180 kHz (purple)] and modulation frequency for FM (b-c) and AM (e-f) signals. Symbols indicate identical conditions across subfigures within FM, AM categories. (a) Optical probe transmission vs. microwave detuning; (b) lock-in detection signal amplitude for 1-kHz-FM modulated signals, including absolute-value amplitude response (filled) and single-quadrature response (open); (c) lock-in detection amplitude for $\Omega_R/2\pi = 180$ kHz at FM modulation frequencies $\omega_m/2\pi = 0.1$ kHz (pink), 1 kHz (purple), and 10 kHz (navy). (d) Amplitude response during AM at 1 kHz vs change $\Delta(\Omega_R)$ from the nominal Rabi frequency, $\Omega_{R,0}$, where the value of Δ_μ for each $\Omega_{R,0}$ is chosen to maximize the AM response measured in (e); (e) absolute-value lock-in detection amplitude for 1-kHz-AM modulated signals; (f) amplitude response, as in (c), for AM modulation when $\Omega_R/2\pi = 180$ kHz. Figure adapted from [62].

where $\tilde{\Delta}_{\mu,0} = \Delta_{\mu,0} + m_{\mathrm{FM}} V_{\mathrm{off}}$ is the new value of the carrier detuning shifted by V_{off}. Physically, $\tilde{\Delta}_{\mu,0}$ in Eq. 4.13 represents the same entity as Δ_μ in Figure 4.4(a), which is a location on the resonance profile. For this reason, we label it simply as Δ_μ in Figure 4.4(b,c,e,f).

Figure 4.4(c) shows the same measurements for $P = -10$ dBm and three values of the modulation frequency. The fact that the higher modulation frequencies do not affect the peak's position indicates that at these modulation frequencies, the transduction is still in the linear regime where the higher-order harmonics of ω_{m} are negligible. As is expected, the shape of the curves in Figure 4.4(b-c) corresponds to that of the first-order derivatives of the curves in Figure 4.4(a).

To obtain k_{AM} as a function of the microwave detuning shown in Figure 4.4(e,f), we operate the microwave source in both FM and AM regimes simultaneously. Each modulation type uses its own modulating input: the AM input receives a sinusoidal signal with no offset, and the FM input receives a constant voltage. These two signals are provided by two separate channels of the lock-in amplifier. As before, the lock-in amplifier scans the constant voltage, and for each value, it mixes the photodetector signal with the sinusoidal modulating signal to retrieve the parameters of the spectral component at ω_{m}. The resulting graphs show nontrivial dependence on the microwave detuning with prominent peaks that can be used to optimize the signal.

These results suggest that to optimize the transduction efficiency, we need to choose microwave parameters corresponding to peak values of $k_{\mathrm{FM}}(\Delta_\mu)$ and $k_{\mathrm{AM}}(\Delta_\mu)$. Not only does it give a stronger signal, but it also guarantees that the next-order corrections to the signal are suppressed because the second-order derivative is zero. These peak values on the graphs are indicated with special markers.

Figure 4.4(d) shows how k_{AM} depends on the Rabi frequency Ω_{R}. For these measurements, the microwave source operates only in the AM regime with the modulation input as in Eq. 4.12. Unlike the FM case, the modulating signal in the AM regime does not allow us to control the amplitude directly but only relative to the unmodulated

value. According to Eq. 4.6, the modulated Rabi frequency is given by

$$\Omega_{\mathrm{R}}(t) = \Omega_{\mathrm{R},0}\left[1 + m_{\mathrm{AM}} \cdot V_{\mathrm{off}} + m_{\mathrm{AM}} V_0 \sin \omega_{\mathrm{m}} t\right]. \tag{4.14}$$

To see what effect the voltage offset has on the Rabi frequency, we set $V_0 = 0$ in Eq. 4.14 yielding

$$m_{\mathrm{AM}} V_{\mathrm{off}} = \frac{\Omega_{\mathrm{R}}(V_{\mathrm{off}}) - \Omega_{\mathrm{R},0}}{\Omega_{\mathrm{R},0}} = \frac{\Delta\Omega_{\mathrm{R}}}{\Omega_{\mathrm{R},0}}, \tag{4.15}$$

which is what we plot on the x-axis in Figure 4.4(d). For each power level, we choose $\Delta\mu$ that corresponds to a peak in Figure 4.4(e). The graphs show broad plateaus, suggesting that k_{AM} is insensitive to small power fluctuations.

4.4.3 Bandwidth measurements

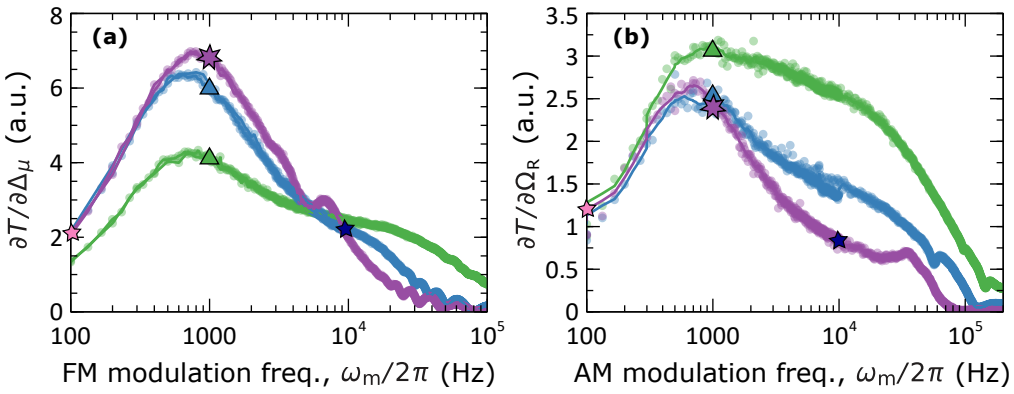

Figure 4.5: Modulation-frequency bandwidth measurements for three values of microwave power corresponding to the following Rabi frequencies: $\Omega_{\mathrm{R}}/2\pi = 18$ kHz (green), 60 kHz (blue), and 180 kHz (purple). (a) FM transduction coefficient vs. the modulation frequency, measured at the detuning with largest amplitude response. (b) AM-transduction coefficient vs. the modulation frequency, measured at the detuning with largest amplitude response. For each type of modulation, markers corresponds to data points from Figure 4.4 measured at the same microwave parameters. Figure adapted from [62].

Next, we estimate the signal bandwidth of the transduction for the optimal parameters obtained above. Figure 4.5 shows the transduction coefficients as a function

of ω_{m} for three values of the microwave power. These measurements are performed via lock-in detection in the same fashion as in the previous section. For each value of microwave power, we use the value of Δ_μ that maximizes the corresponding transduction coefficient in Figure 4.4(b,e). We use the same markers as in Figure 4.4 for the data points corresponding to the same microwave parameters as the marked points in Figure 4.4. From Figure 4.5, we estimate the modulation frequency bandwidth to be on the order of 1 kHz, which is consistent with the square-wave modulation response measurements in Section 4.4.1 that give a typical response time of about 1 ms. The shape of the observed curve resembles the frequency-response curve of a driven damped harmonic oscillator. It is also similar to the shape of the Rabi resonance discussed in Section 3.6.5, which is probably a manifestation of similar origin of these phenomena.

Before moving on to the main results, we would like to highlight the difference between the modulation-frequency bandwidth discussed above and the carrier-frequency bandwidth. The modulation-frequency bandwidth determines what frequency components of the transduced audio signal can be efficiently converted. This is different from the carrier frequency bandwidth, which determines what microwave frequencies can be used for efficient signal transmission. In our setup, the carrier-frequency bandwidth is ultimately limited by the cavity linewidth. Within this limit, this bandwidth can be extended by operating on magneto-sensitive hyperfine transitions whose frequencies can be adjusted with external static magnetic fields. If the carrier-frequency bandwidth is an issue, it might be advantageous to increase the cavity linewidth while sacrificing the Q-factor and coupling strength.

4.5 Transduction results

Figure 4.6 shows our proof-of-concept results on the microwave-to-optical transduction of an audio signal in both AM and FM regimes. The baseband signal corresponds to a license-free song and is shown in Figure 4.6(a), where the voltage from

the headphone output was applied directly to the microphone input. We demonstrate successful transduction not only when the microwave is transmitted to the cavity via cable [Figure 4.6(b,d)] but also when it is transmitted via air between two antennas separated by 30 cm.

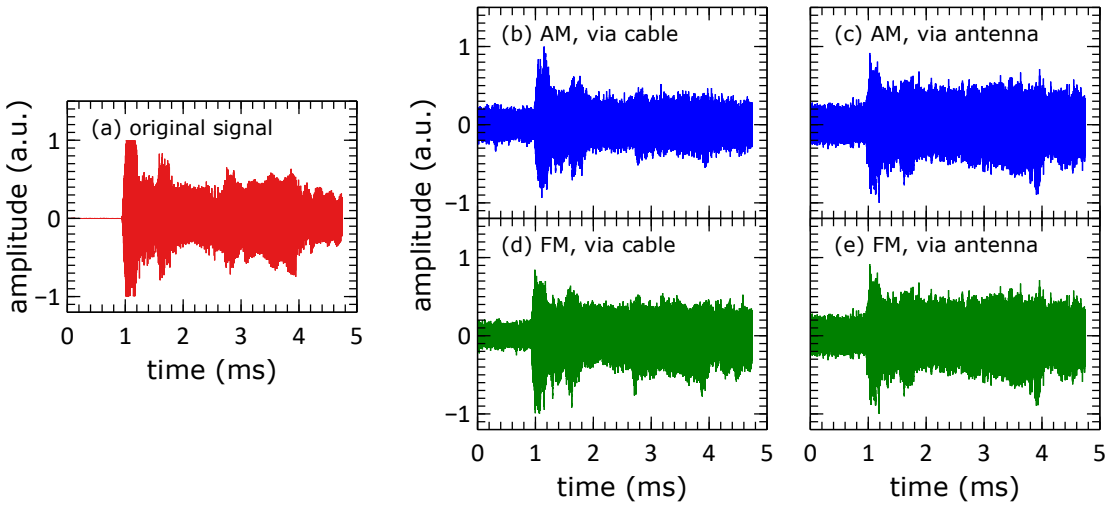

Figure 4.6: Audio signal transduction. (a) Original audio signal $V(t)$ used to modulate the microwave carrier ω_μ. (b, c) Optical transmission of amplitude modulated signal at $\omega_\mu/2\pi = 6.834\ 682\ 610$-GHz [transmitted via cable (b) and 30-cm-separated antennas (c)] for microwave input power $P = -5$ dBm and $m_{\mathrm{AM}} = 15\%/V$. (d, e) Optical transmission of frequency modulated signal at $m_{\mathrm{FM}} = 150$ kHz/V. (d) Signal transmitted over cable for microwave input power $P = -10$ dBm and $\omega_\mu/2\pi = 6.834\ 874\ 610$-GHz. (e) Signal transmitted over 30-cm-separated antennas for MW input power $P = +8$ dBm and $\omega_\mu/2\pi = 6.834\ 877\ 610$-GHz. In all cases, a static bias magnetic field is applied to cancel stray magnetic fields. Figure adapted from [62].

For the recordings shown in Figure 4.6(b-e), we pass the photodetector voltage through two AC filters that cut off DC voltage offset and AC frequency components above 20 MHz. For the sake of experimental integrity, we made sure that the recording software did not perform any signal editing, such as digital filtering or noise reduction. However, we note that using these techniques greatly improves the signal quality.

To monitor the transduction quality in real time, we applied the photovoltage to a speaker and an oscilloscope, which allowed us to listen to the resulting signal and see

its shape. In each scenario, we choose the microwave parameters that provide the best audio signal clarity and most symmetric waveform. We note the optimal parameters obtained in this case are different from those maximizing the transduction coefficients in the previous section, which requires additional investigation.

4.6 Practicality and feasibility of our method

In this section, we would like to discuss how our transduction method compares to atomic transducers based on the electric-dipole interaction coupling to Rydberg states. First, our method requires only a single 780 nm laser, while the Rydberg-based approach in the case of ^{87}Rb additionally uses a 480 nm laser, which makes the setup significantly more expensive and complicates optical alignment and stabilization. Second, at the time of writing this manuscript, other Rydberg-based methods have only demonstrated transduction in vapor cells that are directly exposed to the traveling microwave field. Practically, it means that the location and orientation of the vapor cell with respect to the microwave field is critical for good reception, while the precise alignment of the probe and coupling beams required for the electromagnetically-induced transparency significantly limits the portability of the setup. In our case, the microwaves are picked up by an antenna non-rigidly attached to the cavity. This allows optimizing the reception by adjusting the antenna while keeping the vapor cell stationary. Finally, the Rydberg states are highly susceptible to stray electric fields, which is not the case in our approach.

The main drawback of our method is the limited option concerning the choice of the carrier frequency. In our case, it is tied to the ground-state hyperfine splitting of our atom of choice, while the electric-dipole approach allows switching between a broad range of carrier frequencies without any alterations to the setup by choosing different pairs of Rydberg states [51]. Still, our approach is feasible if the device needs to operate at a particular known carrier frequency. In this case, this frequency can be addressed by carefully choosing the atomic species with the closest transition

frequency, which can be further shifted by external magnetic or electric fields, while selecting appropriate cavity dimensions.

4.7 Conclusions and outlook

In conclusion, we developed a novel method for microwave-to-optical transduction for radio-over-fiber application and demonstrated proof-of-principle transduction of an audio signal in FM and AM regimes. Our approach is based on cavity-enhanced magnetic-dipole interaction between the microwave field and an alkali atomic vapor and requires an easier and cheaper setup compared to atomic transducers based on the electric-dipole coupling. Via lock-in detection, we characterized the transduction performance and bandwidth that show non-trivial dependence on several microwave parameters.

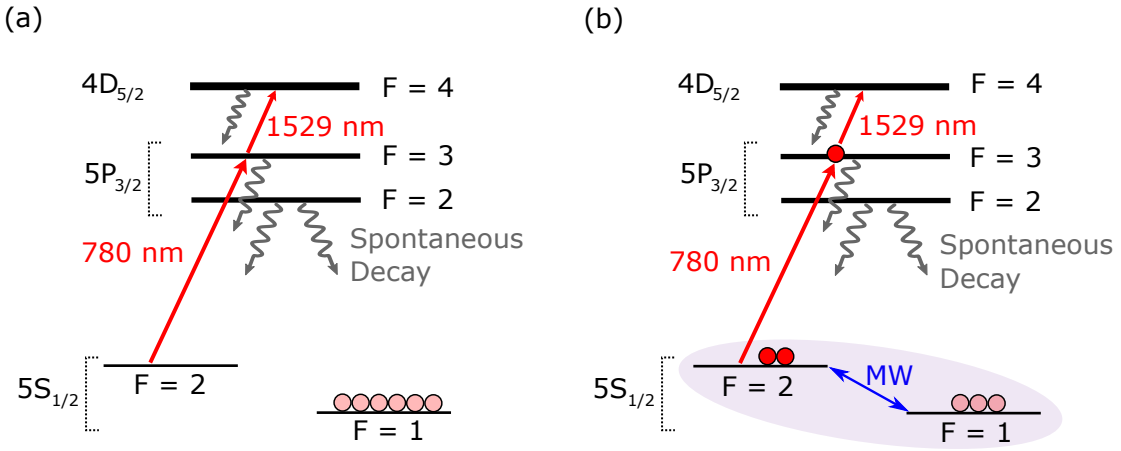

Figure 4.7: Schematics of the proposed microwave-to-telecom transduction principle in ^{87}Rb. (a) In the absence of a microwave field, 780 nm light tuned to $\left|5S_{1/2}, F = 2\right\rangle \rightarrow \left|5P_{3/2}, F = 3\right\rangle$ transition optically pumps atomic population into the dark state $\left|5S_{1/2}, F = 1\right\rangle$ via off-resonant excitation to $\left|5P_{3/2}, F = 2\right\rangle$ state. (b) Microwave (MW) field creates non-zero population of state $\left|5S_{1/2}, F = 2\right\rangle$ and 780 nm light creates non-zero population of $\left|5P_{3/2}, F = 3\right\rangle$. The latter affects absorptive and dispersive properties of $\left|5P_{3/2}, F = 3\right\rangle \rightarrow \left|4D_{5/2}, F = 4\right\rangle$ transition at 1529 nm.

We believe that the transduction method presented here can be further extended. First, for practical applications, the simplest dipole antennas used in our setup for

microwave transmission and reception can be replaced with horn antennas to reduce the power losses during transmission. Second, Figure 4.3(b,d) suggests that the method is readily available for digital FM and AM signal encoding. Third, as will be discussed in Chapter 6, with a microwave field, we can control not only absorptive but also dispersive properties of the atomic vapor, which suggests this method can be extended to encode information using phase-shift keying [54, 58, 105]. Finally, we believe it is possible to upgrade our method for transduction from microwaves to telecom C-band light at 1529 nm. Figure 4.7 illustrates the transduction principle with the relevant levels and transitions. In recent experiments on Faraday lasing in Rb vapors [106, 107], it was shown that with 780 nm, it is possible to alter optical properties of ^{87}Rb vapor at 1529 nm, corresponding to $5P_{3/2} \rightarrow 4D_{5/2}$ transition. This is done by creating a non-zero population [108] in the excited $5P_{3/2}$ state with 780 nm light. Through a two-photon transition, this population will be affected by a microwave magnetic field coupled to the ground-state hyperfine levels, which provides opportunities for microwave-to-telecom transduction using the same principle as the original method.

Chapter 5

AC magnetometry in cold atoms

This Chapter presents our investigation of the dynamics of a two-level system with a phase-modulated coupling going beyond the standard approaches based on the small-signal approximation. Chronologically, this was the first project completed during my Ph.D. program, done while waiting for the warm-atom apparatus components from Chapters 3-4. It started out as an attempt to numerically simulate the Rabi resonance in a two-level system with phase-modulated coupling used in experiments on AC-magnetometry in warm atoms, such as described in Section 3.6.5. The resulting dynamic steady state showed a much richer spectrum than that reported in the literature. As it turned out, the high modulation depth is what made the difference, and lowering its value in the simulation yielded the only two harmonics expected from the literature. Curious if this was a physical result and not just a numerical artifact, I convinced my colleagues, who were at that time working indefatigably on the quantum memory experiments [109], to let me use their ultracold-atom apparatus to make a set of proof-of-principle measurements. The apparatus had the capability of driving the hyperfine transitions with a microwave system set up by Christian Prosko [110], but it was not consistently used. Together with Taras Hrushevskyi, during the last week of 2017, we readjusted the microwave system and tweaked the ultracold-apparatus settings to observe the first microwave-optical double-resonance signal in cold atoms. In the case of the strongly-modulated

phase of the microwave field, the observations were not too different from the simulations, at least qualitatively. These findings motivated further research of the quantum dynamics in this setup and its possible practical applications, which we published in *Phys. Rev. A* 99, 043402 (2019) [63].

The content of this Chapter rather closely follows that of Ref. [63], with some additional details and discussions. Since this was our first attempt to study the double-resonance, we were still developing our understanding and intuition of this phenomenon. As a result, some of our research directions were exploratory and sporadic. In the following narrative, I tried to preserve our original logic and motivation while establishing connections to the theoretical framework presented in Chapter 3. After a brief introduction in Section 5.2, we discuss our results of the numerical simulation of a two-level system driven by a phase-modulated coupling. Section 5.3 and Section 5.4 describe the experimental setup and results, respectively.

5.1 Introduction

This project expands upon the "atomic candle" technique, which exploits the Rabi resonances arising in a double-resonance signal in a two-level system driven by a phase-modulated microwave field [see Chapter 3 for the description of these phenomena]. It was first developed in warm atomic vapors for microwave power stabilization [111] and later modified for warm-atom AC magnetometry. The practicality of the atomic candle technique for AC magnetometry was demonstrated inside microwave cavities [46, 95], inside microwave wave-guides [42, 43, 96], and in free space [45, 46, 48, 49, 97, 112]. It was also shown that using multi-species vapor cells [46] and external static magnetic fields [95] extends the AC-magnetometry bandwidth and allows using of the vapor cell as a vector network analyzer.

All these experiments were demonstrated in warm-atoms with continuous-wave laser and microwave interrogation. In this case, the phase-modulated microwave can be operated in the small-signal regime where the microwave signal is dominated by the

first two harmonics of the modulation frequency, allowing a straight-forward analytical solution. In our approach, we explore the cases of interaction beyond the small-signal approximation. Even though we did not aim for any practical applications at the beginning of this project, we present our findings in the context of a possible adaptation of the atomic-candle AC magnetometry for cold-atom ensembles.

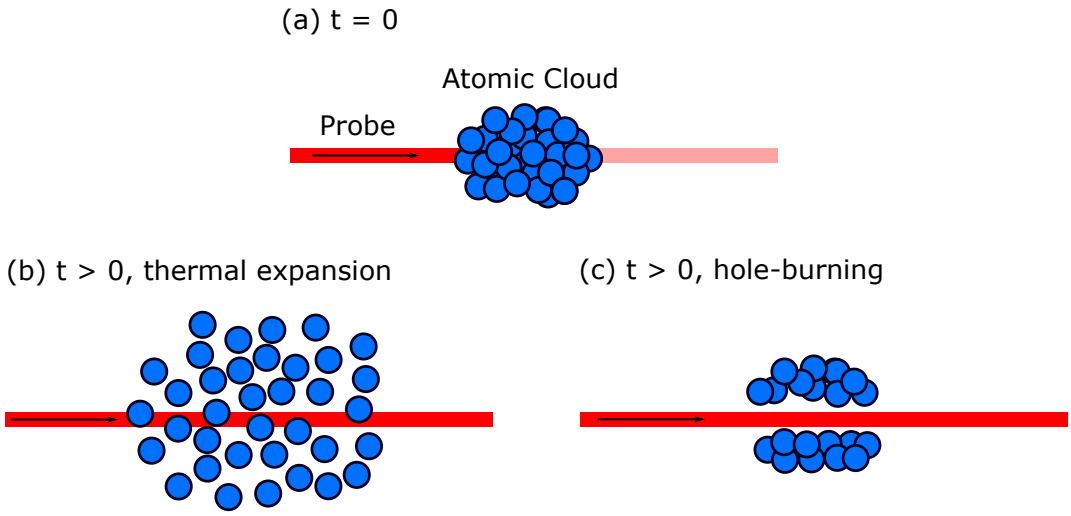

Figure 5.1: Illustration of two processes limiting optical interrogation time in a cloud of cold atoms. (a) Right after the laser-cooling stage, a dense atomic cloud efficiently absorbs the optical probe. (b) Thermal expansion decreases the number of interrogated atoms. (c) Momentum transfer after absorbing a photon from the probe burns a hole in the cloud, reducing the number of interrogated atoms. In real experiments, both processes happen simultaneously.

The use of the atomic candle-technique in cold atoms faces the following challenges. First, the double-resonance imaging can not be applied during the magneto-optical trapping and optical molasses cooling [will be described in Section 5.2]. The reason is that during these stages, the atoms interact with a bichromatic laser field and undergo continuous excitation-emission cycles, which compromises the theoretical framework of the double-resonance imaging. As a result, the interrogation should be performed after the cooling stage. In this situation, the interrogation time is limited due to the thermal expansion of the atomic cloud [see Figure 5.1(b)] and a hole-burning caused by a momentum transfer from the probe laser [see Figure 5.1(c)].

The limited interrogation time dramatically reduces the method's sensitivity due to a small number of observed cycles. This chapter investigates how going beyond the small-signal regime and focusing on a higher-order harmonic can help overcome this challenge and make the technique applicable for cold-atom systems.

5.2 Numerical simulation

5.2.1 Theoretical model

To simulate the atomic response to a phase-modulated magnetic field, we use a two-level model. The excited state $|2\rangle$ corresponds to a Zeeman sublevel from level $F = 2$, and the ground state $|1\rangle$ corresponds to a Zeeman sublevel from level $F = 1$. We assume that the microwave field couples only these two levels and that the coupling operator $\hat{V}$ has only off-diagonal matrix elements, such that $\langle 1|\hat{V}|2\rangle = \langle 2|\hat{V}|1\rangle = \hbar\Omega_{\mathrm{R}}$. For a phase-modulated field $b(t) = b_0 \cos[\omega t + \theta(t)]$, the two-level system Hamiltonian in the rotating-wave approximation is given by

$$\hat{H}(t) = \frac{\hbar}{2}\left(\Omega_{\mathrm{R}}\hat{\sigma}_x - [\delta + \dot{\theta}(t)]\hat{\sigma}_z\right), \tag{5.1}$$

where δ is the carrier-frequency detuning from the two-level resonance. For the rest of this Chapter, we will always assume harmonic phase modulation

$$\theta(t) = m \sin \omega_{\mathrm{m}} t, \tag{5.2}$$

where m is the modulation depth, and ω_{m} is the modulation frequency. We do not directly include in the model the interaction with the optical probe but take into account its effect on the quantum state as the transverse and longitudinal relaxation.

Assuming that the rotating-wave approximation is valid, we describe the evolution of the two-level system using the pseudo-spin approach introduced in Section 2.3.2.

In terms of the pseudo-spin components, Eq. 2.17 can be written as

$$\dot{\nu}_x = [\delta + \dot{\theta}(t)]v_y - \Gamma_2\nu_x, \tag{5.3}$$

$$\dot{\nu}_y = -[\delta + \dot{\theta}(t)]\nu_x + \Omega_R\nu_z - \Gamma_2\nu_y, \tag{5.4}$$

$$\dot{\nu}_z = -\Omega_R\nu_y - \Gamma_1[\nu_z + 1], \tag{5.5}$$

where Γ_1 and Γ_2 are the longitudinal and transverse relaxation rates, respectively. We are particularly interested in the level populations, which can be found using the fact that $v_z = \rho_{22} - \rho_{11}$ and $\rho_{22} + \rho_{11} = 1$. We solve Eqs. 5.3-5.5 in Python 2.7 using the built-in integration function **odeint** from the SciPy package.

5.2.2 Time evolution: weak modulation

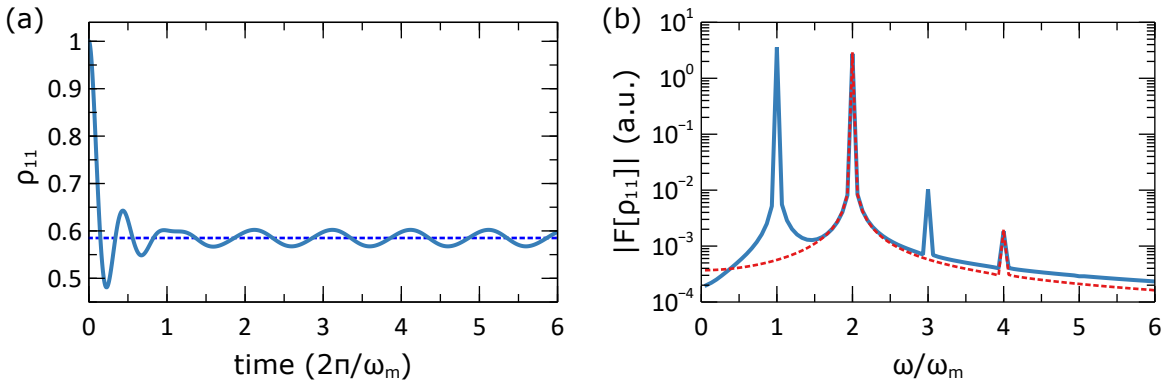

Figure 5.2: (a) Simulated evolution of the ground-state population in a two-level system driven by phase-modulated field. The simulation is done for $m = 1$, $\omega_m = \delta = 0.5\Omega_R$, and $\Gamma_1 = 2\Gamma_2 = \Omega_R$. The dashed line indicates the steady-state level for a two-level system by a field with the same parameters with no modulation. (b) Fast Fourier Transform of the simulated steady-state population oscillations for $\delta = 0.1\omega_m$ (blue solid curve) and $\delta = 0$ (red dashed), with the rest of the parameters the same as in (a). Figure adapted from [63].

Figure 5.2(a) shows the numerical solution of Eqs. 5.3-5.5 in terms of the ground-state population for relatively weak modulation depth. In this case, the dynamic steady-state population oscillates around its unmodulated value. This fact can be considered as rationale for the small-signal approximation, which we already encountered in Section 3.6.5. In this approximation, $\dot{\theta}(t)$ is treated as a perturbation [41],

which allows us to rewrite the steady-state pseudo-spin component and the population as

$$\rho_{22}(t) = \rho_{22,0} + \rho_{22,\mathrm{m}}(t), \tag{5.6}$$

$$\nu_x(t) = \nu_{x,0} + \nu_{x,\mathrm{m}}(t), \tag{5.7}$$

$$\nu_y(t) = \nu_{y,0} + \nu_{y,\mathrm{m}}(t), \tag{5.8}$$

where $\rho_{22,0}, \nu_{x,0}, \nu_{y,0}$ are the steady-state value with no modulation, and $\rho_{22,\mathrm{m}}, \nu_{x,\mathrm{m}}, \nu_{y,\mathrm{m}}$ describe the correction due to the phase modulation.

From Eqs. 5.3-5.5, it follows that the dynamic part of the steady-state population is given by

$$\ddot{\rho}_{22,\mathrm{m}} + \Gamma_1\dot{\rho}_{22,\mathrm{m}} + \Omega_{\mathrm{R}}^2\rho_{22,\mathrm{m}} = \frac{\Omega_{\mathrm{R}}}{2}\left[\Gamma_2\nu_{y,\mathrm{m}} + (\delta + \dot{\theta})\nu_{x,\mathrm{m}} + \dot{\theta}\nu_{x,0}\right]. \tag{5.9}$$

Here, the left-hand side describes damped harmonic oscillations, while the right-hand side can be interpreted as the driving force caused by the phase modulation and coherence between the levels (described by ν_x and ν_y). In the small-signal approximation, defined by the conditions $m < \sqrt{2\Gamma_1/\omega_{\mathrm{m}}}$ and $\Gamma_2 \ll \omega_{\mathrm{m}}$, Eq. 5.9 has an analytical solution, given by Eq. 3.11.

According to the analytical solution, the dynamic steady-state is comprised of oscillations at two harmonics of the modulation frequency, with the first harmonic vanishing when the driving field is exactly on resonance. Figure 5.2 (b) shows the spectra of the dynamic steady-state population ρ_{11}, simulated for $\delta = 0$ and $\delta = 0.1\omega_m$, which are dominated by first and second harmonics. In agreement with the analytical predictions, the first harmonic disappears when the carrier is on resonance. The simulation shows that the dynamic steady-state spectrum also contains higher-order third and fourth harmonics. This is probably due to the fact that the relaxation rates are comparable with the modulation frequency violating the small-signal approximation. Below we investigate the behavior of these higher-order harmonics on the modulation in the strong-modulation regime.

5.2.3 Time evolution: strong modulation

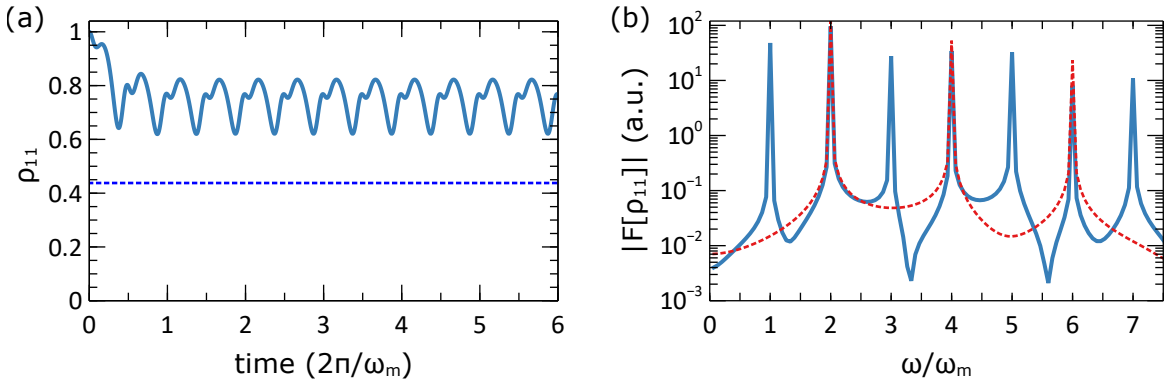

Figure 5.3: (a) Simulated evolution of the ground-state population in a two-level system driven by phase-modulated field. The simulation is done for $m = 6$, $\Omega_{\mathrm{R}} = 1.5\omega_{\mathrm{m}}$, $\delta = 0$, and $\Gamma_1 = 2\Gamma_2 = 0.8\omega_{\mathrm{m}}$. The dashed line indicates the steady-state level for a two-level system by a field with the same parameters with no modulation. (b) Fast Fourier Transform of the simulated steady-state population oscillations for $\delta = \omega$m (blue solid curve) and $\delta = 0$ (red dashed), with the rest of the parameters the same as in (a). Figure adapted from [63].

A general solution for the steady-state dynamics of a two-level system driven by a phase-modulated field was obtained in Ref. [113] for the case of $\Gamma_1 = \Gamma_2$. Yet, there is no simple analytical form for the case of strong modulation and arbitrary relaxation rates, so we study this case numerically.

Figure 5.3(a) shows the population in the ground state simulated for $m = 6$ radians. Unlike the case of weak modulation, the average value of the dynamic part is significantly shifted from the unmodulated steady-state level, meaning the effect of phase modulation can no longer be treated as a perturbation. The calculated spectrum in Figure 5.3(b) shows that the dynamic steady state consists of integer oscillations at multiples of the modulation frequency:

$$\rho_{11}(t) = \sum_n P_n \sin(n\omega_m t + \phi_n), \tag{5.10}$$

where n is a positive integer number, and ϕ_n is the relative phase of the particular harmonic. Similarly to the weak-modulation case, all odd harmonics disappear

when $\delta = 0$.

5.2.4 Rabi resonances

In this section, we examine the resonances behavior of the amplitudes of the second and fourth harmonics simulated for $\delta = 0$. For the analysis, we take the steady-state part of the population evolution, corresponding to $t \gg 1/\Gamma_1$. From these data, we extract amplitudes a_n and b_n of the quadrature components of the oscillations using

$$a_n = \frac{1}{N}\sum_{k=1}^{N} \rho_{11}(t_k) \sin n\omega_{\mathrm{m}} t_k, \tag{5.11}$$

$$b_n = \frac{1}{N}\sum_{k=1}^{N} \rho_{11}(t_k) \cos n\omega_{\mathrm{m}} t_k, \tag{5.12}$$

where t_k are evenly spaced time points, and N is the total number of points in the analyzed data set. The overall amplitude of the n^{th} harmonic is given by

$$P_n = 2\sqrt{a^2 + b^2}. \tag{5.13}$$

Eqs. 5.11-5.12 represent a numerical implementation of the principle of lock-in detection. It relies on the fact that, for $n \neq m$,

$$\lim_{T\to\infty} \frac{1}{T}\int_0^T \sin(n\omega t)\sin(m\omega t)dt = \lim_{T\to\infty} \frac{1}{T}\int_0^T \sin(n\omega t)\cos(m\omega t)dt = 0, \tag{5.14}$$

and

$$\lim_{T\to\infty} \frac{1}{T}\int_0^T \sin(n\omega t)\cos(n\omega t)dt = 0. \tag{5.15}$$

Because in our case, N is finite, the contribution to P_n from the unwanted harmonics is small but noticeable. To reduce this contribution, we perform numerical spectral filtering to the data set before extracting a_n and b_n. During the filtering stage, we apply the Fast Fourier Transform (FFT), null the unwanted harmonics in the Fourier domain, and apply the inverse transform. To eliminate the numerical artifacts arising from the finite duration of the analyzed signal, we additionally apply a Hamming window after the inverse FFT. The functions for the FFT and Hamming window were taken from the SciPy and NumPy libraries, respectively.

Low relaxation rate

Figures 5.4(a) shows the extracted amplitudes P_2 and P_4 in the case when $\Gamma_1, \Gamma_2 \ll \omega_{\mathrm{m}}$ and $m = 0.25$. In the simulation, we vary the Rabi frequency while keeping the modulation frequency constant. The second harmonic shows a resonant behavior around $\Omega_{\mathrm{R}} = 2\omega_{\mathrm{m}}$, which is in agreement with analytical results in the small-signal approximation. The fourth harmonic shows two peaks: one around $\Omega_{\mathrm{R}} = 2\omega_{\mathrm{m}}$ and the other one around $\Omega_{\mathrm{R}} = 4\omega_{\mathrm{m}}$. The second peak is similar to a frequency response of a damped harmonic oscillator with natural frequency Ω_R driven at frequency $4\omega_{\mathrm{m}}$, and that is what we expected by analogy to the Rabi resonances of the first and second harmonics. The origin of the fourth-harmonic resonance at $\Omega_{\mathrm{R}} = 2\omega_{\mathrm{m}}$ is unknown, and the fact that we apply digital filtering before extracting the amplitudes guarantees that there is no contribution from other frequency components. Note that both fourth-harmonic peaks are three orders of magnitude lower than the second-harmonic peak.

Figure 5.4(b) shows that as we increase the modulation index, all resonances shift towards lower values of $\Omega_{\mathrm{R}}/\omega_{\mathrm{m}}$ with respect to their weak-modulation positions. Figure 5.4(c) depicts how the shifts' magnitudes depend on the modulation depth, showing that the location of the $4\omega_{\mathrm{m}}$ peak is not affected as strongly as that of the $2\omega_{\mathrm{m}}$ peaks. Besides, the $2\omega_{\mathrm{m}}$ peaks experience a distortion in their shape, leading to an increased linewidth.

Another effect of the higher modulation depth is the increased peak amplitudes. Figure 5.4(d) shows heights of the second-harmonic peak (i.e., $P_{2,r}$) and of the higher-frequency fourth-harmonic peak (i.e., $P_{4,r}$), as a function of m. As is expected from the small-signal approximation, $P_{2,r}$ shows a quadratic dependence on m at weak modulation, which is no longer the case at larger m. Meanwhile, $P_{4,r}$ scales as the fourth power of the modulation depth. This fact provided us the original insight for our argument towards the possible origin of the harmonics as the series expansion of

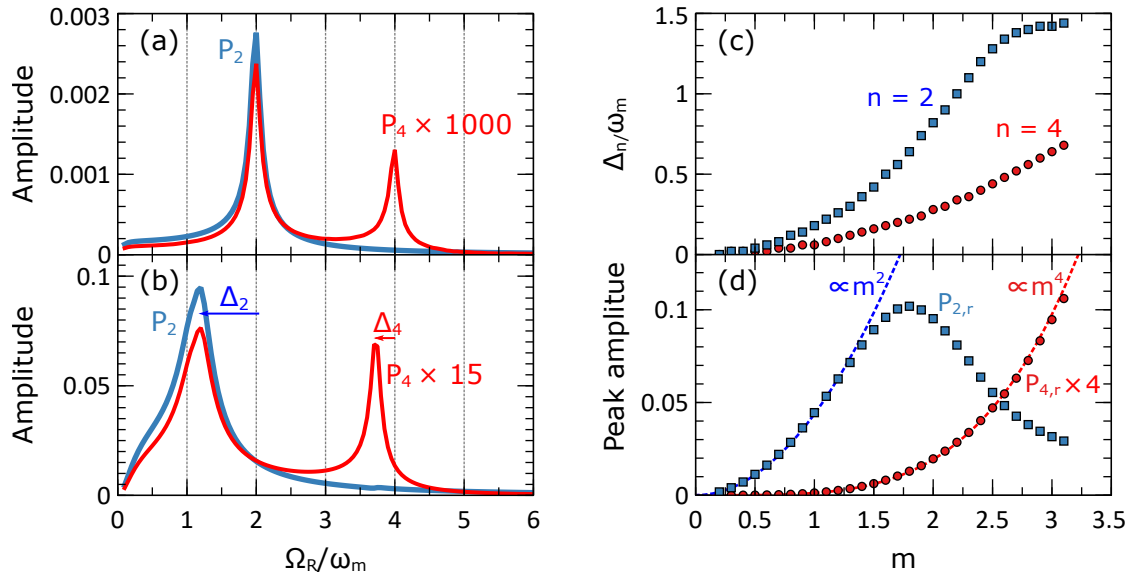

Figure 5.4: Rabi resonances for second (P_2) and fourth (P_4) harmonics for (a) $m = 0.25$ and (b) $m = 2$. The amplitude of the fourth harmonic is scaled as indicated. As the modulation depth is increased, the peaks experience a shift with respect to their original positions $\Omega_R = 2\omega_m$ and $\Omega_R = 4\omega_m$, indicated as Δ_2 and Δ_4, respectively. (c) Shifts of the peaks as a function of the modulation index. (d) Heights of the resonance peaks as a function of the modulation depth. For the fourth harmonic, we use the right-hand peak. Curves indicate the power dependence on m. In all graphs, the simulation was made for $\delta = 0$, and $\Gamma_1 = 2\Gamma_2 = 0.08\omega_m$. Figure adapted from [63].

the double-resonance signal, presented at the end of Section 3.6.5.

In summary, using the strong modulation in a low-relaxation regime leads to a higher peak amplitudes and thus might be used to improve the signal-to-noise ratio. In this setup, the higher-frequency fourth-harmonic Rabi resonance shows a larger height and lower width, making it a better candidate for the AC-magnetometry applications.

High relaxation rate

From the small-signal approximation, we expect the second-harmonic resonance to widen as the relaxation rates increase. This is what we observe in Figure 5.5(a), and this effect holds true for the fourth harmonic as well, for which the two peaks now overlap. Even in the case of weak modulation, the second-harmonic resonance is significantly distorted from a Lorentzian shape, signifying that the small-signal

approximation is no longer valid. Yet, the peak's position is almost unchanged. In a strong-modulation regime, shown in Figure 5.5(b), the broadening and distortion of the resonance line make the technique unsuitable for applications in magnetometry or power standards.

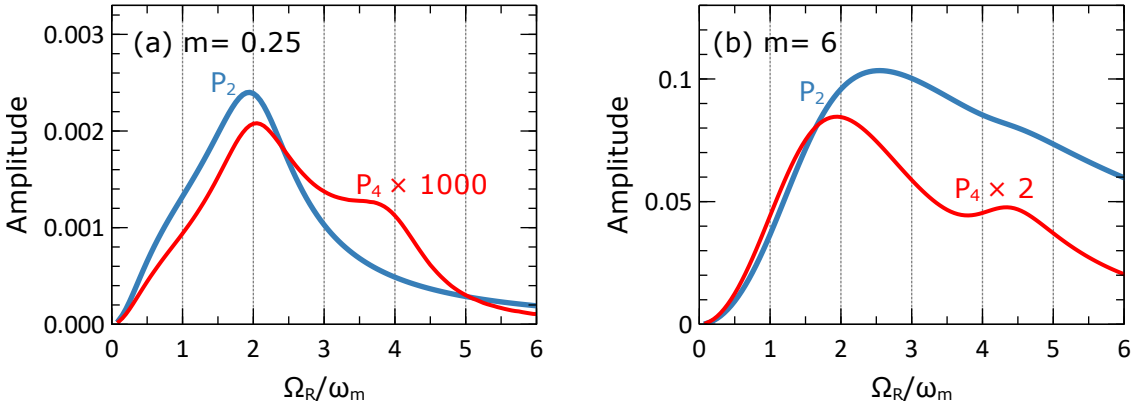

Figure 5.5: Rabi resonances for second (P_2) and fourth (P_4) harmonics for (a) $m = 0.25$ and (b) $m = 6$. The amplitude of the fourth harmonic is scaled as indicated. As the modulation depth is increased, the peaks experience a shift with respect to their original positions $\Omega_R = 2\omega_m$ $\Omega_R = 4\omega_m$, which is indicated as Δ_2 and Δ_4, respectively. In all graphs, the simulation was made for $\delta = 0$, and $\Gamma_1 = 2\Gamma_2 = 0.8\omega_m$. Figure adapted from [63].

5.3 Experimental setup

The experiment was done in the ultracold atom apparatus designed for quantum simulations with ^{87}Rb Bose-Einstein condensates. The apparatus itself is described in great detail in Taras Hrushevskyi's M.Sc. thesis [81], so here we will briefly cover only the main components relevant to our measurements. The experimental measurements are done in a vapor cell attached to an ultrahigh vacuum system. The system is designed to maintain the pressure inside the cell below 10^{-11} Torr, with ^{87}Rb atoms introduced to the cell in a controlled manner. The cell provides optical access for several laser beams. The laser system for the frequency stabilization and control is analogous to the one used in the warm-atom experiment. The static magnetic field in

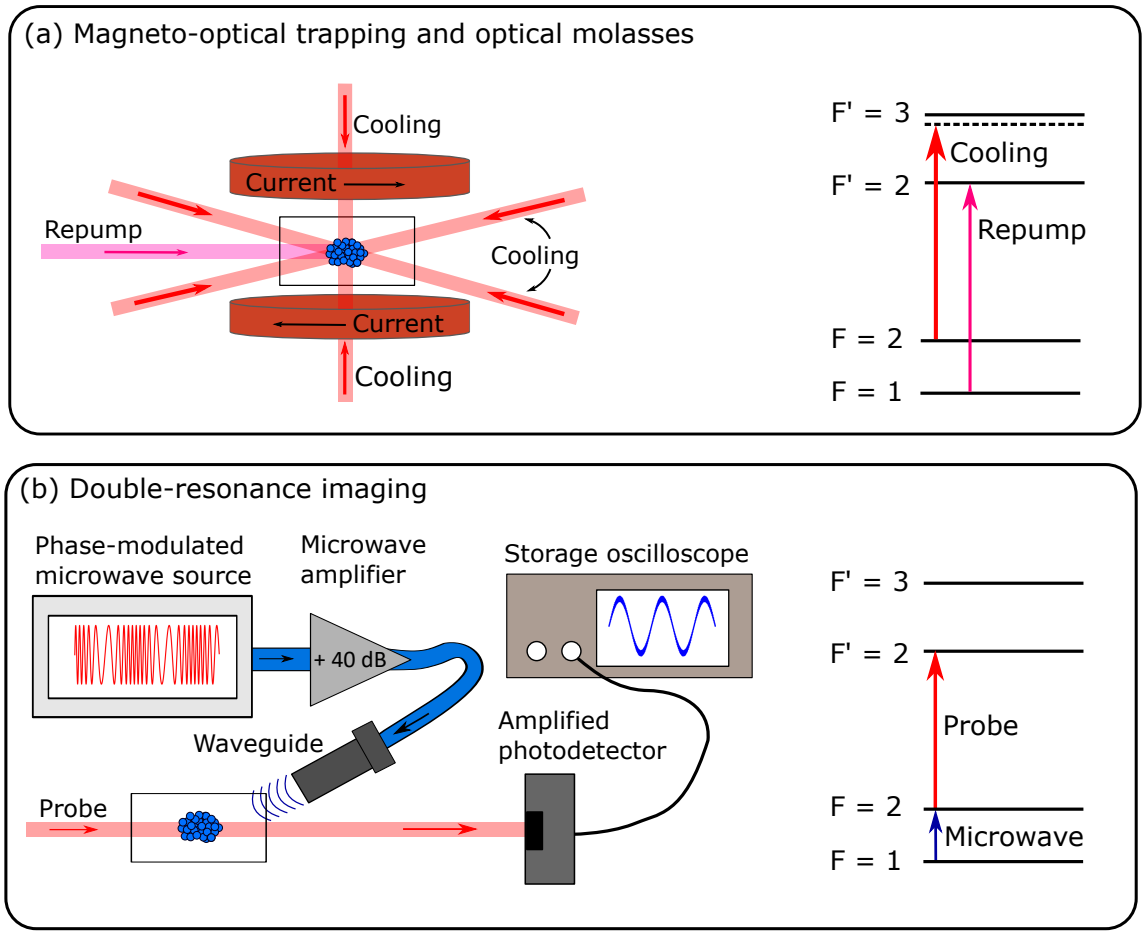

Figure 5.6: (a) Schematics of the laser beams arrangement and transitions for the magneto-optical trapping and the optical molasses. During the optical molasses, we switch off the current in the anti-Helmholtz coils and sweep the cooling laser detuning. (b) Schematics of the microwave setup and transitions for double-resonance imaging. Figure (b) was adapted from [63].

the cell is controlled with three pairs of coils in Helmholtz configuration aligned along three orthogonal axes. An additional pair of coils in the anti-Helmholtz configuration is used for creating a quadrupole magnetic field during the magneto-optical trapping, as will be described below.

The experiment consists of several steps continuously following one another in a cycling manner. After the last step is completed, the cycle repeats itself. For the control and automation of the experimental parameters and steps, we use LabView software. The experimental steps are described below in their corresponding order.

The utilized laser-cooling techniques are introduced very briefly. More details on their working principles can be found in my M.Sc. thesis [80].

5.3.1 Magneto-optical trapping

The first step is the magneto-optical trapping, schematically shown in Figure 5.6(a). Here, the anti-Helmholtz coils create a quadrupole magnetic field with a node in the center of the cell. The exact position of the node is adjusted with three pairs of Helmholtz coils. The magneto-optical trap is created by three pairs of counter-propagating laser beams, referred to as the "cooling light," intersecting at the magnetic field's node. One pair is aligned along the field's axis of symmetry, and the other beams are lying in the perpendicular plane. All cooling beams are derived from the same laser and have the same frequency and approximately the same power. The idea is to set up the laser frequency and the polarization of each beam in such a way that the laser-atom interaction creates an effective potential well, confining atoms in the trap, and an effective viscous force, reducing the average kinetic energy of atoms in the trap.

Both trapping and dissipation effects happen simultaneously and originate from the imbalance in the number of photons scattered from the counter-propagating beams. To create an effective friction force, we want the atoms to scatter more photons from the laser beams traveling in the direction opposite to the atomic velocity. In order to achieve this, the laser frequency is red-detuned from $|F = 2\rangle \rightarrow |F' = 3\rangle$ transition of the D2-line. Due to the Doppler shift, the frequency of the oncoming beams is closer to the resonance in the atomic frame, resulting in a higher scattering rate. The resulting force vector is opposite to the atomic velocity, slowing the atoms down in a process known as the Doppler cooling.

To create a trapping potential, we want the laser beams to push the atoms towards their intersection, serving as the trap center. This spatial preference results from the presence of a quadrupole magnetic field, which shifts the atomic energy levels due to

the Zeeman effect. The sign and value of the shift for each Zeeman sublevel depend on the atom's location with respect to the field's node. The polarization for each beam is chosen in such a way that a combination of the Zeeman shift, which counterbalances the optical detuning, and the selection rules guarantee that the photon scattering rate is higher for the beams pushing the atoms towards the trap center.

During interaction with the cooling light, there is a finite excitation probability for the atoms to undergo off-resonant transition $|F = 2\rangle \rightarrow |F' = 2\rangle$, after which they can spontaneously decay to $|F = 1\rangle$. This results in optical pumping of the atoms to state $|F = 1\rangle$, in which they no longer interact with the cooling beams. To contentiously restore the population in $|F = 2\rangle$, a low-power "repump" beam resonant with $|F = 1\rangle \rightarrow |F' = 2\rangle$ is applied.

As a result of the magneto-optical trapping, an atomic cloud forms in the trap, which has a higher density and lower temperature compared to the rest of the vapor in the cell. The typical duration of this step in our experiment is $5 - 10$ seconds, resulting in the cloud with atom number on the order of 10^9 and the temperature on the order of 100 μK.

5.3.2 Optical molasses cooling

For the second step, we switch off the quadrupole field and sweep the cooling light frequency. It improves the efficiency of the Doppler cooling and adds an additional dissipation mechanism known as polarization-gradient cooling [114], which decreases the cloud's temperature down to 70 μK. In terms of the effect on the atomic motion, the region where the laser beams overlap act as a viscous medium, and is called the "optical molasses". Because there is no restoring force anymore, the atoms eventually diffuse out of the cooling region, so the typical duration of this step is relatively short, on the order of 10 ms. At the end of this stage, we turn off the repump light 1 ms before switching off the cooling beams to optically pump the atoms into $|F = 1\rangle$ state for the following microwave-optical double-resonance imaging. In our case, the typical

atom number after the optical molasses cooling is on the order of 10^8.

5.3.3 Double-resonance imaging

The final step of the experimental cycle is the interrogation of the atomic ensemble by a microwave magnetic field. The magnetic interaction effect on the atomic population is evaluated through the microwave-optical double-resonance imaging of state $|F = 2\rangle$. The imaging principle is the same as described in Chapter 3, except in this case, the atomic population starts in $|F = 1\rangle$. The population of $|F = 2\rangle$ is sampled with probe light resonant with $|F = 2\rangle \rightarrow |F' = 2\rangle$ transition, which is the transition typically used for absorption imaging in cold-atom experiments. Because the Doppler broadening effect in cold atoms is greatly reduced compared to the thermal vapor, we assume that, unlike in Section 3.5, the probe addresses only a single transition.

The microwave field is provided by SRS SG384 microwave source with built-in phase modulation connected to a wave-guide pointing at the cell, as is schematically shown in Figure 5.6(b). Before the wave-guide, the field goes through an external amplifier providing microwave power at the output of about 2 W. We keep the microwave field applied during the experiment and control the interaction by adjusting the microwave detuning. During the cooling stage, it is shifted 100 MHz away from the atomic resonance, so the field does not affect atomic states. During the magnetometry step, the microwave is mixed with a 100-MHz signal, so one of the produced side-bands is resonant with the atomic transition. A detailed description of the microwave setup can be found in the undergraduate report by Christian Prosko [110].

5.4 Experimental results

First, we demonstrate the double-resonance imaging in a laser-cooled atomic cloud as it expands after being released from the optical molasses. Figure 5.7(a) shows the transmitted probe power in the case when the microwave is on resonance, and no modulation is applied. In this case, we can observe a few Rabi oscillations before

the population reaches the steady-state, whose spectrum does not show any distinct oscillations. The steady-state signal shows a slight slope, which we will further investigate and discuss below. Figure 5.7(b) corresponds to the case of a strongly modulated field, whose carrier frequency is slightly off-resonance from the hyperfine transition. In agreement with the simulations, the observed signal shows consistently maintained oscillations at integer multiples of the modulation frequency. In Figure 5.7(c), we use the same microwave parameters, but the carrier is now on resonance. In this case, the odd harmonics in the spectrum are suppressed.

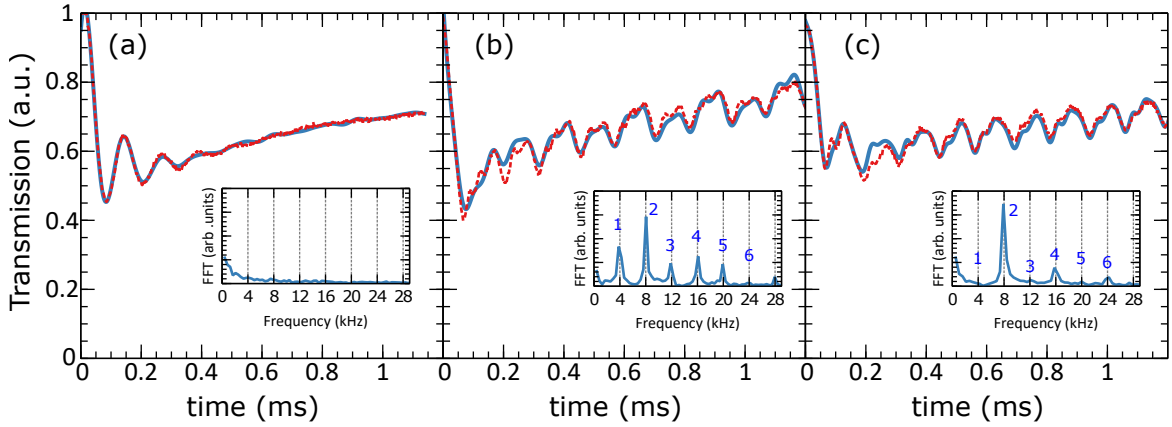

Figure 5.7: Transmission (blue curve) of a 46 μW probe in the double-resonance imaging of a laser-cooled atomic cloud released from the optical molasses. At $t = 0$ atomic population is in $F = 1$. For clarity, we show only the first 1.2 ms out of a total of 5 ms of expansion. The red dashed curve corresponds to the numerical fit. The insets show the Fast Fourier transform applied to the signal's tail, where the Rabi oscillations are damped out. Each spectral component is labeled with an integer number, corresponding to the harmonic of ω_{m}. In all insets, axes have the same scaling. (a) Unmodulated microwave field on resonance. (b) $\omega_{\mathrm{m}}/2\pi = 4$ kHz, $m = 2\pi$, $\delta/2\pi = 7$ kHz; (c) $\omega_{\mathrm{m}}/2\pi = 4$ kHz, $m = 2\pi$, $\delta \approx 0$. Figure adapted from [63].

To show that we can qualitatively interpret the observed signals as a response of a damped harmonic oscillator with natural frequency Ω_{R} driven at multiples of ω_{m}, we fit the data in Figure 5.7 with function

$$f(t) = \sqrt{A^2 + (Bt)^2} + C_1 e^{-\Gamma_1 t} + C_2 e^{-\Gamma_2 t} \sin^2\left(\frac{\Omega_R}{2}t + \phi\right) + \sum_{n=1}^{6} P_n \sin(n\omega_m t + \phi_n). \tag{5.16}$$

In this model, the first term takes into account the change in the cloud's density due to interaction with the probe, where A corresponds to the initial density and B corresponds to the hole-burning rate. The second and third terms describe the Rabi oscillations with longitudinal and transverse relaxation at rates Γ_1 and Γ_2, respectively, where parameters C_1 and C_2 are the proportionality coefficients between the level population and observed signal, and ϕ is the quadrature phase of the Rabi oscillations. The last terms describe oscillations at the harmonics of the modulation frequency, where P_n and ϕ_n are the steady-state amplitude and phase of the n^{th} harmonic. Based on the FFT spectrum, we keep only six harmonics in the fit.

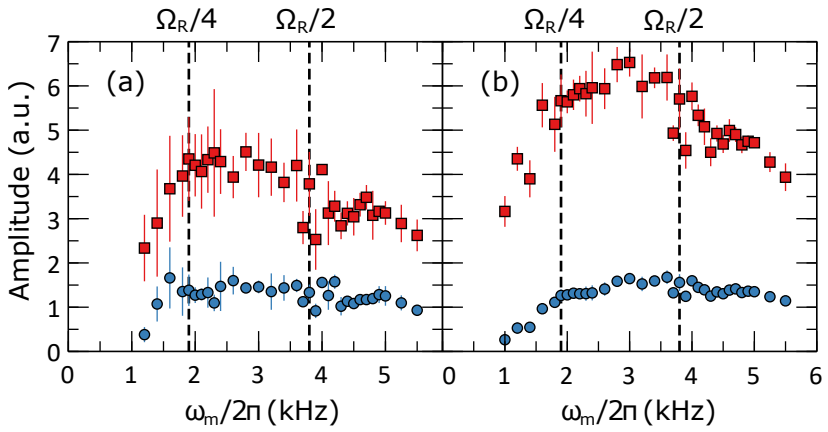

Figure 5.8: Rabi resonances for the amplitudes of the second (red squares) and fourth (blue circles) harmonics for $m = 2\pi$, $\delta \approx 0$, and the probe power of 46 μW. Each point and its error bar correspond to an average and variance of five values extracted from a tail of a double-resonance signal, respectively. The vertical dashed lines correspond to the modulation frequency values satisfying $2\omega_{\text{m}} = \Omega_{\text{R}}$ and $4\omega_{\text{m}} = \Omega_{\text{R}}$. The points were obtained by two numerical methods: (a) using numerical lock-in detection (Eqs. 5.11-5.13); (b) from fitting the observed signal to Eq. 5.16. Figure adapted from [63].

We would like to highlight the fact that the presented results correspond to a single experimental cycle. In general, there is a discrepancy in the observed spectra with the relative peaks' height varying among consecutive experimental cycles with the same parameters. We believe this is due to variations and noise in the radio-frequency mixer response, resulting in the variations in the value of the carrier-frequency detuning.

For the analysis of the Rabi resonances presented below, we use values of amplitudes averaged over several cycles.

To analyze the Rabi-resonance behavior of the second and fourth harmonics, we look at their amplitudes as we vary the modulation frequency at constant microwave and probe power. The results are shown in Figure 5.8, where we extracted the amplitudes using two numerical methods: Figure 5.8(a) shows the values found by the digital lock-in detection (Eqs. 5.11-5.12), Figure 5.8(b) shows the values found from the fit to Eq. 5.16. Both methods are in a qualitative agreement with each other, showing that the amplitudes of both harmonics peak as the modulation frequency is scanned through $\Omega_{\mathrm{R}}/2 = 2\pi \times (3.8 \pm 0.3)$ kHz, where Ω_{R} was determined from the data corresponding to the unmodulated field. The uncertainty in Ω_{R} corresponds to the variance of several data points and probably, in the same way as the uncertainties in the harmonics' amplitudes, originates from the variation of the radio-frequency mixer response time. From the fit of the unmodulated response, we extracted the relaxation rates as $\Gamma_1 = (2.0 \pm 0.1) \times 10\ \mathrm{s}^{-1}$ and $\Gamma_2 = (0.97 \pm 0.04) \times 10\ \mathrm{s}^{-1}$, which are on the same order of magnitude as Ω_{R} and ω_{m}, corresponding to the regime of high relaxation. Even though this regime is of no practical interest, the experimental observations seem to qualitatively agree with our simulations. The fact that the measured relaxation rates satisfy within uncertainty the relation $\Gamma_1 = 2\Gamma_2$ suggests that the transverse relaxation is a consequence of the longitudinal relaxation, and there is no additional inhomogeneous contribution.

To test whether the observed steady-state slope is due to thermal expansion or hole-burning by the probe, we perform the double-resonance imaging for several values of the probe power. Figure 5.9(a,b) shows that reducing the probe power from 0.54 μW down to 0.06 μW exterminates the slope, suggesting that it was caused by the probe. In addition, lower probe power results in a reduced relaxation rate allowing to observe more Rabi oscillations. This is a manifestation of a transition from overdamped to underdamped oscillations. Figure 5.9(c) provides results of a simulation

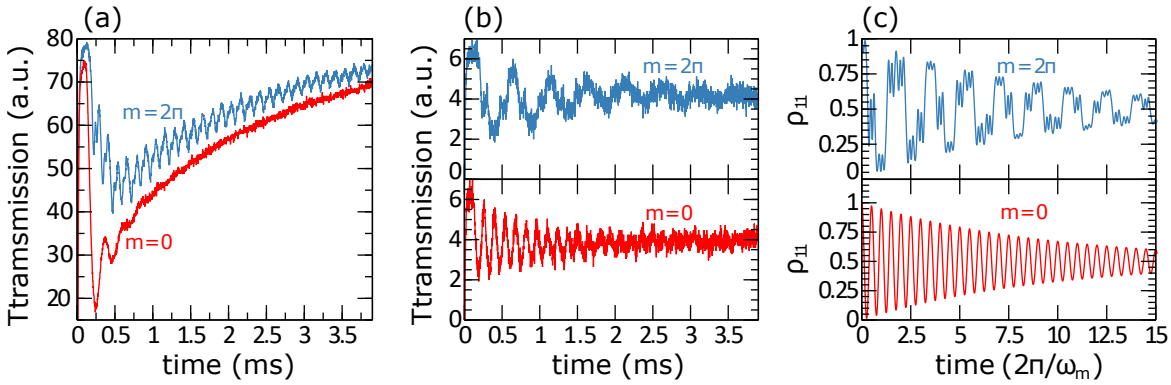

Figure 5.9: (a,b) recorded double-resonance signal for the probe power of (a) 0.54 μW, and (b) 0.06 μW, for the cases of a phase-modulated (red) and unmodulated (blue) microwave field. The microwave source power is 10 dBm, and the modulation frequency is $\omega_{\mathrm{m}}/2\pi = 4$ kHz. (c) Simulation of the two-level system response to a phase-modulated microwave field in the underdamped case corresponding to (b), with simulation parameters $\Omega_{\mathrm{R}} = 2\omega_{\mathrm{m}}$ and $\Gamma_1 = 2\Gamma_2 = 0.02\omega_{\mathrm{m}}$. Figure adapted from [63].

for the underdamped case, which shows a good qualitative agreement with the data in Figure 5.9(b). The simulation of the overdamped case was shown in Figures 5.2-5.3, where the theoretical model assumed a constant atomic density, so the simulated results do not show a steady-state slope.

The effect of the probe power on relaxation can be explained by optical pumping transferring the atomic population from $|2\rangle$ to $|1\rangle$, which is equivalent to a longitudinal relaxation in a two-level system. A similar effect was also observed in Ref. [41], where an increase in the optical probe power (meaning an increase in the optical pumping rate) leads to broadening of the Rabi resonance. Note that using a higher probe power has its benefits: it provides a significantly better signal-to-noise ratio, and the increased relaxation makes the system reach the steady-state faster, allowing to sample more steady-state oscillations. From a practical point of view, the optimal probe power will be determined as a trade-off between the aforementioned benefits and its hole-burning effect.

5.5 Conclusions

In conclusion, we investigated the behavior of a two-level system driven by phase-modulated coupling in the regimes where there is no analytical solution to the problem. Via numerical simulation, we demonstrated that the dynamic steady state consists of oscillations at multiples of the modulation frequency, with only even harmonics present when the carrier frequency is exactly on resonance with the two-level transition. The analysis of the amplitude of the fourth harmonic shows that it experiences two resonances as the modulation frequency is varied. At lower modulation depth and relaxation rates, the peaks are located at $\Omega_{\mathrm{R}} = 2\omega_{\mathrm{m}}$ and $\Omega_{\mathrm{R}} = 4\omega_{\mathrm{m}}$, but they experience a shift as the modulation depth is increased. The peak at $\Omega_{\mathrm{R}} = 4\omega_{\mathrm{m}}$ has a quartic dependence of its height on the modulation depth. Besides, it shows a smaller linewidth and shift compared to the second-harmonic resonance. All these facts combined suggest that the fourth-harmonic resonance might be a promising alternative for the atomic-candle applications and AC-magnetometry in systems with a weak absorption signal and limited interrogation time, such as cold atoms.

Experimentally, we performed contentious-wave measurements of the population transfer in a cold atomic ensemble due to interaction with a microwave magnetic field. In the case of a strongly phase-modulated microwave field, the observed spectrum of the steady-state oscillations contains multiple harmonics of the modulation frequency. To our knowledge, this is the first recorded observation double-resonance in cold atoms and the first observation of high-order harmonics in a phase-modulated double-resonance signal in an atomic vapor. The observed qualitative behavior of the harmonics is in agreement with our simulations.

All in all, our findings improved our understanding of the dynamics of a two-level system driven by a modulated field, and provided us with value insights that we used for the transduction experiments in Chapter 4.

Chapter 6

Microwave-controlled optical switching, and optical polarization rotation.

This chapter presents the results from our most recent project finished in summer 2020. This project started out as an attempt to modify the microwave-optical double-resonance scheme described in previous chapters for microwave-to-optical frequency conversion, i.e., an increase in the optical transmission due to applying a resonant microwave field. In the beginning, we experimentally realized the conversion in the double-resonance setup for an additional optical field in the form of microwave-controlled optical switching. Next, a closer theoretical evaluation of our approach showed that the level structure of ^{87}Rb offers an optical transition experiencing dichroism, which could make the optical switching polarization-selective. To describe this effect, we introduced a multi-level model going beyond the three-level approximation. In this new model, we discovered that in the non-degenerate case, combined microwave and optical coupling in the double-resonance arrangement leads to a transfer of atomic population between the Zeeman sublevels in the $F = 1$ ground state. With this effect, which we call microwave-assisted optical pumping, we propose a method of creating spin polarization or alignment in an atomic ensemble by addressing specific microwave-transitions. Finally, while trying to experimentally confirm the occurrence of the microwave-assisted optical pumping, we accidentally discovered op-

tical rotation that depends on the microwave frequency. To our knowledge, this is the first observation of the optical rotation induced by a microwave magnetic field, at least in an atomic vapor.

This chapter presents the concepts and results in a logical order. We begin by introducing the field of optical switching and magneto-optical rotation in the atomic vapors in Section 6.1. Next, we describe the principles of the microwave-assisted optical pumping in Section 6.3 and its implementation in a polarization-selective microwave-to-optical conversion in Section 6.2. In Section 6.4, we present our experimental results demonstrating the microwave-controlled optical switching and optical rotation.

6.1 Introduction

The experiment discussed in this chapter can be conceptually divided into two parts. In the first part, we show the applicability of the microwave-optical double resonance for optical switching and frequency conversion. In the context of this chapter, we will use the term "optical switching" to denote a process of controlled switching on and off the absorption of an optical field in a device, which we will call the optical switch. Atomic vapors offer a good platform for all-optical switching, where the control is implemented by applying additional optical fields. Typically, the all-optical switching in thermal atomic vapors is implemented using electromagnetically-induced transparency (EIT) in three-level [115] and multi-level [116] systems. Optical switching controlled by a single photon was demonstrated in cold atoms using Rydberg excitations [117–119] and cavity-enhanced EIT [120]. It was also demonstrated that the phase of a microwave magnetic field can be used as a control signal in an EIT-based optical switch [121], in which case the magnetic-dipole interaction with the microwave field interferes with the EIT established by two optical fields.

In the case when applying the control field leads to an increase in the probe transmission through the switch, the optical switching can be considered as a frequency-

conversion process: the control field at one frequency is converted to the probe field at another frequency. For example, the EIT-based optical switch from Ref. [115] is a frequency conversion between two optical fields. While the double-resonance effect considered in previous chapters can be used for optical switching, we do not consider it a frequency conversion because, in this case, applying a microwave field leads to absorption of the optical probe. Later in this chapter we will show that this effect is reversed for an additional optical field leading to the microwave-to-optical frequency conversion, which for a specific optical transition can be polarization-selective. We will also present a model of microwave-assisted optical pumping that shows potential for engineering macroscopic spin polarization of the atomic ensemble.

In the second part of the experiment, we demonstrate a magneto-optical rotation of an off-resonant laser field polarization induced by the microwave field in the extended double-resonance setup, with the angle of rotation depending on the microwave parameters. The magneto-optical rotation results from the circular birefringence due to the spin polarization in an atomic ensemble, and it is widely used in optical magnetometers [122–128] as a passive tool to non-destructively monitor the evolution of atomic spin-polarization created by optical pumping, which allows extracting parameters of the ambient static or slowly-varying magnetic field. In our setup, the magneto-optical rotation is used to control the optical polarization, bringing new prospects for microwave-to-optical transduction.

6.2 Microwave-to-optical transdcution via double resonance

Here we propose a microwave-controlled optical switch based on the microwave-optical double resonance in a thermal atomic vapor. Figure 6.1(a) illustrates the operation principle in terms of the same three-level system as we used to introduce the double-resonance in Section 3.1. Here, the switching is performed for the probe resonant with $|1\rangle \rightarrow |e\rangle$ transition. The population in $|1\rangle$ is controlled by a continuously running

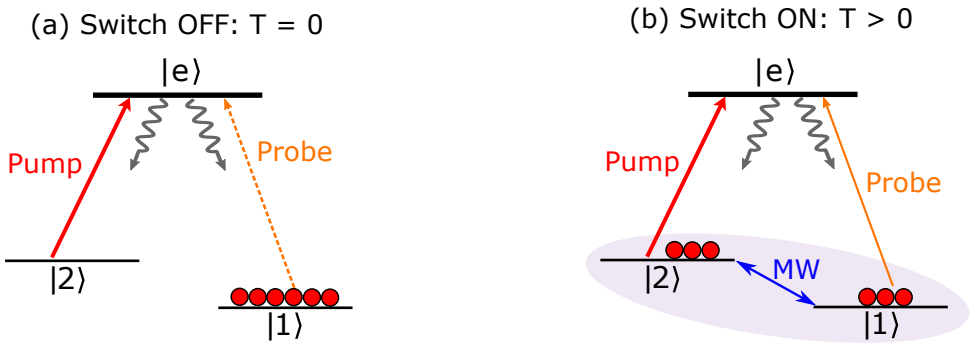

Figure 6.1: Schematics of the microwave-controlled optical switch in a three-level system. (a) With no microwave field the switch is in the OFF-state where the probe is fully absorbed. (b) Applying the microwave field reduces the steady-state population of $|1\rangle$ and puts the switch in the ON-state, where some of the probe is transmitted.

strong pump light resonant with $|2\rangle \rightarrow |e\rangle$ and a microwave field coupling $|1\rangle$ and $|2\rangle$, which acts as a control signal turning the switch on and off.

When the microwave field is not applied, all atomic population is optically pumped into $|1\rangle$. We assume that in this regime the vapor optical density is enough to fully absorb the probe, corresponding to the OFF-state of the switch. Applying the microwave field reduces the steady-state population of $|1\rangle$ enough to make the vapor transmit some of the probe power, corresponding to the ON-state of the switch. Unlike in the optical switching schemes based on electromagnetically-induced transparency, in our approach, the probe and pump do not have to form a closed λ-system and can address different excited states. On a single-photon level, the switch operation corresponds to the destruction of one microwave photon and the creation of one optical photon and thus can be considered microwave-to-optical frequency conversion.

The three-level model presented above can be applied to a ^{87}Rb atom when there are no external static fields, and the hyperfine levels are degenerate. In this case, states $|1\rangle$ and $|2\rangle$ correspond to the hyperfine ground states $|F = 1\rangle$ and $|F = 2\rangle$, respectively, and the microwave field couples to all Zeeman sublevels of $|F = 1\rangle$ at once. In a non-degenerate case, the microwave field can at most couple to two Zeeman sublevels of $|F = 1\rangle$, which leads to an accumulation of the atomic population in

the uncoupled sublevels via a process that we will call microwave-assisted optical pumping. Below we take a closer look at the process of microwave-assisted optical pumping and its possible applications.

6.3 Microwave-assisted optical pumping

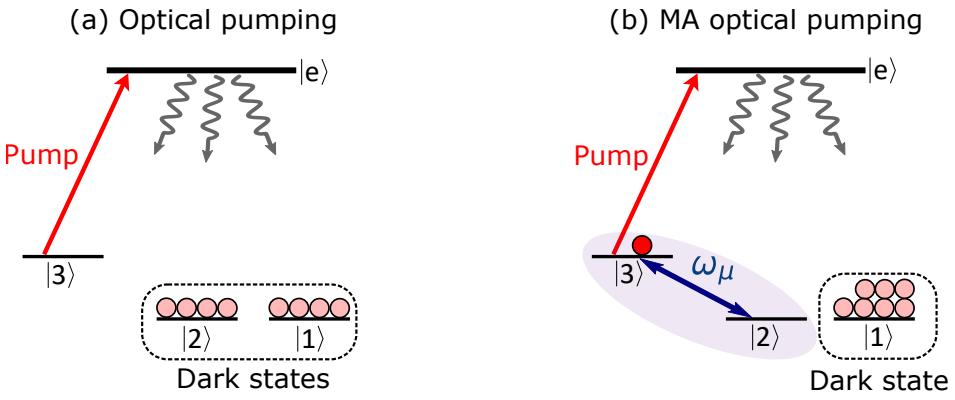

Figure 6.2: Principle of the optical pumping (a) and microwave-assisted (MA) optical pumping (b) in a four-level system.

To illustrate the principle of microwave-assisted optical pumping, we use a four-level toy model shown in Figure 6.2. In this model, $|e\rangle$ represents an excited state, and $|1\rangle$, $|2\rangle$, and $|3\rangle$ are the ground states. We assume that all three ground states can be coupled to $|e\rangle$ via an electric-dipole transition and that states $|2\rangle$ and $|3\rangle$ can be coupled to each other via a microwave magnetic-dipole transition. When the pump field drives the $|3\rangle \rightarrow |e\rangle$ transition, the atomic population accumulates in states $|2\rangle$ and $|1\rangle$ due to optical pumping [Figure 6.2(a)]. Note that we assume that the energy differences between state $|3\rangle$ and the other ground states are large enough, so that the optical field does not excite $|1\rangle$ and $|2\rangle$, making them dark states. When we simultaneously apply a microwave field that couples $|2\rangle$ and $|3\rangle$, state $|2\rangle$ is no longer a dark state for the combined microwave and optical electromagnetic field. As a result, the population of $|2\rangle$ undergoes the $|2\rangle \rightarrow |3\rangle \rightarrow |e\rangle$ transition, after which it spontaneously decays to any of three ground states. After several excitation-emission

cycles all atomic population is accumulated in the dark state $|1\rangle$, decoupled from the electromagnetic fields [see Figure 6.2(b)].

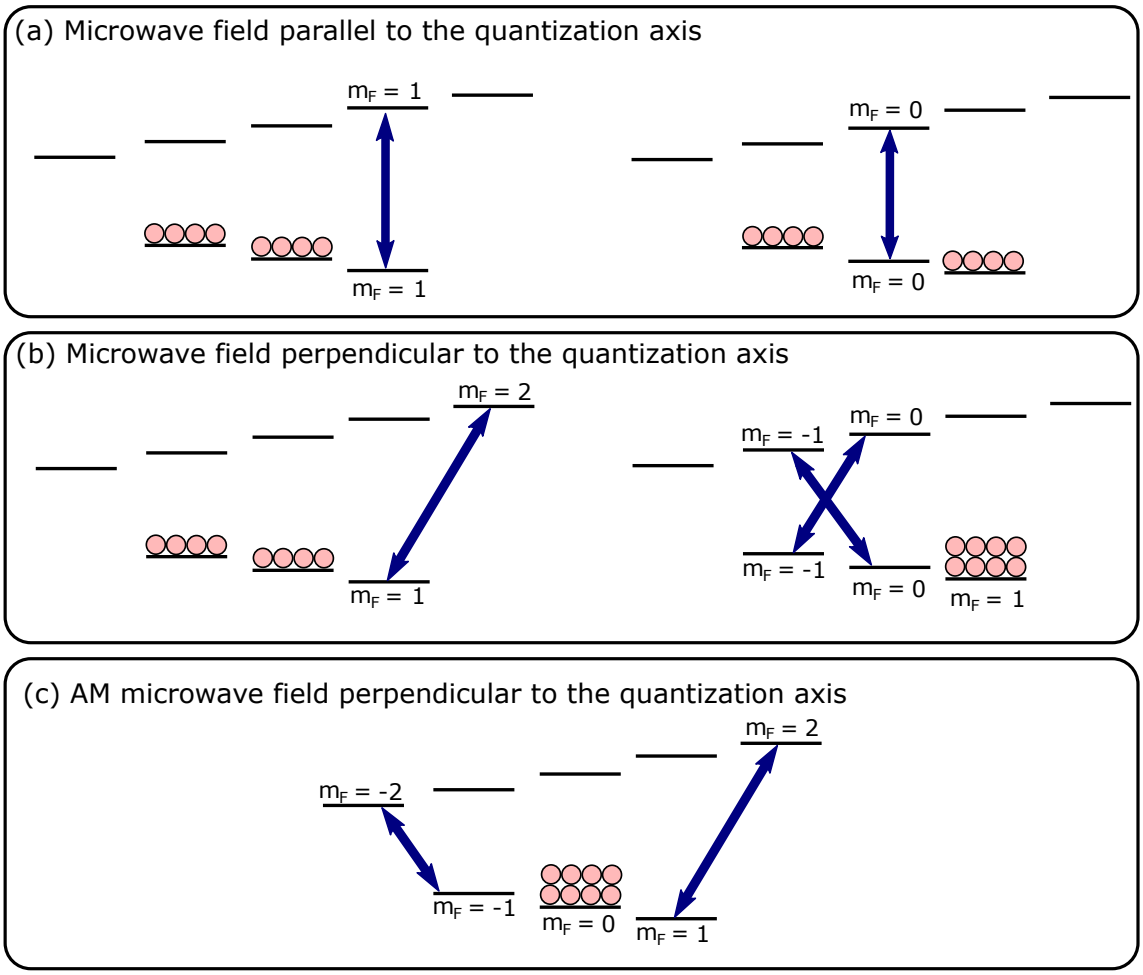

Figure 6.3: Possible population distributions between Zeeman sub-levels of level $F = 1$ which can be created by microwave-assisted optical pumping. All sub-levels of level $F = 2$ are assumed to be coupled to the optical field (not shown). (a) In the case when the microwave field vector is parallel to the quantization axis, we can selectively empty out a particular m_F-state by controlling the microwave frequency (the case of $|F = 1, m_F = -1\rangle$ is not shown). (b) Using a microwave field perpendicular to the quantization axis allows to empty out or fully occupy $|F = 1, m_F = \pm 1\rangle$-states (the case of $|F = 1, m_F = -1\rangle$ is not shown) depending on the microwave frequency. (c) If a microwave field perpendicular to the quantization axis is amplitude modulated at twice the Larmor frequency will empty out $|F = 1, m_F = -1\rangle$ and $|F = 1, m_F = 1\rangle$ states, without affecting $|F = 1, m_F = 0\rangle$.

In the case of ^{87}Rb, we have more than four levels, but the same principle ap-

plies, and the atomic population accumulates in the ground-state Zeeman sublevels uncoupled from the microwave field. Figure 6.3 shows possible population distributions between Zeeman sublevels of level $F = 1$, which can be created by microwave-assisted optical pumping, assuming that all sublevels of level $F = 2$ are coupled to the pump field[1]. By choosing the microwave frequency and polarization, we can fully occupy or clear particular Zeeman sublevels. This can be used to create spin-oriented states $|F = 1, m_F = \pm 1\rangle$, and a spin-aligned state, in which $|F = 1, m_F = 1\rangle$ and $|F = 1, m_F = -1\rangle$ are populated equally. Potentially, we can create atomic spin-polarization transverse to the quantization field by using an amplitude or frequency modulation of the microwave field to generate sidebands coupled to $|F = 1, m_F = 1\rangle \rightarrow |F = 1, m_F = 2\rangle$ and $|F = 1, m_F = -1\rangle \rightarrow |F = 1, m_F = -2\rangle$ [see Figure 6.3(c)]. In this case, the microwave field vector is perpendicular to the quantization axis, the carrier frequency is resonant with the clock transition, and the modulation frequency is twice the Larmor frequency. Due to the selection rules, the carrier wave does not drive the clock transition, and the atomic population should accumulate in the state $|F = 1, m_F = 0\rangle$.

Microwave-assisted optical pumping can make the microwave-to-optical frequency conversion polarization-selective, as is shown in Figure 6.4. Here, the probe is tuned to the $|F = 1\rangle \rightarrow |F = 0\rangle$ transition in ^{87}Rb. Because level $|F' = 0\rangle$ has only one Zeeman state $m_F = 0$, each Zeeman sublevel of $|F = 1\rangle$ can absorb only a single component of the probe polarization, as is determined by the selection rules [see Figure 6.4(a)]. We assume that the optical density of the vapor is enough to fully absorb each polarization component. Selectively clearing out a particular Zeeman sublevel via microwave-assisted optical pumping will make the vapor transparent to the corresponding polarization component [see Figure 6.4(a)]. Note that the redistributed population makes the vapor even more opaque for the other polarization

[1]This assumption is valid since the linewidth of the D2-line is larger than the typical Zeeman spitting in our experiments.

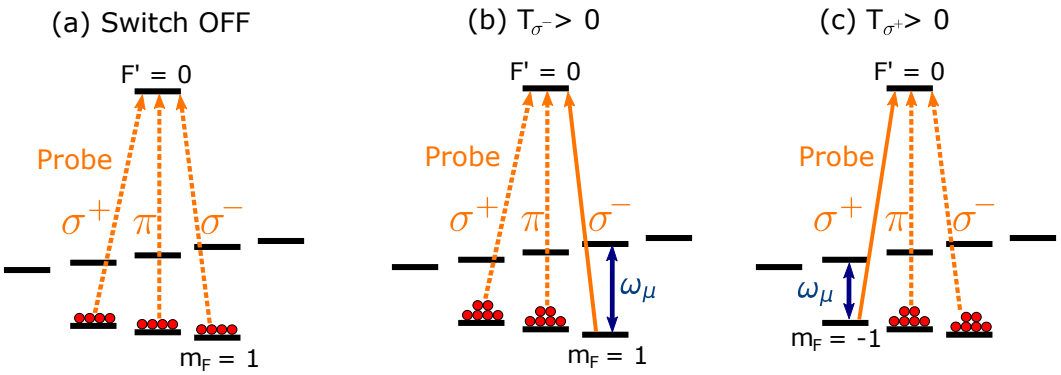

Figure 6.4: Polarization-selective microwave-controlled optical switch in $|F = 1\rangle$ state of ^{87}Rb. Optical pump is not shown. Solid and dashed arrows represent transmitted and absorbed component, respectively. (a) With no microwave field, the atomic population is distributed equally between the Zeeman sublevels, fully absorbing all three polarization components of the probe resonant with $|F = 1 \rightarrow |F = 0\rangle\rangle$. (b) Driving the $|F = 1, m_F = 1\rangle \rightarrow |F = 2, m_F = 1\rangle$ transition, make the vapor transparent for σ^--polarization component of the probe. (c) Driving the $|F = 1, m_F = -1\rangle \rightarrow |F = 2, m_F = -1\rangle$ transition, make the vapor transparent for σ^+-polarization component of the probe.

components. Thus, with this approach, the atomic vapor can act as an optical switch for a particular probe polarization while blocking other polarization components. In addition, modulating the microwave frequency between different hyperfine transition should lead to the modulation of the transmitted probe polarization: e.g, switching the microwave frequency between the $|F = 1, m_F = -1\rangle \rightarrow |F = 2, m_F = -1\rangle$ and $|F = 1, m_F = 1\rangle \rightarrow |F = 2, m_F = 1\rangle$ transitions will modulate the transmitted probe polarization between σ^+ and σ^-, respectively.

In thermal vapors, thermal motion (Section 2.4.3), inter-atomic collisions, and collisions with the cell wall can lead to significant spin relaxation. In this case, microwave-assisted optical pumping does not transfer the whole atomic population to the dark state and does not completely clear out the coupled states. Nevertheless, the steady-state population of the dark state is larger than that of the coupled states, leading to some observable effects, as we will show in the next section.

6.4 Experiment

6.4.1 Setup

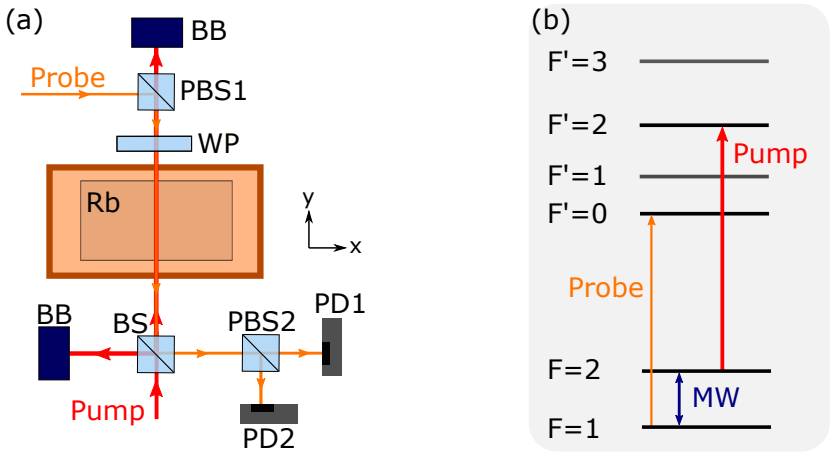

Figure 6.5: (a) Schematics of the optical setup. The labels are described in the main text. x and y axes indicate the horizontal plane. The vacuum system is not shown. (b) Optical transitions used in the experiment.

For the experimental demonstration of the microwave-to-optical frequency conversion we use the same warm-atom system as in Chapters 3 and 4. The setup schematics is shown in Figure 6.5(a). Inside the cell, the probe and pump beam are counter-propagating. To overlap the two beams on one side of the cavity and to separate them on the other side, we use a polarization beam splitter (labeled as PBS1) and a 50/50 beam splitter (labeled as BS). Before PBS1, the probe is polarized vertically (perpendicular to the horizontal plane indicated by x and y axes), so PBS1 reflects the full probe power. After that, the probe goes through a wave plate (labeled as WP), which is either a quarter-wave plate or a half-wave plate. The wave plate allows us to control the probe polarization inside the cell. After the cell, the 50/50 beam splitter reflects half of the probe power, which is now separate from the pump beam. We use this type of beam splitter to preserve the probe polarization. A second polarizing beam splitter (PBS2) splits the vertical and horizontal polarization-components of the reflected probe between two photodetectors (PD1 and PD2). Both photode-

tectors are from Thorlabs, model PDA36A. As in Chapters 3 and 4, we monitor and record only the AC part of the photodetectors' signal on the oscilloscope (not shown). To terminate the stray beams coming out of the beam splitters, we use beam blockers (labeled as BB). Three pairs of coils (not shown) in Helmholtz configuration allow us to control the static magnetic field inside the cell. Figure 6.5(b) shows the atomic transitions for the pump and probe fields. For the probe we use a weak beam resonant with $|F = 1\rangle \rightarrow |F' = 0\rangle$ transition. Its typical power is $10 - 100$ μW. For the optical pumping we use $|F = 2\rangle \rightarrow |F' = 2\rangle$ transition with typical power of $1 - 2$ mW.

6.4.2 Frequency conversion

We begin with proof-of-principle measurements of microwave-to-optical frequency conversion of a circularly-polarized probe. Figure 6.6(a) shows the photo-detection signals as the microwave frequency is linearly swept through the hyperfine resonance in the case when the static magnetic field in the cell is aligned with the probe beam. In contrast with the double-resonance measurements from Chapter 3, here, the optical transmission is *increased* whenever the microwave field is on resonance with a hyperfine transition, which is a manifestation of the frequency conversion introduced in Section 6.2. Because the microwave magnetic field is perpendicular to the static field, only four peaks are observed. The observed feature is asymmetric with respect to the clock transition frequency, and the asymmetry is reversed if we reverse the direction of the static field (not shown). We believe this may be evidence of the uneven distribution of the atomic population between the Zeeman sublevels shown in Figure 6.6(b). Because the probe is σ^+-polarized, it can be absorbed only by atoms in level $|F = 1, m_F = -1\rangle$, whose population is lowered when the microwave detuning is negative and increased when the detuning is positive. When the magnetic field direction is reversed, the probe becomes σ^--polarized with respect to the magnetic-field vector and can couple only to $|F = 1, m_F = 1\rangle$ state, so the observed absorption pattern is reversed (not shown).

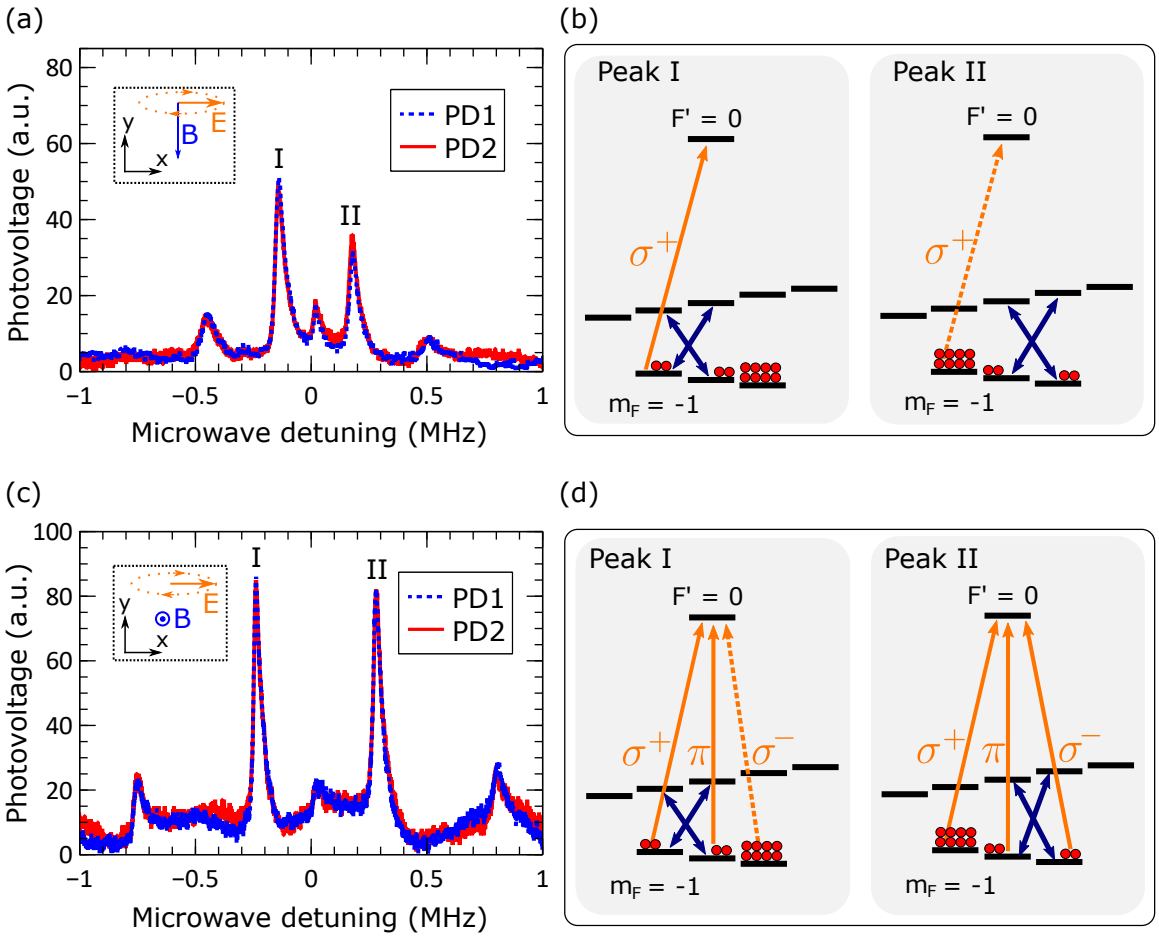

Figure 6.6: (a) Optical signal during a microwave frequency scan detected by PD1 and PD2 for circularly polarized probe in case when the static magnetic field **B** is parallel to the probe beam. Inset shown the orientation of the static magnetic-field vector and the polarization of the probe electric-field vector **E** with respect to x and y axes from Figure 6.5(a). The probe polarization lies in the xz plane. The microwave detuning is given with respect to the clock transition. (b) Schematics of the microwave (blue arrows) and probe (yellow arrow) transitions, and the expected relative distribution of the atomic population between Zeeman substates corresponding to peaks I and II from (a). The probe polarization is indicated with respect to the static magnetic field. The pump is not shown. (c) and (d) are same as (a) and (b), except the static magnetic field is perpendicular to xy-plane. Signals in (a) and (c) are shown on the same scale. Microwave source power output is -10 dBm. The frequency sweeping rate is 35.5 Hz.

Figure 6.6(c) shows the same measurement in the case when the static field is applied vertically. Figure 6.6(d) shows the atomic population distribution and optical

transitions if the quantization axis is chosen along the direction of the static field. In this case, the linear electric-field component of the probe that is parallel to x drives $\sigma^{\pm}$-transitions, while the vertical component drives the π-transition. This population distribution is symmetric in terms of the microwave detuning, so the observed signal is also symmetric. Because the probe couples to all three transitions, the observed signal is stronger than when the magnetic field is parallel to the probe.

Even though the measurements shown in Figure 6.6 support our model of microwave-to-optical frequency conversion, the signal shown in Figure 6.6(a) does not fully match our expectations for microwave-assisted optical pumping. If the atomic distribution shown in Figure 6.6(b) is correct, we would not expect to observe peak II at all or even see a decrease in optical transmission compared to the transmission level corresponding to the off-resonant microwave field, since the population transfer to $|F = 1, m_F = -1\rangle$ resulted from the microwave-assisted optical pumping should provide a higher optical density for σ^+-polarized probe compared to the off-resonant case. A possible reason for the observed discrepancy is a misalignment of the probe wave-vector and the magnetic-field vector, in which case the probe polarization with respect to the quantization axis is not fully circular. In addition, a significant part of the optical signal might be arising from the velocity classes resonant with $F = 1 \rightarrow F' = 1$ and $F = 1 \rightarrow F' = 2$ transitions, for which all Zeeman sublevels of $|F = 1\rangle$ will couple to the probe and contribute to the absorption. To further test that the microwave field creates asymmetric population distribution, in the next section, we look at the optical rotation.

6.4.3 Microwave-controlled optical rotation

The optical absorption in a medium is interconnected with dispersion - the frequency dependence of the phase-velocity of light in the medium, which is characterized by the refractive index. The fact that the microwave field in the above setup affects the optical absorption suggests that it also has an effect on the dispersion. We use

this effect to demonstrate that the microwave-assisted optical pumping creates an uneven population distribution between Zeeman levels, which results in a circular birefringence of the atomic vapor and an optical rotation of the probe polarization.

To observe the optical rotation, we use the same setup as for the absorption measurements in Figure 6.6(a), except now the probe is linearly polarized and its frequency is far red-detuned from $|F = 1\rangle \rightarrow |F = 0\rangle$ transition, where its absorption is reduced and the dispersion is enhanced. In this setup the probe frequency is not locked, and we set it by hand to the lower-frequency edge of the Doppler-broadened absorption peak of the D2-line originating in the $F = 1$ level. With a half-wave plate, we set the probe polarization at 45 degrees with respect to the x-axis (-45 degrees with respect to the z-axis), in which case PBS2 splits the probe power equally between the two photodetectors. In this setup, the optical rotation will result in opposite changes in the photo-voltage of the two detectors without affecting the total optical power.

To explain the origin of the optical rotation, we choose the quantization axis along the static magnetic field, which is parallel to the probe beam. With respect to this axis, the probe electric-field vector is in equal superposition σ^+- and σ^--polarized fields, which couple only to $|F = 1, m_F = -1\rangle$ and $|F = 1, m_F = 1\rangle$ states, respectively. Assuming that the single-atom refraction index is the same for each transition, the ensemble refractive index for each transition is proportional to the population at the corresponding level. As a result, the phase difference between the two polarizations leaving the ensemble is given by

$$\Delta\phi = kL(n_{\sigma^+} - n_{\sigma^-}) = kLn[N(m_F = -1) - N(m_F = 1)], \tag{6.1}$$

where k is the wavenumber, L and the distance that the light travels in the medium, n is the single-atom refraction index, and $N(m_F = -1)$ and $N(m_F = 1)$ are the numbers of atoms in states $|F = 1, m_F = -1\rangle$ and $|F = 1, m_F = 1\rangle$ states, respectively. This phase difference determines the angle by which the linear optical polarization is

rotated. While at thermal equilibrium atomic vapors are isotropic and thus do not show any birefringence, here, the population difference in states $|F = 1, m_F = -1\rangle$ and $|F = 1, m_F = 1\rangle$ corresponds to macroscopic spin polarization of the vapor, making it anisotropic.

The optical rotation due to spin polarization of atomic vapor discussed above corresponds to paramagnetic Faraday rotation [129], which is different from the diamagnetic Faraday rotation, where the optical rotation angle is proportional to the magnitude of a strong static magnetic field applied parallel to the optical beam [130]. In the case of diamagnetic Faraday rotation, transitions corresponding to different circular polarization experience different frequency shifts due to the interaction with the static magnetic field leading to the circular birefringence. In atomic vapors, both effects are typically referred to as Faraday rotation without specifying the type.

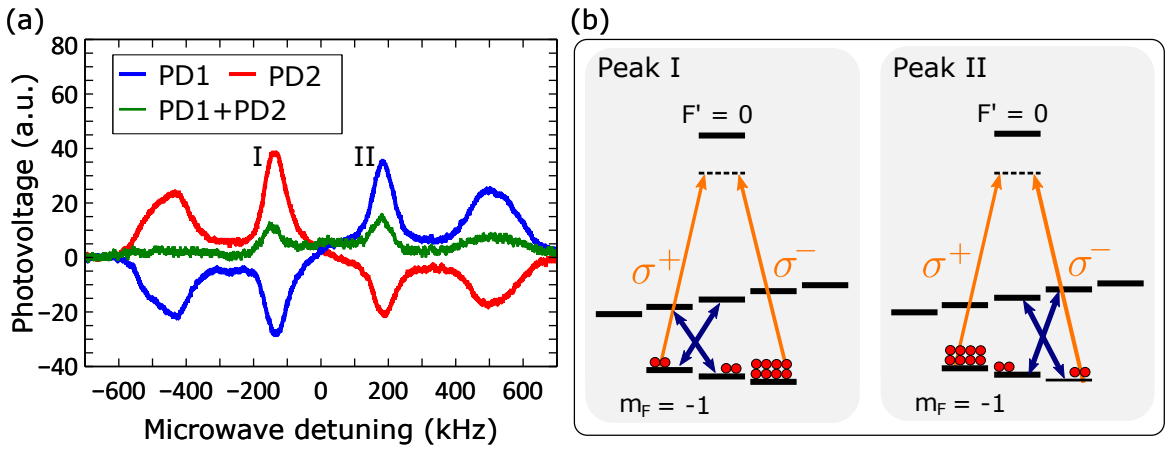

Figure 6.7: (a) Optical rotation during the microwave frequency scan detected as a change in the photovoltage on detectors PD1 and PD2. The green curve corresponds to the sum of the two voltages. Microwave detuning is given with respect to the clock transition. The microwave source is set to -10 dBm, the microwave frequency is scanned at a rate of 35 Hz. The estimated optical rotation angle corresponding to peak I is around 0.025 mrad. (b) Schematics of the microwave (blue arrows) and probe (yellow arrow) transitions, and the expected relative distribution of the atomic population between Zeeman substates corresponding to peaks I and II from (a). The pump is not shown.

Figure 6.7(a) shows the AC parts of the photovoltage from PD1 and PD2 during

the microwave frequency sweep. Whenever the microwave field is on resonance with an allowed hyperfine transition, it results in a positive voltage change from one detector and a negative change from the other, indicating the optical rotation. The sum of the two voltages is not exactly zero and corresponds to the part of the signal coming from frequency conversion. The fact that the signal from each detector is antisymmetric with respect to the clock-transition frequency means that the direction of the polarization rotation depends on the sign of the microwave detuning. According to Eq. 6.1, this is a consequence of a change in the sign of the difference in populations of levels $|F = 1, m_F = -1\rangle$ and $|F = 1, m_F = 1\rangle$. Figure 6.7(b) schematically shows the population distribution for peaks I and II. Due to a higher population of $|F = 1, m_F = +1\rangle$ in the case of peak I, σ^--polarization component experiences larger a refractive index and acquires a phase delay relative to the σ^+-polarization component, so the linear polarization rotates towards the horizontal axis, and more optical power goes to PD2. If we turn off the pump light or set its frequency off-resonance, the observed signal feature disappears, which suggests that the observed circular birefringence of the vapor results from the optical pumping by the pump light and not from the non-linear interaction with the probe itself.

6.5 Conclusions and outlook

We have demonstrated proof-of-principle microwave-to-optical frequency conversion based on optical switching in a double-resonance arrangement. For practical applications, the switching should provide a good signal contrast between ON and OFF regimes, which requires a high optical density for the probe beam. The optical density can be improved by increasing the atomic density in the cell and by increasing the length of the geometrical path that the probe travels in the cell. To improve the atomic density, we are replacing the current cell with a sealed vapor cell filled with enriched ^{87}Rb. To increase the path length covered by the probe inside the vapor cell, the probe can be sent along the cell axis rather than across. This approach would

require a different cavity design that provides optical access through the cavity faces.

In addition, we proposed a technique of microwave-assisted optical pumping that can be used for engineering spin polarization in atomic vapors leading to optical dichroism and birefringence. We provided experimental evidence for circular dichroism for light resonant with $|F = 1 \rightarrow F' = 0\rangle$ transition and circular birefringence for light red-detuned from the D2-line. The optical dichroism can be potentially used for polarization-selective optical switching and microwave-to-optical frequency conversion. The birefringence leads to the optical rotation, allowing us to manipulate the probe polarization by varying parameters of the microwave field. To our knowledge, this is the first demonstration of microwave control of optical rotation, at least in atomic vapors, and the first discussion of the phenomenon of microwave-assisted optical pumping. The microwave-controlled optical rotation can be used for optical switching based on polarization rotation [131] and pulse carving [132]. With the principles of microwave-to-optical transduction for radio-over-fiber applications developed in Chapter 4, we can also use this effect to encode a signal in the optical polarization angle, e.g., in the microwave-to-telecom transducer proposed in Section 4.7.

We believe that the results discussed in this chapter add a valuable contribution to the toolbox for atomic microwave-optical interfaces for information and communication technologies.

Chapter 7

Conclusions and future directions

In this thesis, we presented our results on realizing various types of microwave-to-optical transduction in rubidium vapor. In our transduction approach, we build upon the non-linear interaction between optical electric field and microwave magnetic field in a double-resonance setup.

In Chapter 3, we showed that the cavity-based approach provides a simple yet efficient method for enhancing the magnetic-dipole coupling between the microwave field and the atomic magnetic moment and demonstrated a rigorous experimental study of the double resonance in a thermal rubidium vapor inside a microwave cavity.

In Chapter 4, we introduced a novel method of transducing an audio signal from a frequency- and amplitude-modulated microwave field to optical intensity. With a proof-of-principle experiment, we demonstrated that the method is ready for radio-over-fiber communications. In addition, we proposed an atom-based microwave-to-telecom transducer relying on similar principles.

In Chapter 5, we presented our numerical and experimental study of quantum dynamics of a two-level system driven by a microwave field with harmonic phase modulation at arbitrary modulation depth. We hope that our results made a valuable contribution towards the continuing investigation of fundamental and applied aspects of quantum system dynamics [133].

In Chapter 6, we proposed and realized a novel method for microwave-to-optical

frequency conversion in atomic vapors based on optical switching controlled by a microwave field. We also proposed a scheme for microwave-assisted optical pumping, which can be used for creating and manipulating the spin polarization of an atomic ensemble. Through measurements of the optical dichroism and birefringence, we experimentally demonstrated that the spin polarization created with this method depends on the microwave frequency, which can be used for polarization-selective microwave-to-optical frequency conversion and microwave control of optical polarization.

For each project, we included possible extensions and spin-off applications at the end of the corresponding chapter. So far, all our transduction results are of semi-classical nature, with the transduction is realized between classical field via quantum dynamics in atomic vapor, so the general direction for all projects is to move towards quantized fields, particularly expanding the proposed transduction methods for a single-photon operation. This would require a thorough theoretical investigation of the quantum aspects of the proposed transduction mechanism and consideration of alternative experimental designs.

One of the important aspects of transduction that we did not look at in detail is the spin relaxation in the atomic vapor and the limitations it imposes on the transduction efficiency. This can be approached by using the buffer gas capabilities that our warm-atom apparatus offers to look at how the buffer gas type and pressure affect relaxation and transduction. For this purpose, the system needs to be provided with better vacuum sealing and to be upgraded to incorporate a pressure gauge measuring the total pressure inside.

Currently, our group is working on designing portable transducers based on vapor cells coupled to microwave resonators. One approach is to use a sealed vapor cell supported inside a microwave cavity by a dielectric material. In this project, Myles Ruether has been analyzing how the support's shape and dielectric properties affect cavity resonance. Another approach is to use microfabricated vapor cells, which are

currently studied and developed by Brittany Lu.

To move towards quantum transduction, together with the Davis lab we are currently building a hybrid system that will integrate cold atoms and cryogenically-cooled microwave devices. The work on the cold-atom apparatus for this system was started by Michelle Sullivan and is currently lead by Taras Hrushevskyi.

All in all, we believe our results make a valuable contribution to the growing library of novel devices and methods for microwave-to-optical transduction being developed at the University of Alberta and worldwide. These technologies will advance the field of classical and quantum information and communications by providing a platform for interfacing microwave-frequency qubits with optical photons. Such interface will allow long-distance transfer of quantum information between separated microwave-frequency qubits and integrating microwave and optical quantum information protocols.

Bibliography

[1] A. Montanaro, "Quantum algorithms: an overview," *npj Quantum Information*, vol. 2, no. 1, p. 15 023, 2016. DOI: 10.1038/npjqi.2015.23.

[2] A. Matsuura, S. Johri, and J. Hogaboam, "A systems perspective of quantum computing," *Physics Today*, vol. 72, no. 3, pp. 40–46, 2019. DOI: 10.1063/PT.3.4163.

[3] N. Gisin, G. Ribordy, W. Tittel, and H. Zbinden, "Quantum cryptography," *Rev. Mod. Phys.*, vol. 74, pp. 145–195, 1 2002. DOI: 10.1103/RevModPhys.74.145.

[4] J. C. Bardin, D. H. Slichter, and D. J. Reilly, "Microwaves in quantum computing," *IEEE Journal of Microwaves*, vol. 1, no. 1, pp. 403–427, 2021. DOI: 10.1109/JMW.2020.3034071.

[5] J. Q. You and F. Nori, "Superconducting Circuits and Quantum Information," *Physics Today*, vol. 58, no. 11, pp. 42–47, 2005. DOI: 10.1063/1.2155757.

[6] P. Krantz, M. Kjaergaard, F. Yan, T. P. Orlando, S. Gustavsson, and W. D. Oliver, "A quantum engineer's guide to superconducting qubits," *Applied Physics Reviews*, vol. 6, no. 2, p. 21 318, 2019. DOI: 10.1063/1.5089550.

[7] J. Wrachtrup and F. Jelezko, "Processing quantum information in diamond," *Journal of Physics: Condensed Matter*, vol. 18, no. 21, S807–S824, 2006. DOI: 10.1088/0953-8984/18/21/S08.

[8] F. A. Zwanenburg, A. S. Dzurak, A. Morello, M. Y. Simmons, L. C. L. Hollenberg, G. Klimeck, S. Rogge, S. N. Coppersmith, and M. A. Eriksson, "Silicon quantum electronics," 2013. DOI: 10.1103/RevModPhys.85.961.

[9] A Omran, H Levine, A Keesling, G Semeghini, T. T. Wang, S Ebadi, H Bernien, A. S. Zibrov, H Pichler, S Choi, J Cui, M Rossignolo, P Rembold, S Montangero, T Calarco, M Endres, M Greiner, V Vuletić, and M. D. Lukin, "Generation and manipulation of Schrödinger cat states in Rydberg atom arrays," *Science*, vol. 365, no. 6453, pp. 570–574, 2019. DOI: 10.1126/science.aax9743.

[10] L. Henriet, L. Beguin, A. Signoles, T. Lahaye, A. Browaeys, G. O. Reymond, and C. Jurczak, "Quantum computing with neutral atoms," *Quantum*, vol. 4, p. 327, 2020. DOI: 10.22331/Q-2020-09-21-327.

[11] M Morgado and S Whitlock, "Quantum simulation and computing with Rydberg qubits," 2020. arXiv: 2011.03031.

[12] C. S. Adams, J. D. Pritchard, and J. P. Shaffer, "Rydberg atom quantum technologies," *Journal of Physics B: Atomic, Molecular and Optical Physics*, vol. 53, no. 1, p. 012 002, 2020. DOI: 10.1088/1361-6455/ab52ef.

[13] C. D. Bruzewicz, J. Chiaverini, R. McConnell, and J. M. Sage, "Trapped-ion quantum computing: Progress and challenges," *Applied Physics Reviews*, vol. 6, no. 2, p. 021 314, 2019. DOI: 10.1063/1.5088164.

[14] R. Valivarthi, M. G. Puigibert, Q. Zhou, G. H. Aguilar, V. B. Verma, F. Marsili, M. D. Shaw, S. W. Nam, D. Oblak, and W. Tittel, "Quantum teleportation across a metropolitan fibre network," *Nature Photonics*, vol. 10, no. 10, pp. 676–680, 2016. DOI: 10.1038/nphoton.2016.180.

[15] J.-G. Ren, P. Xu, H.-L. Yong, L. Zhang, S.-K. Liao, J. Yin, W.-Y. Liu, W.-Q. Cai, M. Yang, L. Li, K.-X. Yang, X. Han, Y.-Q. Yao, J. Li, H.-Y. Wu, S. Wan, L. Liu, D.-Q. Liu, Y.-W. Kuang, Z.-P. He, P. Shang, C. Guo, R.-H. Zheng, K. Tian, Z.-C. Zhu, N.-L. Liu, C.-Y. Lu, R. Shu, Y.-A. Chen, C.-Z. Peng, J.-Y. Wang, and J.-W. Pan, "Ground-to-satellite quantum teleportation," *Nature*, vol. 549, no. 7670, pp. 70–73, 2017. DOI: 10.1038/nature23675.

[16] V. Krutyanskiy, M. Meraner, J. Schupp, V. Krcmarsky, H. Hainzer, and B. P. Lanyon, "Light-matter entanglement over 50 km of optical fibre," *npj Quantum Information*, vol. 5, no. 1, p. 72, 2019. DOI: 10.1038/s41534-019-0186-3.

[17] T. E. Northup and R. Blatt, "Quantum information transfer using photons," *Nature Photonics*, vol. 8, no. 5, pp. 356–363, 2014. DOI: 10.1038/nphoton.2014.53.

[18] R. W. Andrews, R. W. Peterson, T. P. Purdy, K. Cicak, R. W. Simmonds, C. A. Regal, and K. W. Lehnert, "Bidirectional and efficient conversion between microwave and optical light," *Nature Physics*, vol. 10, no. 4, pp. 321–326, 2014. DOI: 10.1038/nphys2911.

[19] M. Rudd, P. Kim, C. Potts, C. Doolin, H. Ramp, B. Hauer, and J. Davis, "Coherent Magneto-optomechanical Signal Transduction and Long-Distance Phase-Shift Keying," *Physical Review Applied*, vol. 12, no. 3, p. 034 042, 2019. DOI: 10.1103/PhysRevApplied.12.034042.

[20] H. Ramp, T. J. Clark, B. D. Hauer, C. Doolin, K. C. Balram, K. Srinivasan, and J. P. Davis, "Wavelength transduction from a 3D microwave cavity to telecom using piezoelectric optomechanical crystals," *Applied Physics Letters*, vol. 116, no. 17, p. 174 005, 2020. DOI: 10.1063/5.0002160.

[21] X. Fernandez-Gonzalvo, Y. H. Chen, C. Yin, S. Rogge, and J. J. Longdell, "Coherent frequency up-conversion of microwaves to the optical telecommunications band in an Er:YSO crystal," *Physical Review A - Atomic, Molecular, and Optical Physics*, vol. 92, no. 6, p. 62 313, 2015. DOI: 10.1103/PhysRevA.92.062313.

[22] X. Fernandez-Gonzalvo, S. P. Horvath, Y. H. Chen, and J. J. Longdell, "Cavity-enhanced Raman heterodyne spectroscopy in Er3+: Y2SiO5 for microwave to optical signal conversion," *Physical Review A*, vol. 100, no. 3, p. 033 807, 2019. DOI: 10.1103/PhysRevA.100.033807.

[23] C. Li and P. Cappellaro, "Telecom photon interface of solid-state quantum nodes," *Journal of Physics Communications*, vol. 3, no. 9, p. 095 016, 2019. DOI: 10.1088/2399-6528/ab4430.

[24] J. G. Bartholomew, J. Rochman, T. Xie, J. M. Kindem, A. Ruskuc, I. Craiciu, M. Lei, and A. Faraon, "On-chip coherent microwave-to-optical transduction mediated by ytterbium in YVO4," *Nature Communications*, vol. 11, no. 1, p. 3266, 2020. DOI: 10.1038/s41467-020-16996-x.

[25] M. C. Collodo, J. M. Fink, D. V. Strekalov, H. G. L. Schwefel, A. Rueda, C. Marquardt, G. Leuchs, U. Vogl, B. Stiller, G. Schunk, F. Sedlmeir, and O. Painter, "Efficient microwave to optical photon conversion: an electro-optical realization," *Optica*, vol. 3, no. 6, p. 597, 2016. DOI: 10.1364/optica.3.000597.

[26] J. D. Witmer, T. P. McKenna, P. Arrangoiz-Arriola, R. Van Laer, E. Alex Wollack, F. Lin, A. K. Jen, J. Luo, and A. H. Safavi-Naeini, "A silicon-organic hybrid platform for quantum microwave-to-optical transduction," vol. 5, no. 3, p. 034 004, 2020. DOI: 10.1088/2058-9565/ab7eed.

[27] X. Zhang, C.-L. Zou, L. Jiang, and H. X. Tang, "Strongly Coupled Magnons and Cavity Microwave Photons," *Physical Review Letters*, vol. 113, no. 15, p. 156 401, 2014. DOI: 10.1103/PhysRevLett.113.156401.

[28] F. Vewinger, J. Appel, E. Figueroa, and A. I. Lvovsky, "Adiabatic frequency conversion of optical information in atomic vapor," *Optics Letters*, vol. 32, no. 19, p. 2771, 2007. DOI: 10.1364/OL.32.002771.

[29] B. T. Gard, K. Jacobs, R. McDermott, and M Saffman, "Microwave-to-optical frequency conversion using a cesium atom coupled to a superconducting resonator," *Physical Review A*, vol. 96, no. 1, p. 13 833, 2017. DOI: 10.1103/PhysRevA.96.013833.

[30] J. Han, T. Vogt, C. Gross, D. Jaksch, M. Kiffner, and W. Li, "Coherent Microwave-to-Optical Conversion via Six-Wave Mixing in Rydberg Atoms," *Physical Review Letters*, vol. 120, no. 9, p. 093 201, 2018. DOI: 10.1103/PhysRevLett.120.093201.

[31] T. Vogt, C. Gross, J. Han, S. B. Pal, M. Lam, M. Kiffner, and W. Li, "Efficient microwave-to-optical conversion using Rydberg atoms," *Physical Review A*, vol. 99, no. 2, p. 023 832, 2019. DOI: 10.1103/PhysRevA.99.023832.

[32] Z.-T. Liang, Q.-X. Lv, S.-C. Zhang, W.-T. Wu, Y.-X. Du, H. Yan, and S.-L. Zhu, "Coherent Coupling between Microwave and Optical Fields via Cold Atoms *," *Chinese Physics Letters*, vol. 36, no. 8, p. 080 301, 2019. DOI: 10.1088/0256-307X/36/8/080301.

[33] R. Zhang, S. R. Garner, and L. V. Hau, "Creation of Long-Term Coherent Optical Memory via Controlled Nonlinear Interactions in Bose-Einstein Condensates," *Physical Review Letters*, vol. 103, no. 23, p. 233 602, 2009. DOI: 10.1103/PhysRevLett.103.233602.

[34] O. Katz and O. Firstenberg, "Light storage for one second in room-temperature alkali vapor," *Nature Communications*, vol. 9, no. 1, p. 2074, 2018. DOI: 10.1038/s41467-018-04458-4.

[35] T. Bandi, M. Pellaton, D. Miletic, C. Affolderbach, F. Gruet, R. Matthey, G. Mileti, C. Stefanucci, M. Violetti, F. Merli, J.-F. Zurcher, and A. K. Skrivervik, "Double-resonance in alkali vapor cells for high performance and miniature atomic clocks," in *2012 IEEE International Frequency Control Symposium Proceedings*, IEEE, 2012, pp. 1–6. DOI: 10.1109/FCS.2012.6243654.

[36] Y Pétremand, C Affolderbach, R Straessle, M Pellaton, D Briand, G Mileti, and N. F. de Rooij, "Microfabricated rubidium vapour cell with a thick glass core for small-scale atomic clock applications," *Journal of Micromechanics and Microengineering*, vol. 22, no. 2, p. 025 013, 2012. DOI: 10.1088/0960-1317/22/2/025013.

[37] M Pellaton, C Affolderbach, Y Pétremand, N de Rooij, and G Mileti, "Study of laser-pumped double-resonance clock signals using a microfabricated cell," *Physica Scripta*, vol. T149, no. T149, p. 014 013, 2012. DOI: 10.1088/0031-8949/2012/T149/014013.

[38] T. Bandi, C. Affolderbach, C. Stefanucci, F. Merli, A. K. Skrivervik, and G. Mileti, "Compact high-performance continuous-wave double-resonance rubidium standard with 1.4×10^{-13} $\tau^{-1/2}$ stability," *IEEE Transactions on Ultrasonics, Ferroelectrics, and Frequency Control*, vol. 61, no. 11, pp. 1769–1778, 2014. DOI: 10.1109/TUFFC.2013.005955.

[39] W. Demtröder, "Optical Pumping and Double-Resonance Techniques," in *Laser Spectroscopy: Basic Concepts and Instrumentation*. Berlin, Heidelberg: Springer Berlin Heidelberg, 1996, pp. 552–593. DOI: 10.1007/978-3-662-08260-7_10.

[40] J. G. Coffer and J. C. Camparo, "Atomic stabilization of field intensity using Rabi resonances," *Physical Review A - Atomic, Molecular, and Optical Physics*, vol. 62, no. 1, p. 9, 2000. DOI: 10.1103/PhysRevA.62.013812.

[41] J. G. Coffer, B Sickmiller, A Presser, and J. C. Camparo, "Line shapes of atomic-candle-type Rabi resonances," *Physical Review A - Atomic, Molecular, and Optical Physics*, vol. 66, no. 2, p. 7, 2002. DOI: 10.1103/PhysRevA.66.023806.

[42] M. Kinoshita, K. Shimaoka, and K. Komiyama, "Determination of the Microwave Field Strength Using the Rabi Oscillation for a New Microwave Power Standard," *IEEE Transactions on Instrumentation and Measurement*, vol. 58, no. 4, pp. 1114–1119, 2009. DOI: 10.1109/TIM.2008.2010677.

[43] M. Kinoshita, K. Shimaoka, and Y. Shimada, "Optimization of the atomic candle signal for the precise measurement of microwave power," *IEEE Transactions on Instrumentation and Measurement*, vol. 62, no. 6, pp. 1807–1813, 2013. DOI: 10.1109/TIM.2013.2239071.

[44] F. Sun, J. Ma, Q. Bai, X. Huang, B. Gao, and D. Hou, "Measuring microwave cavity response using atomic Rabi resonances," *Applied Physics Letters*, vol. 111, no. 5, p. 051 103, 2017. DOI: 10.1063/1.4997302.

[45] M. Kinoshita and M. Ishii, "Electromagnetic field sensor based on atomic candle," in *IEEE Transactions on Instrumentation and Measurement*, vol. 66, 2017, pp. 1592–1597. DOI: 10.1109/TIM.2017.2661618.

[46] F. Y. Sun, D Hou, Q. S. Bai, and X. H. Huang, "Rabi resonance in Cs atoms and its application to microwave magnetic field measurement," *J. Phys. Commun. J. Phys. Commun*, vol. 2, no. 1, p. 015 008, 2018. DOI: 10.1088/2399-6528/aaa11f.

[47] F. Sun, Z. Jiang, J. Qu, Z. Song, J. Ma, and D. Hou, "Tunable Microwave Magnetic Field Detection based on Rabi Resonance with a Single Cesium-Rubidium Hybrid Vapor Cell," *Citation: Appl. Phys. Lett*, vol. 113, p. 164 101, 2018. DOI: 10.1063/1.5051025.

[48] H. Shi, J. Ma, X. Li, J. Liu, C. Li, and S. Zhang, "A Quantum-Based Microwave Magnetic Field Sensor," *Sensors*, vol. 18, no. 10, p. 3288, 2018. DOI: 10.3390/s18103288.

[49] X. Liu, Z. Jiang, J. Qu, D. Hou, X. Huang, and F. Sun, "Microwave magnetic field detection based on Cs vapor cell in free space," *Review of Scientific Instruments*, vol. 89, no. 6, p. 063 104, 2018. DOI: 10.1063/1.5029986.

[50] K. C. Cox, D. H. Meyer, F. K. Fatemi, and P. D. Kunz, "Quantum-Limited Atomic Receiver in the Electrically Small Regime," *PHYSICAL REVIEW LETTERS*, vol. 121, p. 110 502, 2018. DOI: 10.1103/PhysRevLett.121.110502.

[51] A. B. Deb and N. Kjærgaard, "Radio-over-fiber using an optical antenna based on Rydberg states of atoms," *Applied Physics Letters*, vol. 112, no. 21, p. 211 106, 2018. DOI: 10.1063/1.5031033.

[52] Y. Jiao, X. Han, J. Fan, G. Raithel, J. Zhao, and S. Jia, "Atom-based quantum receiver for amplitude- and frequency-modulated baseband signals in high-frequency radio communication," 2018.

[53] D. A. Anderson, R. E. Sapiro, and G. Raithel, "An atomic receiver for AM and FM radio communication," *IEEE Transactions on Antennas and Propagation*, pp. 1–1, 2020. DOI: 10.1109/TAP.2020.2987112.

[54] D. H. Meyer, K. C. Cox, F. K. Fatemi, and P. D. Kunz, "Digital communication with Rydberg atoms and amplitude-modulated microwave fields," *Applied Physics Letters*, vol. 112, no. 21, 2018. DOI: 10.1063/1.5028357.

[55] C. L. Holloway, M. T. Simons, A. H. Haddab, C. J. Williams, and M. W. Holloway, "A "real-time" guitar recording using Rydberg atoms and electromagnetically induced transparency: Quantum physics meets music," *AIP Advances*, vol. 9, no. 6, p. 065 110, 2019. DOI: 10.1063/1.5099036.

[56] Z. Song, H. Liu, X. Liu, W. Zhang, H. Zou, J. Zhang, and J. Qu, "Rydberg-atom-based digital communication using a continuously tunable radio-frequency carrier," *Optics Express*, vol. 27, no. 6, p. 8848, 2019. DOI: 10.1364/oe.27.008848.

[57] Y. Jiao, X. Han, J. Fan, G. Raithel, J. Zhao, and S. Jia, "Atom-based receiver for amplitude-modulated baseband signals in high-frequency radio communication," *Applied Physics Express*, vol. 12, no. 12, p. 126 002, 2019. DOI: 10.7567/1882-0786/ab5463.

[58] C. L. Holloway, M. T. Simons, J. A. Gordon, and D. Novotny, "Detecting and receiving phase-modulated signals with a rydberg atom-based receiver," *IEEE Antennas and Wireless Propagation Letters*, vol. 18, no. 9, pp. 1853–1857, 2019. DOI: 10.1109/LAWP.2019.2931450.

[59] J. A. Gordon, M. T. Simons, A. H. Haddab, and C. L. Holloway, "Weak electric-field detection with sub-1 Hz resolution at radio frequencies using a Rydberg atom-based mixer," *AIP Advances*, vol. 9, no. 4, 2019. DOI: 10.1063/1.5095633.

[60] M. T. Simons, A. H. Haddab, J. A. Gordon, and C. L. Holloway, "A Rydberg atom-based mixer: Measuring the phase of a radio frequency wave," *Applied Physics Letters*, vol. 114, no. 11, p. 114 101, 2019. DOI: 10.1063/1.5088821.

[61] C. L. Holloway, M. T. Simons, A. H. Haddab, C. J. Williams, and M. W. Holloway, "A "real-time" guitar recording using Rydberg atoms and electromagnetically induced transparency: Quantum physics meets music," *AIP Advances*, vol. 9, no. 6, 2019. DOI: 10.1063/1.5099036.

[62] A. Tretiakov, C. A. Potts, T. S. Lee, M. J. Thiessen, J. P. Davis, and L. J. LeBlanc, "Atomic microwave-to-optical signal transduction via magnetic-field coupling in a resonant microwave cavity," *Applied Physics Letters*, vol. 116, no. 16, p. 164 101, 2020. DOI: 10.1063/1.5144616.

[63] A. Tretiakov and L. J. LeBlanc, "Microwave Rabi resonances beyond the small-signal regime," *Physical Review A*, vol. 99, no. 4, p. 043 402, 2019. DOI: 10.1103/PhysRevA.99.043402.

[64] C. J. Foot, "Atomic physics," in. Oxford: Oxford University Press, 2005, ch. 4.

[65] D. J. Griffiths and D. F. Schroeter, "Introduction to quantum mechanics," in. Cambridge University Press, 2017, ch. 6.

[66] C Cohen-Tannoudji, B Diu, and F Laloë, "Quantum mechanics.," in. New York: Wiley-Interscience, 2006, ch. XII.

[67] D. A. Steck, *Rubidium 87 d line data*, http://steck.us/alkalidata/rubidium87numbers.pdf, 2001.

[68] C. J. Foot, "Atomic physics," in. Oxford: Oxford University Press, 2005, ch. 2.

[69] C. J. Foot, "Atomic physics," in. Oxford: Oxford University Press, 2005, ch. 6.

[70] M. Auzinsh, D. Budker, and S. Rochester, "Optically polarized atoms: Understanding light-atom interactions," in. Oxford University Press, 2010, ch. 7.

[71] I. I. Rabi, N. F. Ramsey, and J. Schwinger, "Use of rotating coordinates in magnetic resonance problems," *Reviews of Modern Physics*, vol. 26, no. 2, pp. 167–171, 1954. DOI: 10.1103/RevModPhys.26.167.

[72] D. A. Steck, "Quantum and Atom Optics," *Book*, 2007.

[73] R. P. Feynman, F. L. Vernon, and R. W. Hellwarth, "Geometrical Representation of the Schrödinger Equation for Solving Maser Problems," *Journal of Applied Physics*, vol. 28, no. 1, pp. 49–52, 1957. DOI: 10.1063/1.1722572.

[74] J. Johansson, P. Nation, and F. Nori, "QuTiP: An open-source Python framework for the dynamics of open quantum systems," *Computer Physics Communications*, vol. 183, no. 8, pp. 1760–1772, 2012. DOI: 10.1016/j.cpc.2012.02.021.

[75] J. Johansson, P. Nation, and F. Nori, "QuTiP 2: A Python framework for the dynamics of open quantum systems," *Computer Physics Communications*, vol. 184, no. 4, pp. 1234–1240, 2013. DOI: 10.1016/j.cpc.2012.11.019.

[76] D. Manzano, "A short introduction to the Lindblad master equation," *AIP Advances*, vol. 10, no. 2, p. 025 106, 2020. DOI: 10.1063/1.5115323.

[77] R. W. Boyd, "Nonlinear optics," in. Academic Press, 2008, ch. 6, p. 613.

[78] A. Papoyan and S. Shmavonyan, "Signature of optical Rabi oscillations in transmission signal of atomic vapor under continuous-wave laser excitation," *Optics Communications*, vol. 482, p. 126 561, 2021. DOI: 10.1016/j.optcom.2020.126561.

[79] M. Reagor, H. Paik, G. Catelani, L. Sun, C. Axline, E. Holland, I. M. Pop, N. A. Masluk, T. Brecht, L. Frunzio, M. H. Devoret, L. Glazman, and R. J. Schoelkopf, "Reaching 10 ms single photon lifetimes for superconducting aluminum cavities," *Applied Physics Letters*, vol. 102, no. 19, p. 192 604, 2013. DOI: 10.1063/1.4807015.

[80] A. Tretiakov, *Versatile apparatus for ultracold atomic hybrid systems*, 2016. DOI: 10.7939/R30V89V89.

[81] T. Hrushevskyi, *Quantum gas apparatus for Bose-Einstein condensation of 87 Rb*, 2017. DOI: 10.7939/R3H708C43.

[82] A. Rastogi, *Light-matter interactions for quantum simulation and quantum memory experiments*, 2018. DOI: 10.7939/R3JS9HQ4Q.

[83] M. A. Sullivan, *A Cold Atoms Apparatus for a New Hybrid Quantum System*, 2020. DOI: 10.7939/R3-6VVJ-KC16.

[84] J. Vanier and C. Tomescu, *The quantum physics of atomic frequency standards: recent developments*. CRC Press, 2015.

[85] A. Horsley, "High Resolution Field Imaging with Atomic Vapor Cells," Ph.D. dissertation, 2015. DOI: 10.5451/unibas-006504997.

[86] G. Moon and H.-R. Noh, "Analytic calculation of linear susceptibility in velocity-dependent pump-probe spectroscopy," *Physical Review A*, vol. 78, no. 3, p. 032 506, 2008. DOI: 10.1103/PhysRevA.78.032506.

[87] D Main, T. M. Hird, S Gao, I. A. Walmsley, and P. M. Ledingham, "Room Temperature Atomic Frequency Comb Memory for Light," 2020.

[88] D Main, T. M. Hird, S Gao, E Oguz, D. J. Saunders, I. A. Walmsley, and P. M. Ledingham, "Preparing Narrow Velocity Distributions for Quantum Memories in Room-Temperature Alkali Vapours," 2020. arXiv: 2011.03766.

[89] T. Bandi, "Double-resonance studies on compact, high-performance rubidium cell frequency standards," *PhD Thesis, Neuchatel*, no. April, 2013.

[90] E. Saglamyurek, T. Hrushevskyi, A. Rastogi, K. Heshami, and L. J. LeBlanc, "Coherent storage and manipulation of broadband photons via dynamically controlled autler–townes splitting," *Nature Photonics*, vol. 12, no. 12, p. 774, 2018.

[91] I. D. Leroux and J. H. Thywissen, "Manipulation of Ultra-Cold Atoms Using Radio-Frequency and Microwave Radiation," Tech. Rep., 2005.

[92] V. I. Yudin, A. V. Taichenachev, and M. Y. Basalaev, "Dynamic steady state of periodically driven quantum systems," *Physical Review A*, vol. 93, no. 1, p. 013 820, 2016. DOI: 10.1103/PhysRevA.93.013820.

[93] U. Cappeller and H. Müller, "Phasenmodulierte Anregung eines optisch gepumpten Spinsystems," *Annalen der Physik*, vol. 497, no. 3, pp. 250–264, 1985. DOI: 10.1002/andp.19854970306.

[94] J. C. Camparo and R. P. Frueholz, "Observation of the Rabi-resonance spectrum," *Physical Review A*, vol. 38, no. 12, pp. 6143–6150, 1988. DOI: 10.1103/PhysRevA.38.6143.

[95] F. Sun, J. Ma, Q. Bai, X. Huang, B. Gao, and D. Hou, "Measuring microwave cavity response using atomic Rabi resonances," *Appl. Phys. Lett.*, vol. 111, no. 5, p. 051 103, 2017. DOI: 10.1063/1.4997302.

[96] M. Kinoshita, K. Shimaoka, and K. Komiyama, "Atomic Microwave Power Standard Based on the Rabi Frequency," *IEEE Trans. Instrum. Meas.*, vol. 60, no. 7, pp. 2696–2701, 2011. DOI: 10.1109/TIM.2010.2091299.

[97] T. Swan-Wood, J. Coffer, and J. Camparo, "Precision measurements of absorption and refractive-index using an atomic candle," *IEEE Trans. Instrum. Meas.*, vol. 50, no. 5, pp. 1229–1233, 2001. DOI: 10.1109/19.963189.

[98] P. T. Dat, A. Kanno, and T. Kawanishi, "Radio-on-radio-over-fiber: efficient fronthauling for small cells and moving cells," *IEEE Wireless Communications*, vol. 22, no. 5, pp. 67–75, 2015. DOI: 10.1109/MWC.2015.7306539.

[99] J. Guillory, "networks Radio over Fiber for the future Home Area Networks," Ph.D. dissertation, 2013.

[100] J. Bohata, M. Komanec, J. Spáčil, Z. Ghassemlooy, S. Zvánovec, and R. Slavík, "24–26 GHz radio-over-fiber and free-space optics for fifth-generation systems," *Optics Letters*, vol. 43, no. 5, p. 1035, 2018. DOI: 10.1364/OL.43.001035.

[101] C. L. Holloway, M. Simons, J. Gordon, and D. Novotny, "Detecting and Receiving Phase Modulated Signals with a Rydberg Atom-Based Receiver," *IEEE Antennas and Wireless Propagation Letters*, vol. 18, no. 9, pp. 1–1, 2019. DOI: 10.1109/lawp.2019.2931450.

[102] H. Zou, Z. Song, H. Mu, Z. Feng, J. Qu, and Q. Wang, "Atomic receiver by utilizing multiple radio-frequency coupling at rydberg states of rubidium," *Applied Sciences*, vol. 10, no. 4, p. 1346, 2020.

[103] C. L. Holloway, M. T. Simons, A. H. Haddab, J. A. Gordon, and S. D. Voran, "A multiple-band rydberg-atom based receiver/antenna: Am/fm stereo reception," *arXiv preprint arXiv:1903.00786*, 2019.

[104] G. C. Bjorklund, "Frequency-modulation spectroscopy: a new method for measuring weak absorptions and dispersions," *Optics Letters*, vol. 5, no. 1, p. 15, 1980. DOI: 10.1364/OL.5.000015.

[105] M. Rudd, P. Kim, C. Potts, C Doolin, H Ramp, B. Hauer, and J. Davis, "Coherent Magneto-optomechanical Signal Transduction and Long-Distance Phase-Shift Keying," *Physical Review Applied*, vol. 12, no. 3, p. 034 042, 2019. DOI: 10.1103/PhysRevApplied.12.034042.

[106] Q. Sun, Y. Hong, W. Zhuang, Z. Liu, and J. Chen, "Demonstration of an excited-state Faraday anomalous dispersion optical filter at 1529 nm by use of an electrodeless discharge rubidium vapor lamp," *Applied Physics Letters*, vol. 101, no. 21, p. 211 102, 2012. DOI: 10.1063/1.4767140.

[107] P. Chang, H. Peng, S. Zhang, Z. Chen, B. Luo, J. Chen, and H. Guo, "A Faraday laser lasing on Rb 1529 nm transition," *Scientific Reports*, vol. 7, no. 1, p. 8995, 2017. DOI: 10.1038/s41598-017-09501-w.

[108] L. D. Turner, V. Karaganov, P. J. O. Teubner, and R. E. Scholten, "Sub-Doppler bandwidth atomic optical filter," *Optics Letters*, vol. 27, no. 7, p. 500, 2002. DOI: 10.1364/OL.27.000500.

[109] E. Saglamyurek, T. Hrushevskyi, A. Rastogi, K. Heshami, and L. J. LeBlanc, "Coherent storage and manipulation of broadband photons via dynamically controlled Autler–Townes splitting," *Nature Photonics*, vol. 12, no. 12, pp. 774–782, 2018. DOI: 10.1038/s41566-018-0279-0.

[110] C. Prosko, *Evaporative Cooling of 87 Rb with Microwave Radiation*, 2015. [Online]. Available: https://sites.ualberta.ca/~ljleblan/proskophys499_2015.pdf.

[111] J. C. Camparo, J. G. Coffer, and R. P. Frueholz, "Rabi resonances induced by an off-resonant, stochastic field," *Phys. Rev. A*, vol. 58, no. 5, pp. 3873–3878, 1998. DOI: 10.1103/PhysRevA.58.3873.

[112] M. Ishii and M. Kinoshita, "A feasibility study of a real-time visualization method for electromagnetic fields," *Microwave and Optical Technology Letters*, vol. 63, no. 2, pp. 399–403, 2021. DOI: 10.1002/mop.32608.

[113] A. V. Alekseev and N. V. Sushilov, "Analytic solutions of Bloch and Maxwell-Bloch equations in the case of arbitrary field amplitude and phase modulation," *Phys. Rev. A*, vol. 46, no. 1, pp. 351–355, 1992. DOI: 10.1103/PhysRevA.46.351.

[114] J Dalibard and C Cohen-Tannoudji, "Laser cooling below the Doppler limit by polarization gradients: simple theoretical models," *Journal of the Optical Society of America B*, vol. 6, no. 11, p. 2023, 1989. DOI: 10.1364/JOSAB.6.002023.

[115] H Schmidt and R. J. Ram, "All-optical wavelength converter and switch based on electromagnetically induced transparency," *Applied Physics Letters*, vol. 76, no. 22, pp. 3173–3175, 2000. DOI: 10.1063/1.126620.

[116] S. E. Harris and Y Yamamoto, "Photon Switching by Quantum Interference," *Physical Review Letters*, vol. 81, no. 17, pp. 3611–3614, 1998. DOI: 10.1103/PhysRevLett.81.3611.

[117] S. Baur, D. Tiarks, G. Rempe, and S. Dürr, *Physical Review Letters*, vol. 112, no. 7, p. 073 901, 2014. DOI: 10.1103/PhysRevLett.112.073901.

[118] H. Gorniaczyk, C. Tresp, J. Schmidt, H. Fedder, and S. Hofferberth, "Single-Photon Transistor Mediated by Interstate Rydberg Interactions," *Physical Review Letters*, vol. 113, no. 5, p. 053 601, 2014. DOI: 10.1103/PhysRevLett.113.053601.

[119] D. Tiarks, S. Baur, K. Schneider, S. Dürr, and G. Rempe, "Single-Photon Transistor Using a Förster Resonance," *Physical Review Letters*, vol. 113, no. 5, p. 053 602, 2014. DOI: 10.1103/PhysRevLett.113.053602.

[120] W. Chen, K. M. Beck, R. Bücker, M. Gullans, M. D. Lukin, H. Tanji-Suzuki, and V. Vuletić, "All-optical switch and transistor gated by one stored photon," *Science*, vol. 341, no. 6147, pp. 768–770, 2013. DOI: 10.1126/science.1238169.

[121] M. Ghosh, A. Karigowda, A. Jayaraman, F. Bretenaker, B. C. Sanders, and A. Narayanan, "Demonstration of a high-contrast optical switching in an atomic Delta system," *Journal of Physics B: Atomic, Molecular and Optical Physics*, vol. 50, no. 16, p. 165 502, 2017. DOI: 10.1088/1361-6455/aa8014.

[122] S. Pustelny, A. Wojciechowski, M. Gring, M. Kotyrba, J. Zachorowski, and W. Gawlik, "Magnetometry based on nonlinear magneto-optical rotation with amplitude-modulated light," *Journal of Applied Physics*, vol. 103, no. 6, p. 063 108, 2008. DOI: 10.1063/1.2844494.

[123] B Patton, E Zhivun, D. C. Hovde, and D Budker, "All-Optical Vector Atomic Magnetometer," vol. 113, no. 1, p. 013 001, 2014. DOI: 10.1103/PhysRevLett.113.013001.

[124] K. Jensen, R. Budvytyte, R. A. Thomas, T. Wang, A. M. Fuchs, M. V. Balabas, G. Vasilakis, L. D. Mosgaard, H. C. Stærkind, J. H. Muller, T. Heimburg, S. P. Olesen, and E. S. Polzik, "Non-invasive detection of animal nerve impulses with an atomic magnetometer operating near quantum limited sensitivity," *Scientific Reports*, vol. 6, no. 1, pp. 1–7, 2016. DOI: 10.1038/srep29638.

[125] K. Jensen, M. A. Skarsfeldt, H. Stærkind, J. Arnbak, M. V. Balabas, S.-P. Olesen, B. H. Bentzen, and E. S. Polzik, "Magnetocardiography on an isolated animal heart with a room-temperature optically pumped magnetometer," *Scientific Reports*, vol. 8, no. 1, p. 16 218, 2018. DOI: 10.1038/s41598-018-34535-z.

[126] N. Wilson, P. Light, A. Luiten, and C. Perrella, "Ultrastable Optical Magnetometry," *Physical Review Applied*, vol. 11, no. 4, p. 044 034, 2019. DOI: 10.1103/PhysRevApplied.11.044034.

[127] M. Limes, E. Foley, T. Kornack, S Caliga, S. McBride, A Braun, W Lee, V. Lucivero, and M. Romalis, "Portable Magnetometry for Detection of Biomagnetism in Ambient Environments," *Physical Review Applied*, vol. 14, no. 1, p. 011 002, 2020. DOI: 10.1103/PhysRevApplied.14.011002.

[128] N. Wilson, C. Perrella, R. Anderson, A. Luiten, and P. Light, "Wide-bandwidth atomic magnetometry via instantaneous-phase retrieval," 2020. DOI: 10.1103/PhysRevResearch.2.013213.

[129] M. Takeuchi, T. Takano, S. Ichihara, Y. Takasu, M. Kumakura, T. Yabuzaki, and Y. Takahashi, "Paramagnetic Faraday rotation with spin-polarized ytterbium atoms," *Applied Physics B*, vol. 83, no. 1, pp. 107–114, 2006. DOI: 10.1007/s00340-006-2136-y.

[130] P. Siddons, C. S. Adams, and I. G. Hughes, "Optical control of Faraday rotation in hot Rb vapor," *Physical Review A*, vol. 81, no. 4, p. 043 838, 2010. DOI: 10.1103/PhysRevA.81.043838.

[131] C. Kupchak, P. J. Bustard, K. Heshami, J. Erskine, M. Spanner, D. G. England, and B. J. Sussman, "Time-bin-to-polarization conversion of ultrafast photonic qubits," *Physical Review A*, vol. 96, no. 5, p. 053 812, 2017. DOI: 10.1103/PhysRevA.96.053812.

[132] K. L. Fenwick, D. G. England, P. J. Bustard, J. M. Fraser, and B. J. Sussman, "Carving out configurable ultrafast pulses from a continuous wave source via the optical Kerr effect," *Optics Express*, vol. 28, no. 17, p. 24 845, 2020. DOI: 10.1364/OE.399878.

[133] A. Hudson and J. Camparo, "Quantum System Dynamics and the Quasistatic Approximation," *Physical Review Applied*, vol. 13, no. 6, p. 064 007, 2020. DOI: 10.1103/PhysRevApplied.13.064007.

Appendix A: Angular momentum operators

In this appendix we present some definitions and conventions concerning the angular momentum operators that we use throughout the thesis. As an example we will consider the total atomic angular momentum operator $\hat{\mathbf{F}}$. Each component of $\hat{\mathbf{F}}$ corresponds to the projection of the angular momentum on the corresponding axis. In general, atomic quantum states are described in terms of Hermitian operators $\hat{F}_z$ and $\hat{\mathbf{F}^2} = F^2 = F_x^2 + F_y^2 + F_z^2$, corresponding to the projection of the angular momentum vector on the z-axis and the square of the vector's magnitude, respectively. Operators $\hat{F}_z$ and $\hat{F}^2$ commute with each other and have common eigenstates $|F, m_F\rangle$, such that

$$\hat{F}_z |F, m_F\rangle = \hbar m_F |F, m_F\rangle , \tag{A.1}$$

and

$$\hat{F}^2 |F, m_F\rangle = \hbar^2 F(F+1) |F, m_F\rangle , \tag{A.2}$$

where $m_F = -F, -F+1, \ldots, F-1, F$, both m_F and F are dimensionless, and F is positive.

When the atomic energy does not depend on m_F, we typically describe the atomic state in terms of level $|F\rangle$, which refers to a set of all quantum states that differ only in m_F.

Appendix B: Polarization in atomic transitions

In this Appendix we provide more details on the polarization of oscillating fields involved in the atomic transitions. The polarization type is indicated with respect to a particular quantization axis, which is typically along the z-axis.

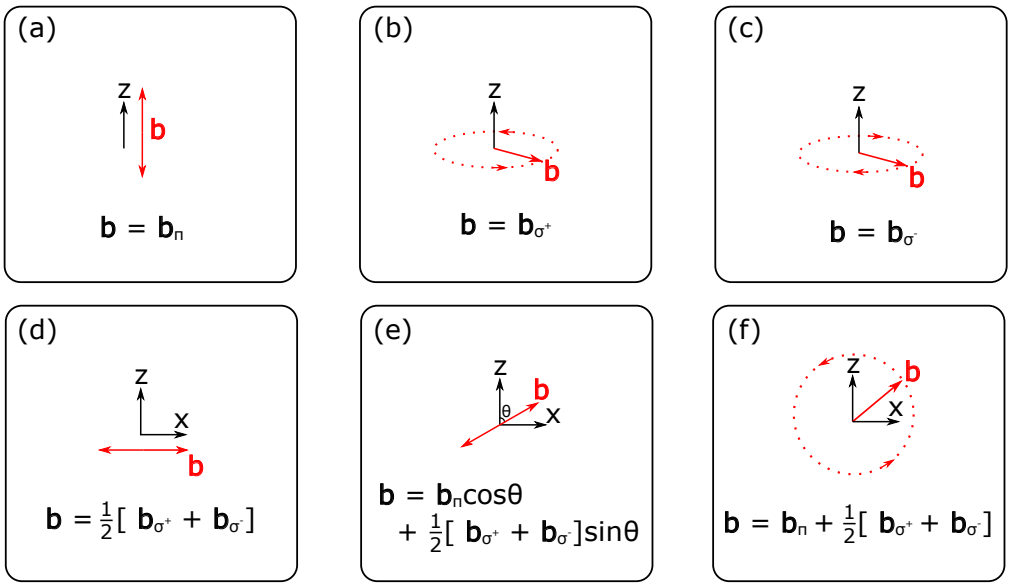

Figure B.1: Several examples of polarization of field $\mathbf{b}$ with respect to the z-axis.

A linearly-polarized field is π-polarized with respect to the z-axis, if its vector is parallel to the z-axis [see Figure B.1(a)]:

$$\mathbf{b}_\pi(t) = \mathbf{z} b_0 \cos(\omega t + \phi). \tag{B.1}$$

A circularly-polarized field is σ-polarized with respect to the z-axis, if its vector

rotates around the z-axis in the perpendicular plane [see Figure B.1(b,c)]:

$$\mathbf{b}_{\sigma^{\pm}}(t) = \mathbf{x} b_0 \cos(\omega t + \phi) \pm \mathbf{y} b_0 \sin(\omega t + \phi). \tag{B.2}$$

In general, any polarization is a linear combination of π and $\sigma^{\pm}$ polarization components. For example, a linearly-polarized field whose vector is perpendicular to z-axis [see Figure B.1(d)] is an equal superposition of two fields that are σ^{+}- and σ^{-}-polarized with respect to the z-axis:

$$\mathbf{b}(t) = \mathbf{x} b_0 \cos(\omega t + \phi) = \frac{1}{2}\left[\mathbf{x} b_0 \cos(\omega t + \phi) + \mathbf{y} b_0 \sin(\omega t + \phi)\right] \tag{B.3}$$

$$+\frac{1}{2}\left[\mathbf{x} b_0 \cos(\omega t + \phi) - \mathbf{y} b_0 \sin(\omega t + \phi)\right] = \frac{1}{2}\mathbf{b}_{\sigma^{+}}(t) + \frac{1}{2}\mathbf{b}_{\sigma^{-}}(t). \tag{B.4}$$

If the vector of a linearly-polarized field makes an arbitrary angle θ with respect to the z-axis [see Figure B.1(e)], the z-component corresponds to the π-polarization and the x component with respect to the z-axis is an equal superposition of σ^{+} and σ^{-} polarization components. The total polarization with respect to the z is

$$\mathbf{b}(t) = \mathbf{b}_{\pi}(t)\cos\theta + \frac{1}{2}\left[\mathbf{b}_{\sigma^{+}}(t) + \mathbf{b}_{\sigma^{-}}(t)\right]\sin\theta. \tag{B.5}$$

Finally, if the field is circularly-polarized in the plane parallel to the z-axis [see Figure B.1(f)], the polarization with respect to the z-axis is

$$\mathbf{b}(t) = \mathbf{x} b_0 \cos(\omega t + \phi) \pm \mathbf{z} b_0 \sin(\omega t + \phi) = \frac{1}{2}\left[\mathbf{b}_{\sigma^{+}}(t) + \mathbf{b}_{\sigma^{-}}(t)\right] \pm \mathbf{b}_{\pi}(t). \tag{B.6}$$

Appendix C: Modulated signals

In this appendix we provide illustrative examples of the amplitude, frequency, and phase modulation.

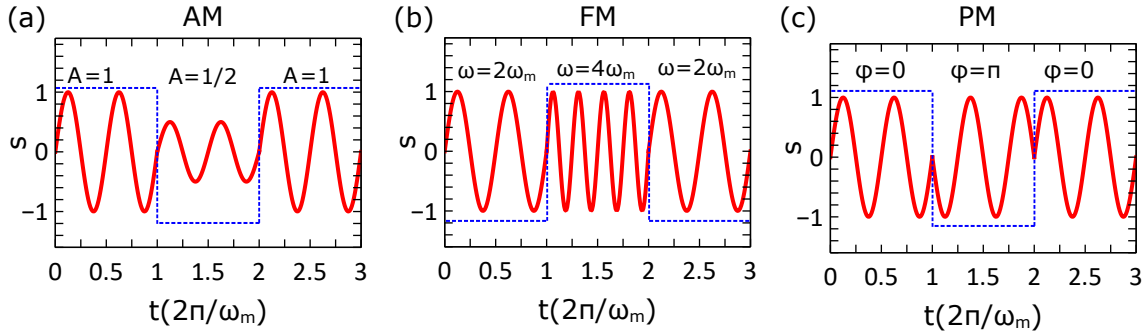

Figure C.1: Examples of different types of modulation. (a) Square-wave amplitude modulation between $A = 1$ and $A = 0.5$ at the modulation frequency is $\omega_{\rm m}$. The carrier frequency is $\omega_0 = \omega_{\rm m}$. (b) Square-wave frequency modulation between $\omega = 2\omega_{\rm m}$ and $\omega = 4\omega_{\rm m}$. (c) Square-wave phase modulation between $\phi = 0$ and $\phi = \pi$. Red solid curves correspond to the signal $s(t)$, blue dashed curves correspond to the modulating signal.

The amplitude-modulated (AM) signal is given by

$$s(t) = A(t)\sin[\omega_0 t + \phi_0], \tag{C.1}$$

where the frequency ω_0 and the quadrature phase ϕ_0 are constant, and the amplitude $A(t)$ is a function of time given by

$$A(t) = A_0\left[1 + m_{\rm AM}V(t)\right], \tag{C.2}$$

where A_0 is the unmodulated amplitude, $m_{\rm AM}$ is the amplitude-modulation index,

and $V(t)$ is the modulating signal. Figure C.1(a) shows the signal whose amplitude is modulated between A_0 and $A_0/2$ with periodic square-wave pulses.

The frequency-modulated (FM) signal is given by

$$s(t) = A_0 \sin[\omega(t)t + \phi_0], \tag{C.3}$$

where

$$\omega(t) = \omega_0 + m_{\mathrm{FM}} V(t), \tag{C.4}$$

m_{FM} is the frequency-modulation index. Figure C.1(b) shows the signal whose frequency is modulated between ω_0 and $2\omega_0$ with periodic square-wave pulses.

The phase-modulated (PM) signal is given by

$$s(t) = A_0 \sin[\omega_0 t + \phi(t)], \tag{C.5}$$

where

$$\phi(t) = \phi_0 + m_{\mathrm{PM}} V(t), \tag{C.6}$$

where m_{PM} is the phase-modulation index. Figure C.1(c) shows the signal whose frequency is modulated between 0 and π with periodic square-wave pulses.